A STUDY OF PRECIPITATED FILMS FORMED DURING ELECTROCHEMICALLY DRIVEN DISSOLUTION PROCESSES

by

Joshua Aaron Hammons

A thesis submitted to the University of Birmingham for the degree of DOCTOR OF PHILOSOPHY

School of Chemistry
University of Birmingham
August 2011

Abstract

Precipitated surface films form when metal cations are produced faster than they can move away from the dissolving interface. This build up of cations results in supersaturation conditions, which cause a solid to precipitate. The precipitated solid affects ion transport and thus the dissolution kinetics, which ultimately control the two systems studied here. X-ray diffraction, small angle X-ray scattering and fast radiography were chosen to study the metal/solution interface *in-situ*, using synchrotron radiation.

The AC electrograining system is a widely used industrial process whereby an alternating current is applied to aluminium plates to form a pitted surface. During this process, an $Al(OH)_3$ surface gel (smut) forms within seconds whilst electrograining continues for several minutes in its presence. Although smut formation has been investigated previously, how the smut affects metal dissolution is currently unknown and is the primary goal of this project.

The second system is a nickel "artificial pit," which is commonly used to simulate pit propagation. In this system, a salt film is precipitated by imposing a large overpotential whilst restricting transport through a 1-D pit. Interfacial phenomena that occur during salt film formation are investigated towards an understanding of how the salt film forms.

Acknowledgements

I would like to acknowledge my advisor Trevor Rayment for his help and support throughout my PhD and, along with the School of Chemistry, for providing me the opportunity to study at the University of Birmingham. I would also like to thank my co-advisor, Alison Davenport, for her help and support, particularly with allowing me access to her offices and laboratory. I would especially like to thank Mehdi Monir and Majid Ghahari for the extensive experimental support and discussions throughout my PhD.

The AC electrograining project was done in collaboration with the Vrije Universiteit Brussel (VUB), Research Group Electrochemical and Surface Engineering (SURF), Department Materials and Chemistry. I am very thankful for the support of their facilities as well as the discussions I was able to have with the people in their department. All SEM images, presented in this thesis, were obtained by Marc Raes and Maria Tzedaki and were invaluable to my PhD.

I greatly acknowledge all of help, support and experimental expertise from the beamline scientists and staff at: Station 6.2 Daresbury (Dr. Christopher Martin), I22 at Diamond (Dr. Nick Terrill), TOMCAT beamline at the Swiss Light Source (Dr. Marco Stampanoni), DUBBLE beamline at the European Synchrotron Light Source (Dr. Wim Bras) and 32ID at the Advanced Photon Source (Dr. Jan Ilavsky).

I would also like to thank the School of Chemistry and the School of Metallurgy and Materials for the use of their facilities and funding from the Engineering and Physical Sciences Research Council.

Finally, I would also like to recognize that this would have not been possible without the support of my friends and family.

Table of Contents

List of Illustrations

List of Symbols

X-Ray Symbols

I	X-ray intensity
I_o	Incoming intensity
I_t	Transmitted X-ray intensity
I_{o_B}	Incoming intensity during an electrograining burst
I_{t_B}	Transmitted intensity during an electrograining burst
I_e	Scattered intensity
2θ	Scattering angle
$2\theta_0$	Angle of peak centre
$\ddot{A}$	X-ray amplitude
$\Delta\Omega$	Solid angle of the X-ray beam
A_c	Cross-sectional area
V	Total volume
V_p	Particle volume
P_s	Perimeter
r_e	Classical electron radius
ς	Phase
$\boldsymbol{s}$	X-ray unit vector
$\boldsymbol{q}$, q	X-ray scattering vector and magnitude, Respectively
$\boldsymbol{r}$, r	Vector and magnitude between scattering centres, respectively.
$\mathbf{r_j}$	Vector between atoms in a unit cell.
$\mathbf{R_n}$	Vector between unit cells.
λ	X-ray wavelength
f	Scattering factor
d	Lattice spacing
k	Generic constant
ρ_e	Scattering length density (formally). Commonly, referred to as simply the Electron density
$\Delta\rho_e$	Electron density contrast between 2 Phases
$\overline{\rho_e}^2(\boldsymbol{r})$	Patterson function (auto-correlation of the electron density)
γ	Normalized Patterson function (also called the correlation function)
$\langle\rho_e\rangle$	Volume average electron density
v	Volume fraction
N	Number of scatterers

n_e	Number of electrons
G	Guinier pre-factor
B	Porod pre-factor
B_{kdg}	Background intensity
R_g	Radius of gyration
RCO	Cut-off radius (Unified Equation)
P	Exponent for intensity power law decay
k	General constant
n	Any integer
D_n	Number distribution
$F(q,R)$	Form factor
ρ_m	Mass density
d_s	Surface fractal dimension
d_m	Mass fractal dimension
h	Geometrical contribution to an agglomerate correlation function
Q	Total scattering (also called the Invariant)
Q_φ	Anisotropic total scattering (also called the pseudo-invariant)
Fl, Fl_1	Electron density fluctuations: Isotropic and 1-D anisotropic, respectively
σ	Transition layer thickness (standard deviation)
V_c	Total crystalline volume
Δ	Full Width at Half Maximum (FWHM) also the Transition layer thickness (FWHM)
Δ_{raw}	FWHM of an XRD peak obtained from the raw data
Δ_s	FWHM of an XRD peak obtained from the NBS Si standard
Δ_k	Estimated FWHM of an XRD peak obtained from the silicon standard
Δ_0	Instrumental FWHM
Vc	Total crystalline volume
l	Crystal size
x_t	Thickness
T_r	X-ray transmission
A	Excess absorption (relative to saturation)
μ/ρ	Mass absorption coefficient
m	Mass
x_m	Mass fraction
$SAS2D$	Raw SAXS image obtained from the detector
T_s	X-ray transmission relative to the that obtained during the previous burst

z_{deg}	Degree of agglomeration
c	Linearity
d_{min}	Minimum dimension
$\overline{\eta^2}$	Average square fluctuations in electron density (contrast)
ω	Angle in plane with X-rays
φ	Azmuthal angle perpendicular to X-rays
X,Y,Z	Surface layer dimensions
α,β,δ	Cosines of the angles between the Vector, **q**, and each of the three axes in real space.
i_L	Limiting current density at 0 V
J	Flux
x_B	Salt film boundary
A_{max}	Maximum excess absorption
A_0	Baseline absorption
$T_{r_o}(x)$	Averaged transmission profile obtained During the 0 V period
$T_{r_i}(x)$	Averaged transmission profile obtained From each subsequent frame
$\overline{\eta_f^2}$	Fractional contrast

Electrochemistry Symbols

μ	Chemical potential
$\tilde{\mu}$	Electrochemical potential
F	Faraday's constant
z	Ion charge
n	Number of reaction electrons
Φ	Electrostatic potential
Φ_0	Open circuit potential
Φ_0^0	Standard potential
Φ_a	Peak anodic potential
Φ_c	Peak cathodic potential
$R_{RE/WE}$	Resistance between the reference and working electrodes
ε	permittivity
i	Current density
i_o	Exchange current density
α_a	Anodic kinetic parameter (Tafel slope)
α_c	Cathodic kinetic parameter (Tafel slope)
C	Concentration
Γ	Activity coefficient
R	Gas constant
s	Stoichometric coefficient
ξ	Reaction order
κ	Conductivity
O_{ij}	Onsager coefficient
$\mathbf{v}$	Velocity
u	Mobility
Λ	Equivalent conductance
D	Diffusion coefficient
D_{eff}	Effective diffusion coefficient
ϕ	Porosity
τ	Tortuosity
L	Smut thickness
L_e	Actual pore length
x	Independent space variable
t	Time
p	Pressure or partial pressure
Δp	Pressure gradient
K_1, K_2, K_3	Fit constants
t_{lag}	Lag time

List of Abbreviations

AC	Alternating Current
DC	Direct Current
SAXS	Small Angle X-ray Scattering
WAXS	Wide Angle X-ray Scattering
XRD	X-ray Diffraction
SRS	Synchrotron Radiation Source
DLS	Diamond Light Source
SLS	Swiss Light Source
ESRF	European Synchrotron Source
APS	Advanced Photon Source
WE	Working electrode
RE	Reference electrode
CE	Counter electrode
DHO	Debye-Huckel-Onsager

CHAPTER 1
Introduction

Studies of interfacial phenomena in two different electrochemical dissolution systems are presented in this thesis. Metal dissolution is a very common and much-studied phenomenon in electrochemistry, but becomes complicated when ion transport away from the metal becomes restricted. In the simplest case, the dissolved metal cations immediately diffuse and/or migrate away from the interface as more metal is dissolved. However, when the metal ion transport is restricted, the concentration of these metal cations increases near the interface, which attracts anions towards themselves to maintain charge balance. If the cation/anion concentration reaches supersaturation levels, a solid is precipitated, which can further restrict transport away from the metal.

The focus of this research is the effect of the precipitated solid on continued metal dissolution. In the first system presented, an alternating current is imposed on an aluminium substrate to form a uniformly pitted surface. This process is commonly known as AC electrograining and has application in lithographic printing as well as energy storage super-capacitors. During this process the solid that is precipitated is an $Al(OH)_3$ gel (smut), whose presence is expected to change the conditions at the reaction plane and ultimately affect metal dissolution kinetics. The mechanism of smut film formation is well understood and is not investigated here. Instead, the overall goal of this study is to understand the role that the gel plays on the final surface morphology, in particular how it affects metal dissolution during AC electrograining.

The second system is a nickel artificial pit system that is used to simulate pit propagation. In this system, a thin nickel foil is dissolved inside a one dimensional pit, where ion transport is intentionally restricted as is the case in a real pit. A precipitated salt film that forms during the metal dissolution restricts transport away from the interface, which is believed to maintain an aggressive solution at the reaction plane; this allows for continued dissolution in a real pit. Although many electrochemical studies have been performed on these salt films at steady state, there is only limited knowledge of how the salt film forms; researchers generally accept that the metal is dissolved until supersaturation conditions exist near the interface, at which time the salt precipitates. The approach used here is to apply a potential step to form the salt film. During the salt film formation, interfacial phenomena are studied, as a function of time, with the hope of understanding the composition of the salt film and how it is formed.

To probe interfacial phenomena, X-ray scattering and fast radiography were used. Synchrotron radiation was used to provide the required flux to study the two systems *in-situ*. The use of synchrotron radiation allows for a high flux of X-rays to pass through a solution and interact with all possible scattering populations near the interface to give a relatively high signal compared to a traditional X-ray tube. For small angle scattering, possible scattering populations include any phase with an appreciable difference in electron density, compared to the adjacent phase. The size of this phase must be on the nanometre scale to be observed with X-rays. X-ray diffraction is also used and can provide the phase identification of any crystalline material near the interface, as well as the total crystalline volume and size. Finally, fast radiography is a useful technique to measure the absorption profile across the interface, which will be a function of the solution composition by the Beer-Lambert law.

The scope of this work is centred on X-ray scattering and electrochemistry. In the following chapter, the required theory and background of these two disciplines are reviewed, as they are

applicable to this thesis. The experimental methods used for both systems are presented together in Chapter 3. Chapters 4 and 5 contain a literature review and a presentation of work performed on the AC electrograining system, respectively. Chapters 6 and 7 contain the literature review and a presentation of work performed on the nickel artificial pit system, respectively. Finally, the significant conclusions and future work are discussed in Chapter 8.

CHAPTER 2
Theory and Background

In this chapter the theories behind the techniques that are used in this thesis are presented. Synchrotron radiation and X-ray techniques are presented first, followed by the fundamentals of electrochemistry and electrochemical methods. A brief description of synchrotron radiation is presented, followed by fundamentals of general X-ray scattering, small angle X-ray scattering (SAXS), X-ray diffraction (XRD) and then radiography. A complete and comprehensive discussion of synchrotron radiation, supporting equipment, detectors and X-ray scattering is not provided, as only concepts relevant to the experiments presented in this thesis are discussed.

In general, SAXS and XRD are based on the constructive interference of the coherently scattered X-rays; the degree to which these scattered X-rays constructively interfere depends on the sample and angle of measurement. Radiography is based on the Beer-Lambert law, where the transmitted intensity is a function of sample thickness and composition. Most of the information presented in these sections is taken from text books written by: Guinier[1, 2], Glatter[3] and Als-Nielsen[4]. All three techniques were applied using synchrotron radiation at five different synchrotrons: Synchrotron Radiation Source (SRS) Daresbury Laboratory, Diamond Light Source (DLS), European Synchrotron Radiation Facility (ESRF), the Swiss Light Source (SLS) and the Advanced Photon Source (APS).

Chapter 2 Theory

Both of the systems studied in this thesis are electrochemical systems. Electrochemical concepts, such as: dissolution kinetics and ionic transport are important in the analysis of these systems and are also discussed in this chapter.

2.a X-ray Scattering Using Synchrotron Radiation

X-rays are electromagnetic waves and typically have wavelengths between 0.02 Å and 12 Å. Such small wavelengths make characterization of structural inhomogenieties on the nanometre scale possible. In any scattering experiment the determination of the structure of these small features relies on the degree of interference between X-rays, which are scattered by electrons in the sample. This fundamental principle results in changes in the amplitude, $\ddot{A}$, as the wave crests are added (constructive interference) or subtracted (destructive interference) from one another. In reality, the intensity is what is measured and related to the amplitude by the equation:

(2.1) $I = \ddot{A}\ddot{A}^*$

where I is the scattered intensity, $\ddot{A}$ and $\ddot{A}^*$ are the amplitude and its complex conjugate, respectively.[3] In general, the scattered intensity is measured by either a gas-filled or solid-state detector where a single photon triggers a measurable event such as gas ionization or current/light from a semi-conductor. In a simplified, ideal experiment each electron in the sample would scatter a photon. If these (ideal) scattered photons are only scattered once and are not attenuated a maximum scattered intensity would be obtained from the sample. Given the order of magnitude of Avogadro's number (10^{23}), typical densities and number of protons of most solid or liquid state systems, a very high flux of photons is required. Though, other factors such as detector efficiencies and scattering cross-sections demand an even higher number of photons, such a high flux is very hard to obtain. In the systems proposed here, the

problem is compounded further by the fact that the X-rays are necessarily attenuated by water in an *in-situ* cell and a low collection time is required to be able to collect time resolved data during the electrochemical process. Thus, a large number of photons are required for the scattering experiments proposed here. More precisely, a high brilliance is required as given by the equation:

(2.2) $$Brilliance = \frac{I}{\Delta\Omega A_c(0.1\%BW)}$$

where $\Delta\Omega$ is solid angle that the beam passes through, A_c is the focused cross-sectional area of the beam on the sample and the 0.1%BW is 0.1% of the energy range.[4] Equation 2.2 is a more appropriate measure of how well suited an X-ray beam is for a scattering experiment, as it accounts for the divergence of the beam as well as the energy range. Modern synchrotron radiation provides a brilliance 12 orders of magnitude higher than that of a traditional X-ray tube.[4] This brilliance is achieved by changing the velocity of charged particles (typically electrons) moving at relativistic speeds.[4]

Typically, electrons are generated by an electron gun and accelerated to speeds approaching the speed of light by alternating attractive/repulsive voltage to target plates that electrons pass through. Once at the required speed, the electrons enter a large storage ring, where they are maintained at relativistic speeds and used to generate X-rays. At the beamlines used for these experiments, X-rays were produced by either a bending magnet or an insertion device. In either device, electrons encounter a magnetic field causing the velocity to change; this change in velocity causes X-rays to emit along the original trajectory of the electron. A bending magnet applies a magnetic field orthogonal to the electron velocity, causing the electron bunch to follow a semi-circular orbit. As electrons follow the circular path, a broad spectrum of energies is irradiated.

Alternatively, an insertion device imposes a series of magnetic fields that cause the electron bunch to oscillate in one plane. Specifically, an undulator oscillates the electron bunch such that each oscillation produces semi-monochromatic X-rays. The following oscillation is timed such that semi-monochromatic X-rays are in phase with the ones from the previous oscillation. The resulting intensity is very high and semi-monochromatic with some coherence from the nature from which they were produced. Regardless of the device used, X-rays produced for scattering or radiography experiments here were inherently polarized because the acceleration of the electron is always in one plane. [4]

For scattering experiments performed here, the X-ray beam must be monochromatic because of the detectors used. A single energy is selected by scattering the beam from two opposing (perfect) crystals, which are spaced and tilted such that only one wavelength can exit. The monochromatic beam passes through several optics that serve to focus and collimate the beam on the sample (XRD) or detector (SAXS). The resulting monochromatic X-ray beam has very little divergence with a very high intensity suitable for time resolved experiments in an *in-situ* cell.

2.b General Scattering

Elastic X-ray scattering occurs when an X-ray causes an electron to (briefly) accelerate, emitting a radially propagating X-ray of the same wavelength.[4] The resulting X-rays intensity scattered by a single electron is given by Equations 2.1 and 2.2. Also, the corresponding intensity of the scattered wave depends on the polarization of the beam and is given equations:

(2.3) $I_e = r_e^2 I_o \cos 2\theta$ (parallel)

(2.4) $I_e = r_e^2 I_o$ (perpendicular)

where r_e is the classical electron radius, I_o is the incoming intensity and 2θ is the angle of intensity measurement.[1] Equations 2.3 and 2.4 depend on whether the electric field vector of the incoming X-rays is in the same plane as the angle of measurement (Equation 2.3) or perpendicular (Equation 2.4). In theory raw data collected from a synchrotron should be normalised by Equation 2.3 or 2.4 before any modelling or absolute intensity calibration can be performed; the measured intensity, $I(2\theta)$ must be normalized by Equations 2.3 or 2.4 to give the actual scattering cross-section, $d\Sigma/d\sigma$. Typical small angle scattering experiments presented here measure the intensity out to 1^o and are not calibrated, rendering Equations 2.3 and 2.4 unnecessary ($\cos 1^o \sim 1$). X-ray diffraction experiments were performed with a 1-D detector positioned perpendicular to the electric field vector. Consequently, the scattered intensity is not a function of scattering angle (Equation 2.4).

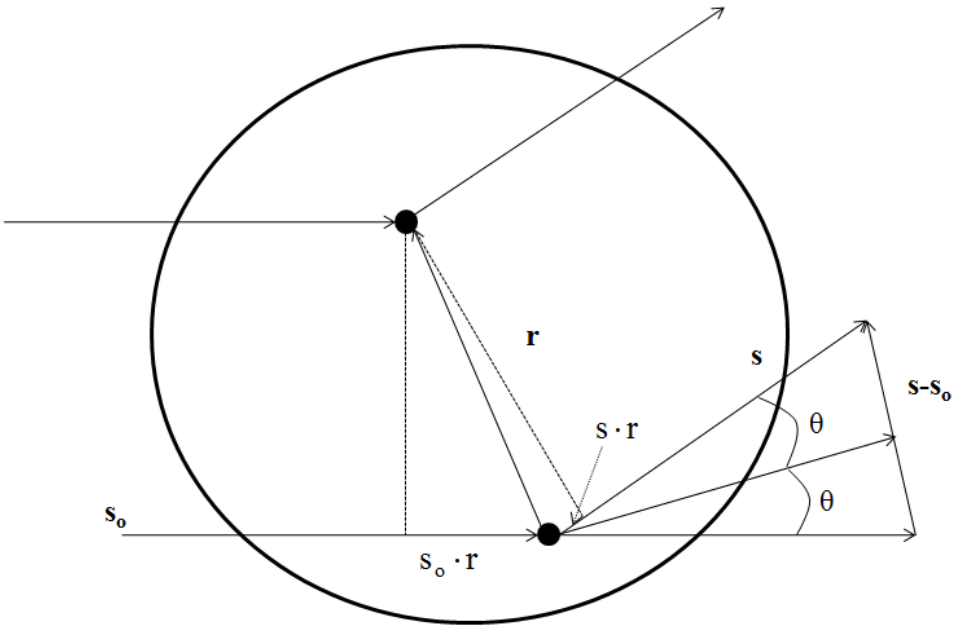

Figure 2.1 is a simplified diagram showing how two electromagnetic waves can either constructively or destructively interfere, depending on the angle of measurement (for a specific wavelength).

Figure 2.1 shows the scattering of an X-ray wavefront by two points in a particle a distance, **r**, apart where the resulting intensity is measured at an angle, *2θ*. When the X-rays are scattered from different points in the particle the interference of the waves will depend on the phase, ς, of the scattered X-rays (relative to each other), which is given by equation:

$$\varsigma = \frac{2\pi((\mathbf{s}-\mathbf{s_o})\cdot\mathbf{r})}{\lambda} = \mathbf{q}\cdot\mathbf{r} \quad (2.5)$$

where λ is the wavelength of the scattered X-rays, **s** and $\mathbf{s_o}$ are the incoming and scattered waves, **r** is the vector between the two scattering centres and the vector **q** is defined accordingly.[1-4] Figure 2.1 also shows that the magnitude of $\mathbf{s}$-$\mathbf{s_o}$ is given by the angle of measurement, *2θ*, resulting in the conventional equation for $|\mathbf{q}|$:

$$q = 2\pi\frac{2\sin(\theta)}{\lambda} \quad (2.6)$$

where the factors 2π and λ are included from Equation 2.5. The resulting amplitude from all points in an object can be calculated using complex notation:

$$\ddot{A} = \sum f e^{i\varsigma} \quad (2.7)$$

where *f* is the scattering power of each electron (assumed to be 1 for a free electron).[1-4] From Equation 2.7, the resulting amplitude will be *2f* if the value of ς is 0 or *nf*, where *n* is any integer. If scattering occurs from every electron in the particle, the resulting amplitude and intensity is calculated from the equation:

$$\ddot{A}(\mathbf{q}) = \sum f e^{i(\mathbf{q}\cdot\mathbf{r})} = \int \rho_e(\mathbf{r})\, cos\, \mathbf{q}\cdot\mathbf{r}\, dV \quad (2.8)$$

where $\rho_e(\boldsymbol{r})$, is the scattering length density at the vector **r** and the summation or integral is carried out over the entire irradiated volume;[1-3] for simplicity, the term electron density of a sample is used synonymously with the scattering length density for the remainder of this

thesis. Equation 2.8 is a fundamental equation for scattering when the wavelength of radiation is the same size or smaller than the structural inhomogeniety, defined by $\rho_e(\mathbf{r})$. When the particle has a centre of symmetry (at **r**=0), the imaginary portion of the phase factor will always be zero and can be replaced by the cosine (Equation 2.8).[2, 3] It can also be concluded that there is an inverse relationship between **r** and **q**, as constructive interference will only occur if scattered waves are in phase (Equation 2.5). If, for example, the function $\rho_e(\mathbf{r})$ represents a constant function over very large distances, constructive interference will only occur at extremely low angles. On the other hand, if the function $\rho_e(\mathbf{r})$ represents many very small particles, constructive interference will be possible at higher angles of measurement (Equation 2.6).

According to Equation 2.8, the phase factor must be either zero or $n2\pi$, where n is an integer for completely constructive interference. If there is an ordered structure between very small particles with a preferred distance between them, constructive interference will only occur at certain angles following Bragg's law:

(2.9) $$n\lambda = 2dsin\,(\theta)$$

where d is the distance between scattering centres. Instead of using a single function of $\rho_e(\mathbf{r})$ to describe the whole system, an alternative approach is to calculate the resulting amplitude as:

(2.10) $$\ddot{A}(\boldsymbol{q}) = \sum_j f_j(\boldsymbol{q}) e^{i(\boldsymbol{q}\cdot\boldsymbol{r}_j)} \sum_n e^{i(\boldsymbol{q}\cdot\boldsymbol{R}_n)}$$

where the electron density is described in terms of a small volume (e.g. unit cell) that is repeated over the whole structure of the object, described by the second term.[4] In Equation 2.10, every point in the system is defined by the vector $\mathbf{r}_j$, which is a trajectory from the

vector $\mathbf{R}_n$ (with respect to some centre of symmetry). In X-ray diffraction, the first summation would be a unit cell, where atoms have a preferred distance between them, while the second summation accounts for the entire crystal where the phase is multiples of 2π.[4] Because the distance between atoms is much smaller than the size of the crystal (~1μm), X-ray diffraction is performed at large angles. On the other hand, small angle scattering experiments are designed to probe slightly larger features accessible only at smaller angles, where the second term is neglected for a dilute system. In dilute small angle scattering, the first term is associated with the scattering from an individual particle. The second summation is then a constant for "randomly distributed" particles distanced very far apart, relative to their size; however, if the particles have a preferred distance, this term cannot be neglected and depends on **q** and the preferred distance.

2.c SAXS

2.c.1 Small Angle Scattering from a single particle

Small angle X-ray scattering (SAXS) is a technique used to characterize nanosized features, within a sample. Combining Equation 2.8 with Equation 2.1, the resulting fundamental equation for small angle scattering is given by the equations:

(2.11) $$I(\boldsymbol{q}) = \iiint \overline{\rho_e}^2(\boldsymbol{r}) e^{-i(\boldsymbol{q}\cdot\boldsymbol{r})} dV$$

(2.12) $$\overline{\rho_e}^2(\boldsymbol{r}) = \int \rho_e(\boldsymbol{r_1})\rho_e(\boldsymbol{r_1}+\boldsymbol{r})\, dV$$

where the electron density is defined by the vectors **r** and $\mathbf{r_1}$, $\overline{\rho_e}^2(\mathbf{r})$ is the Patterson function, and the integration in Equation 2.12 is carried out over the entire irradiated volume, *V*; the integration in Equation 2.11 is carried out over reciprocal space.[3] Equation 2.12 is an auto-correlation of the electron density function of a particle and its "ghost," shifted by the

vector **r** (reciprocal space) and provides a means to calculate the scattered intensity for simple particles, as opposed to squaring Equation 2.8. Figure 2.2 is two plots of the normalized Patterson function, $\gamma(r)$, (top) and the intensity, $I(q)$, calculated from Equation 2.11 for a spherical particle (Equation 2.18). Though Equation 2.11 can be used to numerically calculate the scattered intensity from any particle, it is computationally expensive, except for particles with spherical symmetry. Many analytical solutions to Equation 2.11 are also available[3].

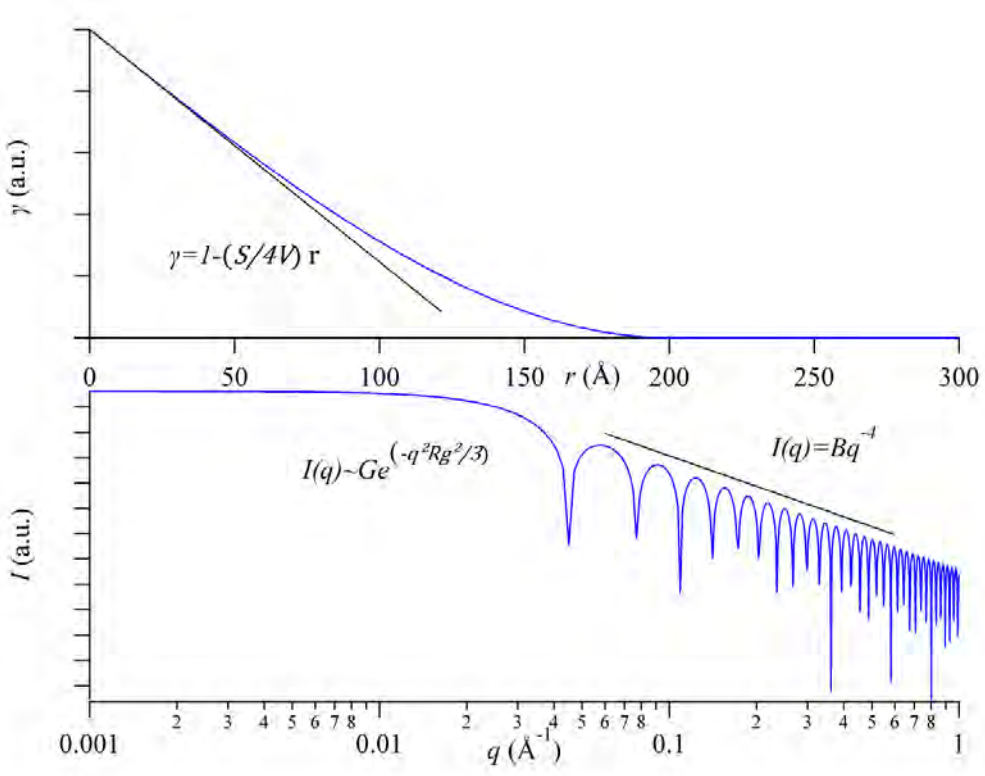

Figure 2.2 is plots of the normalised Patterson function, $\gamma(r)$, and the scattered intensity, $I(q)$ for a perfectly spherical, 20 nm diameter particle. The Patterson function is numerically calculated with Equation 2.12 and the scattered intensity is calculated with Equation 2.18. The normalised Patterson function $\gamma(r)$ is simply the patterson function, $\overline{\rho_e}^2(\mathbf{r})$, divided by its maximum value

Assuming no long range order between two points, at large $|\mathbf{r}|$, $\int \rho_e(\mathbf{r_1})\rho_e(\mathbf{r_1}+\mathbf{r})$ will tend toward a constant value known as the (volume) average electron density, $\langle\rho_e\rangle$. The function $\overline{\rho_e}^2(\mathbf{r})$ must therefore be different from $\langle\rho_e\rangle$ for small $|\mathbf{r}|$ to give a small angle scattering

signal. Thus, the scaling of Equation 2.11 will depend on the difference in electron density between phases, $\Delta\rho_e$ the total scattering volume, *V*, and relative volume fractions, *v*. In order to obtain absolute values of the intensity, a calibration must be performed on a sample of known scattering. The absolute intensity will depend on the irradiated area, solid angle of the detector, detector efficiency, sample transmission and thickness.[5] Equations presented in this chapter do not include these parameters, which are typically constant with *q*.[5] Thus, a general constant, *k*, can be used in front of Equation 2.11 when the scaling of the intensity is not important.

2.c.1.i Particles and Pores

Small angle scattering is a powerful technique for the study for small structures. As stated in Section 2.c.1, there must be structural inhomogenieties in the function $\rho_e(\mathbf{r})$, for small angle scattering to occur at experimentally accessible angles. If however, this function contains small voids surrounded by a matrix, one might think that there will be no scattering because there are no electrons in the voids; however, this would be incorrect.

The simplest system to illustrate this would be a block of metal with small holes within it (for example dealloying). The goal is to calculate the scattered intensity of the irradiated sample, I^s, the surrounding metal, I^m, and the voids, I^v; the calculation of I^s will be unity, as there is no long-range order in most small angle scattering systems. The resulting amplitude is given from Equation 2.10 by the equations:

(2.13) $\rho_e^s = v^m\rho_e^m + v^v\rho_e^v$

(2.14) $\ddot{A}^s(\boldsymbol{q}) = \int \rho_e^s e^{-i(\boldsymbol{q}\cdot\boldsymbol{r})}\, d\boldsymbol{r}$

(2.15) $\ddot{A}^v(\boldsymbol{q}) = \int \rho_e^v(\boldsymbol{r}) e^{-i(\boldsymbol{q}\cdot\boldsymbol{r})}\, d\boldsymbol{r}$

(2.16) $\ddot{A}^{v}(\boldsymbol{q}) = \int(\rho_e^s - \rho_e^m(\boldsymbol{r}))e^{-i(\boldsymbol{q}\cdot\boldsymbol{r})}d\boldsymbol{r} = \ddot{A}^{s} - \ddot{A}^{m}$

where the superscripts, *s*, *m* and *v* correspond to the entire system, metal and voids, respectively and all other symbols are the same as defined previously. Multiplication by the complex conjugate (Equation 2.1), the intensity of scattering from voids will be:

(2.17) $I^{v}(\boldsymbol{q}) = \left[\ddot{A}^{s}(\boldsymbol{q}) - \ddot{A}^{m}(\boldsymbol{q})\right]\left[\ddot{A}^{s^*}(\boldsymbol{q}) - \ddot{A}^{m^*}(\boldsymbol{q})\right] = I^{s}(\boldsymbol{q}) + I^{m}(\boldsymbol{q}) - \ddot{A}^{s}(\boldsymbol{q})\ddot{A}^{m^*}(\boldsymbol{q}) - \ddot{A}^{m}(\boldsymbol{q})\ddot{A}^{s^*}(\boldsymbol{q})$

where the value of $\ddot{A}^{s^*}(\mathbf{q})$ and $\ddot{A}^{s}(\mathbf{q})$ will be near zero at angles experimentally accessible.[2] It follows from Equation 2.17 that the function $I^{v}(\mathbf{q})$ will be the same as $I^{m}(\mathbf{q})$ and is the well known Babinet Principle of reciprocity[6]. This concept is extended to any system in which the electron density of the small inhomogenieties is smaller than that of the surrounding matrix. Of course, had the electron density of the voids and surrounding matrix been the same (but structurally different) there would be no observable scattering.

2.c.1.ii Anisotropy

Equations 2.11 and 2.12 are general equations for small angle scattering but can be numerically evaluated only for very simple systems. However, this equation can be simplified by noting that **q** and **r** are the scattering and reciprocal space vectors, respectively. It follows that only the component in **r**, relative to the plane of measurement, is relevant in the phase factor. Even when the particles are anisotropic, they can still be considered statistically isotropic if the particles are randomly oriented. The assumption of statistical isotropy requires every vector, **r**, to take every possible orientation with respect to **q**; this is the equivalent of the particles taking on every possible orientation. The phase factor, in Equation 2.11 can be averaged over the azimuthal angle, φ, and inclination angle, 2θ to give:

(2.18) $I(q) = N \int 4\pi r^2 \overline{\rho_e}^2(r) \frac{sin\,(qr)}{qr} dr$

where N is the total number of particles and r and q are now the magnitudes of reciprocal space and the scattering vector, respectively.[1-4] Equation 2.18 is a general equation for isotropic scattering of a monodisperse scattering population. It is worth mentioning that the Patterson function must also be isotropic, as well as the scattering population, and cannot be a function of either angle.

However, if the particles are anisotropic and have a preferred orientation Equation 2.18 cannot be used. One possible approach is to simply average the phase factor in Equation 2.11 over a direction in reciprocal space that corresponds to the azimuthal angle of measurement. A simple case would be a parallelepiped, modelled by the equation:

(2.19) $\ddot{A}(q) = \Delta\rho_e V_p \frac{sin\,(qa\alpha)}{qa\alpha} \frac{sin\,(qb\beta)}{qb\beta} \frac{sin\,(qc\delta)}{qc\delta}$

where V_p is the particle volume, a, b, c are the dimensions of the parallelepiped and α, β, δ are the cosines of the angles between each axis and the vector **q**.[2, 3] The resulting intensity is obtained by squaring the amplitude. Equation 2.19 is derived from Equation 2.11, with the principal assumption that there is no variation in the electron density within the particle. Scattering from both anisotropic and isotropic populations is markedly different and require careful consideration; for example: the scattered intensity from an oriented parallelepiped decays according to q^{-2}, instead of q^{-4}, and depends on the isotropy of the particles.

2.c.2 Modelling Approaches

There are many models that can be fitted to scattering data in order to obtain quantitative information such as particle size, shape, number, etc. Unfortunately, the complexities of the systems studied here prevent the use of simple form factors. Factors such as electron density fluctuations and polydispersity have similar effects upon the scattering curve and cannot be separated without the prior knowledge of one factor. Instead, it is normal for the scattering data to be broken down into key features, which qualitatively explain characteristics of the scattering population of interest. Namely, the so-called Guinier region, Porod region and Invariant can be used to characterise specific features of a scattering population. These are explained in detail and provide a foundation for the analysis presented here. Other effects, such as polydispersity, structure and electron density gradients and fluctuations are explained as deviations from ideal Guinier and Porod behaviour.

2.c.2.i Ideal Particles

2.c.2.i.1 Guinier Region

The Guinier approximation gives information about volume parameters such as the particle size. Because points separated by a large distance, **r**, will only constructively interfere at very low **q**, the Guinier approximation is valid only at very small($\mathbf{q} \cdot \mathbf{r}$). Starting from Equation 2.8, the Guinier approximation assumes the scattering particle has a centre of charge and is taken as the origin. In this case, the phase factor can be replaced by cos $\mathbf{q} \cdot \mathbf{r}$, since the amplitude will always be real. The cosine term can be expanded into a two term power series for values of $\mathbf{q} \cdot \mathbf{r}$ near zero and thus the low **q** region. Calculation of the scattered intensity is then accomplished by substitution of the Taylor series into Equation 2.11. The resulting approximation of the intensity at low **q** is:

(2.21) $I(q) \cong (\Delta\rho_e)^2 V_p^2 \left(1 - q^2 \frac{\overline{r^2}}{3}\right) \cong G e^{\frac{-q^2 R_{g_i}^2}{3}}$

where, *G* is a constant containing $\Delta\rho_e$, the electron density contrast between the particle and surrounding matrix and the particle volume, V_p, and $\overline{r^2}$ is the electron density weighted centre of mass of the particle, also known as the radius of Gyration, R_g.[2, 3] Equation 2.21, predicts a constant intensity at very low *q*, followed by a rapid decay proportional to e^{-q^2}, resulting in a "knee" in the scattering curve shown in Figure 2.2. The central approximation in Equation 2.21 is that the particle must have a centre of charge, as is usually the case (most all of the time).

2.c.2.i.2 Porod Decay

The Guinier approximation shows how the intensity of scattering from a single particle decreases at low $(\mathbf{q} \cdot \mathbf{r})$. Also, the Guinier approximation is valid regardless of anisotropy, whereas the Porod approximation is only valid for a statistically isotropic system. However, the Guinier approximation does not hold as *q* increases to larger values because of the assumption containing the expansion of the phase factor into a two term power series. Unlike the Guinier approximation, the Porod approximation focuses on small *r* values near the surface and thus gives a general approximation for scattering at high *q*. The principal assumptions behind this approximation are that the surface is smooth and well defined; this means that the radial electron density function must be a Heaviside (step) function and the surface itself is smooth.

Just as in the Guinier approximation, the phase factor in Equation 2.18 can be expanded into a power series for analytical integration. It can also be shown that for small *r*, the Patterson function follows a linear decrease proportional to $S/_{4V}$ and shown in Figure 2.2.

Substitution of the two previous assumptions into Equation 18 and integration results in the relationship:

(2.21) $I(q) \cong Bq^{-4}$

where *B* is a constant proportional to the electron density and surface area.[2, 3] Equation 2.21 predicts a power-law decay in q of q^{-4} and shown in Figure 2.2. A detailed derivation is avoided here and it should be pointed out that if the particle surface is not smooth, isotropic or the radial electron density function is continuous, Equation 2.21 would not be valid. Deviations from Equation 2.21 are considered in later sections.

2.c.2.i.3 Unified Equation and Form Factors

The Guinier and Porod approximations have proven to be robust for particles or pores of any shape, but neither one can model the entire scattering curve.[2, 3] A Unified Equation that brings the two approximations together is available. Using both of the above approximations, the scattered intensity can be modelled by the equation:

(2.22) $$I(q) = \sum_{i=1}^{N} \left(G_i e^{\frac{-q^2 R_{g_i}^2}{3}} + B_i e^{\frac{-q^2 R_{g_{i-1}}^2}{3}} \left(\frac{\left(erf\left(\frac{qR_{g_i}}{\sqrt{6}} \right) \right)^3}{q} \right)^{P_i} \right) + B_{kgd}$$

where B_{kdg} is the background scattering, i is the level, and P_i is the exponential power-law decay equal to four, following Porod's law.[7] The error function, within Equation 2.22, allows for the scattering curve to become dominated by the Porod approximation at higher q values.

When the particle/pore shape is known, analytical solutions to the scattered intensity are normally used and are commonly referred to as form factors, $|F(q,R)|^2$. These expressions

take in volume parameters, such as radius, thickness, length, etc. and produce a calculated intensity *vs.* q curve. Equation 2.22 can be fit to an entire scattering curve, allowing for slightly more flexibility than a classical form factor. If it is to be used as a strict form factor, the proper relationship between R_g and volume parameters must be used; for example, the radius of a sphere would be equal to $R_g\sqrt{5/3}$. In addition, the surface to volume ratio of the particle shape must be taken into account in the values of *G* and *B*.

2.c.2.ii Real Scattering Systems

2.c.2.ii.1 Polydispersity

For a dilute isotropic system, the contribution of each particle to the total scattered intensity is additive. When the distribution of particles is known, the scattered intensity can be modelled as:

(2.23) $I(q) = k \int D_n(R) V_p(R)^2 |F(q,R)|^2 dR$

where D_n is the number distribution of particles of size, R, V_p is the particle volume, $|F(q,R)|^2$ is the form factor and k is a general constant that depends on the contrast and volume.[3] Figure 2.3 is a plot of the intensity *vs.* q for a broad distribution of spheres and a single 35 nm ellipsoid with an aspect ratio of 0.3. The effects of polydispersity and particle shape are seen to broaden the Guinier knee as well as dampen the oscillations at high q. Larger particles can be visualized as a series of successive Guinier "knees" added together to give a broadened knee. Deviation of the aspect ratio also has a broadening affect of the Guinier knee. As the aspect ratio increases to values >10 two separate Guinier knees are separated by a power-law decay in q of q^{-1};[3] a further increase in the aspect ratio separates the two knees even further in q. Conversely, as the aspect ratio decreases toward zero, two

Guinier knees are again observed, which are separated by a power-law decay proportional to q^{-2}.[3] Though, particle shape and polydispersity may become distinguishable at extreme aspect ratios, both effects are indistinguishable if the system has particles of moderate aspect ratios and an unknown distribution, as both traces in Figure 2.3 are similar.

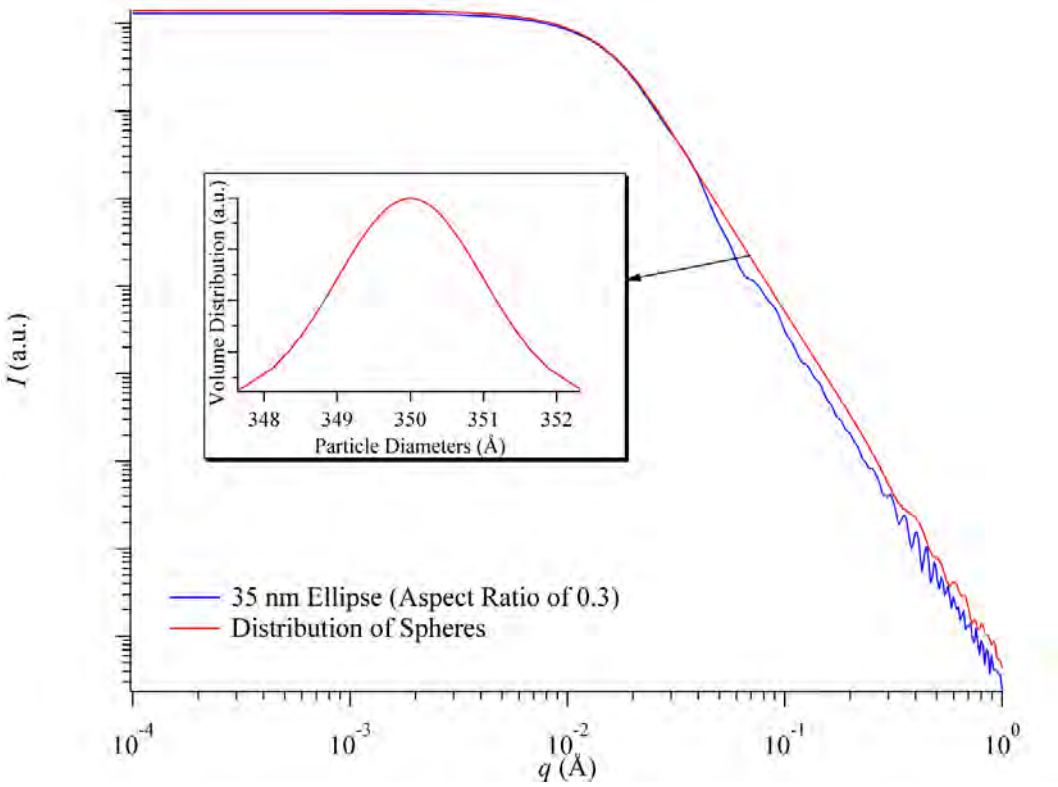

Figure 2.3 is log-log plot of the scattered intensity calculated from a single 35 nm ellipsoid particle (blue) and a distribution of particles (red). A Gaussian distribution is used for the distribution, with a mean of 20 nm.

Because both particle shape and distribution both have similar affects on the scattering curve, solving both from a single curve is not possible without *a priori* knowledge of these. In the case that the distribution is known, the scattering curve can be fit to a system of particles with either the same aspect ratio or a function of size. Alternatively, if an aspect ratio is either assumed or known, the distribution can be solved for, directly, from the discretized form of Equation 2.23. In this case, other methods such as the method of maximum entropy[8] can be

used. However, care must be taken as the contribution to the scattered intensity at low q can also be attributed to particle structuring, discussed in the following section.

2.c.2.ii.2 Particle Interference

As the number of particles in the system increases, the probability that they will be closer to each other also increases and hence the scattering probability for both particles is no longer independent. Two general cases are considered here and depend on whether the particles are correlated or not. In the case where particles or pores are separated by a specific distance, one might expect there to be a q value where the intensity peaks, instead of a steady monotonic decrease in q shown in Figure 2.3. The peak in intensity is characteristic of correlated systems only, where a preferred distance exists between inhomogeneities, just as in X-ray diffraction.[2, 3] Similar to the second summation of Equation 2.10, particle structuring is modelled by a structure factor, $S(q)$, which would be multiplied by the form factor in Equation 2.23. This is a complex topic and is not discussed further as it does not apply to any system considered here.

Small particles can also form clusters as a result of Van der Waals forces; agglomerates formed as a result of these relatively weak forces are commonly referred to as soft agglomerates.[16] In this case particles are very close to each other but without any order. Lack of order in the particle arrangement makes a mathematical calculation of the scattered intensity difficult, but possible. The structure of these particles can be described as a fractal like object.[9] The degree to which the particles that make up the agglomerate or aggregate are packed can be expressed in terms of the mass density, ρ_m, of the agglomerate:

(2.24) $\rho_m \propto R_g^{d_m-3}$

where R_g is the radius of gyration of the agglomerate and d_m is the mass fractal dimension[17],which ranges from 1 to 3. Therefore, as the value of d_m increases towards 3, the density, ρ_m, will also increase. Equation 2.24 defines the relationship between effective density of the agglomerate and the mass fractal dimension. The normalized Patterson function, $\gamma(r)$, can be described as:

(2.25) $\gamma(r) = h(r/R_g)r^{d_m-3}$

where $h(r/R_g)$ is a function that describes the overall agglomerate geometry and d_m is the mass fractal dimension.[9] It follows from Equation 2.25 that for a mass fractal dimension of 3, $\gamma(r)$ would represent the auto-correlation of a particle that is so tightly packed it would scatter as a single particle. Just as for regular particles, the scattered intensity would show a typical Guinier knee at low q that corresponds to the R_g of the entire agglomerate. However, as q increases, it can be shown that the scattered intensity would be:

(2.26) $I(q) \cong Bq^{-d_m}$

where the intensity decays according to the value of d_m, which can only be between 1 and 3.[9] It is worth noting that Equation 2.26 is not valid when the mass fractal dimension is exactly equal to 3, as Equation 2.21 or surface fractal scattering[10], would then apply. Scattering from agglomerates is well established in many systems that are prone to agglomeration. However, care must be taken when applying Equation 2.26, as mass fractal scattering typically requires a power-law decay to span over at least a decade in q in order for agglomerates to be considered fractal-like.[9]

2.c.2.ii.3 Deviations from Porod's law

Though Equation 2.21 has been shown to be a robust approximation for many systems, deviations from this behaviour are in every system discussed in this work. Deviations from Porod's law can be found in systems where: the electron density function is continuous at the particle/pore surface (i.e. not a sharp boundary), the surface is rough (on the Angstrom scale) or fluctuations in the electron density within the phase. Each of these effects are discussed below as they will be applied to SAXS results in this thesis.

2.c.2.ii.3.a Surface Gradients

Figure 2.4 is a plot of the scattered intensity calculated from a particle with a sharp boundary and one containing a gradient at the particle boundary with both electron density functions shown in the inset; the scattered intensity was calculated numerically, assuming a spherical shape. As the intensity approaches high q values, a decay much greater than Equation 2.21 is observed. In Section 2.c.2.i.2, Porod's law was derived by assuming a linear decay in the Patterson function at small r, which cannot be the case if the electron density function (blue) is convoluted. This concept has been applied mainly to semi-crystalline polymer systems where electron density gradients exists between lamellar structures[3, 11] and methods have been developed to estimate the thickness of the gradient.

The boundary layer thickness, σ, can be calculated from SAXS data by the method of Ruland[12] or Vonk[13]; the latter is not considered here, as it requires very high quality data. The general procedure outlined by Ruland starts with defining the Patterson function as a convolution of an ideal function with a smoothing function.[12] Because the scattered intensity is a Fourier transform of the Patterson function, the resulting scattered intensity is then the ideal scattering intensity multiplied by the auto-correlation of the smoothing

function. It can be shown that the scattered intensity for an isotropic system can then be approximated as:

(2.27) $I(q) = \frac{B}{q^4}(1 - \sigma^2 q^2)$

where B is the same as in Equation 2.21 and σ is the thickness of the boundary over which the electron density gradient exists.

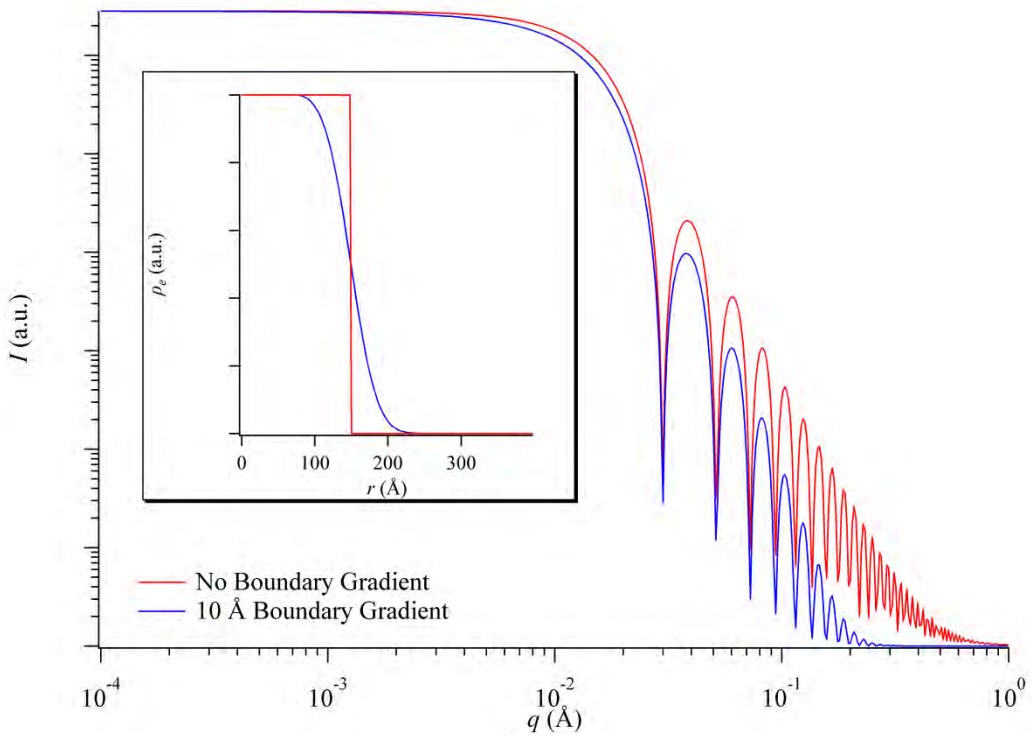

Figure 2.4 is a log-log plot of the scattered intensity from a spherical particle with a sharp boundary (red) and a particle with a smooth boundary (blue). Both particles have a radius of 30 nm and a constant background is included.

Equation 2.27 is applicable for isotropic systems and assumes that σ is much less than R_g of the particle; the limit on σ, has also been shown to depend on the smoothing function used[11]. Following the same procedure, it can also be shown that for an anisotropic system, the scattered intensity can be approximated as:

(2.28) $I(q) = \frac{B}{q^2}E_2(\sigma^2 q^2)$

(2.29) $E_2(\sigma^2 q^2) = \int_1^\infty \frac{e^{-\sigma^2 q^2 x}}{x^2} dx$

where all parameters are the same as defined before. For an isotropic system, the value of σ, is obtained by plotting Iq^4 *vs*. q^2 and fitting a straight line to the high q data. Alternatively, σ must be obtained by a least squares fit if the system is anisotropic. In either case, the scattered intensity will have a greater decay at high q, compared to an ideal system.

Until now, it has also been assumed that the particle or pore has a constant electron density. In reality, electron density fluctuations will occur in multi-component particles, as well as possible thermal fluctuations; the former can be visualized by either distributed impurities in the particle, while the latter would be where the average electron density in the particle changes with time (i.e. loss or gain of water). The overall effect of either fluctuation is to decrease the intensity decay at high q. Assuming no correlation between the density fluctuations between phases and the fluctuations are not a function of phase size or boundary shape, the observed intensity is given by:

(2.30) $I(q) = I_{ideal}(q) + \sum V_i \rho_{e_i} [Fl]$

(2.31) $[Fl] = \frac{\langle n_e^2 \rangle - \langle n_e \rangle^2}{\langle n_e \rangle}$ (isotropic)

(2.32) $[Fl_1] = k \frac{Fl_1}{q^2}$ (anisotropic 1-D)

where [Fl] is the contribution to the scattered intensity from the fluctuations of the scattering phase, n_e is the number of elections averaged over the volume of the phase, k is a constant and Fl_1 is the one dimensional density fluctuation. Equation 2.30 shows that these fluctuations can be considered a constant related to the average number of electrons in each phase. However, this is not the case for a one dimensional anisotropic phase. The values of

the fluctuations, Fl, are rarely of interest, but necessarily have to be accounted for. It is common[14] to simply subtract a constant from isotropic scattering data before data at high q is analyzed[3]. However, data collected at high q will inherently have a low signal and be very noisy, rendering a good fit to the data difficult. Nevertheless, fluctuations must be accounted for before any analysis on the scattered intensity at high q can be performed.

2.c.2.ii.3.b Surface Fractals

Another deviation from Porod's law is commonly referred to as "surface-fractal" scattering[10]. A surface fractal can be visualized as an infinitely rough surface such that the surface area depends on the length of measurement. For example, if one were to fold a ruler of size, *l*, over itself across the edge of Britain, the perimeter, P_s, would be simply *nl*., where *n* is the total number of times the ruler was folded. However, if the size of the ruler was decreased and the experiment repeated, the final value of the perimeter would increase according to:

(2.33) $P_s = nl^{d_s}$

where d_s is a non integer exponent; in this case the value of d_s would be 1.25[9]. If the coast had been perfectly smooth, d_s would be 1.[9] Thus, the island of Britain is described as a fractal.

Following the same logic as the previous example, the idea of a rough surface can be applied to small angle scattering. The derivation begins with relating the surface of the particles/pores to a fractal dimension. Now that the surface is mathematically defined, the normalized Patterson function, $\gamma(r)$, can be approximated at small *r*:

(2.34) $\gamma(r) = 1 - \frac{kr^{3-d_s}}{V}$

where k is a constant, r is the magnitude of reciprocal space vector, **r**, V is the volume and d_s is the surface fractal dimension[9]. Equation 2.34 bears a striking resemblance to what is obtained from Porod's law, where the initial decrease in $\gamma(r)$ was proportional to the surface to volume ratio. Using Equation 2.34, it can be shown that the scattered intensity decays at high q by the equation:

(2.35) $I(q) = Bq^{d_s-6}$

where d_s is again the surface fractal dimension and B is the same as in Equation 2.21. For a perfectly smooth surface, Equation 2.35 reduces to Equation 2.21 and d_s is 2. Conversely, if the particle/pore has a surface area similar to a tightly crumpled piece of paper, the value of d_s will approach 3. Characteristic surface fractal scattering follows a strict power-law decay that should, in principle, span over at least a decade in q[9, 10] and become negligible only when the background scattering becomes appreciable at high q.

Spatial electron density fluctuations, within a phase, will also cause a decrease in the intensity decay at high q and should be considered if positive deviations from Porod's law are observed[15]. This effect is similar to polydispersity effects where smaller features dominate over the surface scattering of larger particles. Accounting for the positive deviations can only be accomplished when information about the size and shape of these density fluctuations are known. However, density fluctuations, inside a particle cannot cause negative deviations from Porod's law.

2.c.3 Invariant

According to Equations 2.11 and 2.12, the Patterson function and scattered intensity are related by a Fourier transformation. It is also clear from Equation 2.12 that at r = 0, in

reciprocal space, the value of the Patterson function must be the square of the volume average electron density squared, $\Delta\rho_e{}^2$ times the volume, *V*, of the particle/pore. It follows that if *r* is taken as zero, the averaged phase factor in Equation 2.18 will be equal to one. If the inverse Fourier transformation is then applied to Equation 2.18, a unique parameter of the system is obtained, which will contain the volume averaged contrast and volume of the total scattering population. This parameter is referred to as the invariant and given by the equations:

(2.36) $Q = \frac{1}{2\pi^2}\int_0^\infty q^2 I(q)dq = kV\overline{\eta^2} = kV(\Delta\rho_e)^2 v_1$ (isotropic)

(2.37) $Q_\varphi = \int_0^\infty \int_{\varphi_1}^{\varphi_2} I(q)q^2 d\varphi dq = kV\overline{\eta^2} = kV(\Delta\rho_e)^2 v_1$ (anisotropic)

where *k* would be a calibration constant, φ_1 and φ_2 are the starting and ending azimuthal angle of the scattering sector, $\overline{\eta^2}$ is the volume average fluctuations in electron density and can be further simplified using the volume fraction of the dilute phase, v_1 and the difference in the electron densities, $\Delta\rho_e$; this simplification can only be used in a simple two-phase, dilute system.[3] Equations 2.36 and 2.37 are referred to as the "invariant" because they are parameters that do not change with the size or shape of the scattering population. Given any system, the value of *Q* will change only if either *V* or $\overline{\eta^2}$ changes. This concept is used extensively throughout the SAXS analysis.

2.d X-ray Diffraction

When the scattered intensity is measured at much higher angles, the technique is referred to as X-ray diffraction. In X-ray diffraction, the scattered intensity is a function of both terms in Equation 2.10, with the first term referring to the interferences of individual atoms in a unit cell. The second term extends over the entire crystal, composed of many unit cells. Because

of the strict order present in crystals, the $I(2\theta)$ curve contains a series of peaks whose positions in 2θ depend on the crystal structure and lattice parameters[1, 4].

In this thesis, X-ray diffraction is used to identify phases present based on the position of the intensity peaks. Because of the relatively low signal, a detailed refinement of the XRD patterns was not performed and a detailed discussion of X-ray diffraction is avoided. Instead, the diffraction peaks observed were compared to known diffraction patterns of possible crystal structures to identify the phases present. In addition, the peak magnitude and shape are analyzed to obtain the total crystalline volume and size.

2.d.1 Total Crystalline Volume

Just as in small angle scattering, the scattered intensity will increase with the scattering volume. A relationship between the scattered intensity and total salt volume can be made, for XRD patterns, with a few assumptions. The principal assumptions are that: the crystal size is small enough that absorption throughout the crystal can be neglected and the detector perfectly measures the intensity at each 2θ position[1]. The first assumption requires that the same intensity is scattered throughout the crystal and requires the crystal sizes to be on the order of 1 μm for the energies used here. Assuming instrumental effects do not change throughout an experiment, it can be shown that the total scattering volume is proportional to the integrated peak intensity by the equation:

$$V_c \propto \int_{2\theta_0-\epsilon}^{2\theta_0+\epsilon} I(2\theta)\, d2\theta \tag{2.38}$$

where ϵ is a sufficiently high value to encompass the entire peak area (~1°), $2\theta_0$ is the peak centre and V_c is the total crystalline volume. When Equation 2.38 is applied to the same peak

positions of XRD data obtained from different samples of the same phase, the relative amount of crystalline volume, V_c, in the two samples can be determined.

2.d.2 Crystallite Size

The size of the crystallite affects the width of the intensity peak, which corresponds to the *d*-spacing of a lattice plane by Equation 2.9. If the intensity is scattered from many consecutive planes, in a crystal, the scattered waves will destructively interfere, just as in small angle scattering, as the angle of measurement deviates from the $2\theta_0$ position. A quantitative argument can be formulated by considering the path length difference between scattered X-rays diffracted a distance, *l*, apart at small angular deviations from $2\theta_0$.[1] It can be then shown that the full width at half maximum, Δ, of the peak is related to this distance, *l*, by the Scherrer equation:

(2.39) $\Delta(2\theta) = \frac{0.9\lambda}{l\cos\theta_0}$

where *l* is the length of the crystal and all other parameters are the same as before. As with small angle scattering, the crystallite size is inversely related to the angle of measurement. When Equation 2.39 is applied to a diffraction peak, an estimation of the crystallite size can be obtained.

In reality, Equation 2.39 cannot be applied directly to the raw data because of instrumental broadening effects. To account for the instrumental broadening, a sample of known crystallite size can be used to determine the instrumental resolution function. As a first approximation, a Gaussian shape is assumed for the instrumental broadening and thus the real Δ can be obtained by the equations:

(2.40) $\Delta = \sqrt{\Delta_{raw}^2 - \Delta_0^2}$

(2.41) $\Delta_0 = \sqrt{\Delta_s^2 - \Delta_k^2}$

where Δ_{raw}, and Δ_s are the FWHMs of the raw data from the sample and standard, respectively and Δ_k is the estimated FWHM from the standard, calculated from Equation 2.39 based on known values of θ_0 and l and Δ_0 is the instrumental FWHM.[16] To obtain an estimate of the crystallite sizes, the value of Δ_0 is calculated from an NBS Silicon standard. Equations 2.39 through 2.41 provide a means to estimate the crystallite size. However, values of l obtained from Equation 2.39 should be considered an order of magnitude estimate, due to the necessary assumptions made.

To obtain the total salt volume and crystallite size, each peak was fit to a Voigt function[17], which is a convolution of a Gaussian and Lorentzian function. By fitting a Voigt function to each peak, the FWHM and integrated area are readily calculated from the diffracted intensity.

2.e Radiography

In a typical X-ray radiography experiment, the transmitted intensity is measured at different points in space, just as in medical or dental radiographs. The transmitted intensity, I_t, depends on how the incoming intensity is absorbed in the sample by the Beer-Lambert Law:

(2.42) $T_r = \frac{I_t}{I_o} = e^{-\left(\left(\mu/\rho\right)\rho_m x_t\right)}$

where, T_r is the transmission, μ/ρ is the mass absorption coefficient of the sample, ρ_m is the mass density and x_t is the sample thickness. From Equation 2.42, the measured transmission, T_r, is a function of μ/ρ and ρ_m, which depend on the sample composition. For a homogenous sample, μ/ρ and ρ_m are related to sample composition by the equations:

(2.43) $\mu/\rho = \sum m_i \left(\mu/\rho\right)_i$

(2.44) $\rho_m = \frac{1}{\sum \frac{x_{m_i}}{\rho_{m_i}}}$

where m_i and $\left(\mu/\rho\right)_i$ are the mass fraction and mass absorption coefficient of element, *i* and x_{m_i} and ρ_{m_i} are the mass fraction and density of phase *i*. Values of $\left(\mu/\rho\right)_i$ depend on the element and energy and are readily obtained from any number of sources. Thus, T_r depends upon the composition and thickness of the sample. For complex materials there is insufficient information to determine the composition, unless prior knowledge (i.e. electroneutrality) is incorporated into the model. In general, radiography measurements provide a means to visualize events in a system and also the potential for a more quantitative analysis.

2.f Electrochemical Methods

Electrochemistry is a very broad discipline and a complete review of Electrochemistry cannot be provided here. The electrochemical methods, used in this study, are affected by: dissolution kinetics, near-interface resistance and transfer of species from the interface to solution. Controlling or understanding the dissolution of the metal in solution is common to both pitting corrosion and AC electrograining and thus depends on the applied potential and concentration of species at the reaction plane[18]. In this section, a brief review of metal and solution potentials and current response are presented. Following the brief introduction, fundamental concepts of ionic transport are discussed, as they pertain to this study.

2.f.1 Potentials (Electrodes and Solution)

A potential is defined as the amount of work required to bring a test particle (electron for electric potentials) from infinity to its current state and can be used to characterise the current state of a system. As this test particle moves closer to its final state, the amount of work is calculated by integrating the force *vs.* distance curve (from infinity). In electrochemistry, the total force typically depends on the electric field, chemical composition, temperature and pressure[18]. It is common to refer to the electrochemical potential, $\tilde{\mu}_i$, which depends on both the chemical surroundings and electric field by the equation:

(2.42) $\tilde{\mu}_i = \mu_i + z_i F \Phi$

where μ_i is the chemical potential, z_i is the charge of species *i*, *F* is Faraday's constant and Φ is the electric potential[18]. Equation 2.42 provides the means to assess the potential of a species whose potential is influenced by its chemical and electrical surroundings. The chemical potential, in Equation 2.42, takes on its usual thermodynamic definition and is proportional to the natural log of its activity coefficient, Γ, and concentration, *C*, which are experimentally measurable parameters that depend on the chemical environment. The definition of the electrostatic potential, Φ, in Equation 2.42, must meet the required condition:

(2.43) $zF\Delta\Phi = \tilde{\mu}_i - \tilde{\mu}_j$

if phases *i* and *j* are chemically identical. Thus, there should be no potential difference between two identical electrodes that are submerged into a uniform electrolyte and electrically connected.

Because the potential, Φ, requires a "test charge," it is common to compare the potential of an electrode with that of a reference electrode; instead of comparing the electrical state to a free electron[18]. Common electrochemical experiments use a Potentiostat that can measure Φ, of the working electrode, relative to a reference. Although choosing this value of Φ is somewhat ill-defined with respect to the final state of the species (e.g. outer-Volta or inner-Galvani). However, it does satisfy equation 2.43; other definitions, such as a quasi-potential[18], also satisfy Equation 2.43. Thus, the chemical and electrical state of species in solution can be mathematically defined with experimentally determined parameters that depend on the species' environment.

2.f.1.i Electrode Potential

In an electrochemical cell, the potential of the working electrode can be controlled potentiostatically. Typically, the reference and working electrode are connected such that the potential difference between the two is controlled, with a negligible current between them. Figure 2.5 is a simplified schematic of a simple electrochemical cell, similar to those used in these studies. Because the Potentiostat controls the potential between the working and counter electrode, the actual potential at the working electrode is:

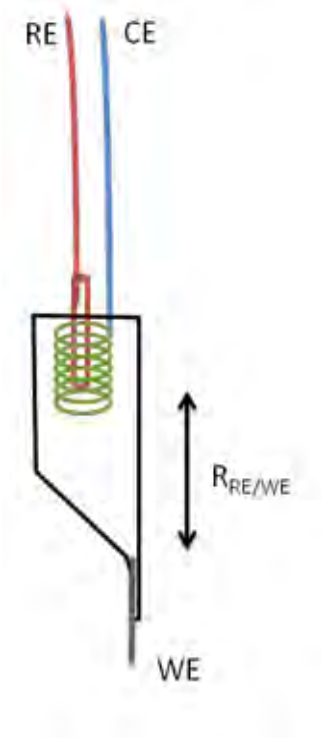

Figure 2.5 is a simplified schematic of an electrochemical cell, similar to that used in the artificial pit system.

(2.44) $\Phi_{we} = \Phi_{out} - iA_cR_{RE/WE}$

where, Φ_{out} is the output potential from the Potentiostat and, $R_{RE/WE}$ is the solution resistance between the reference and working electrode, iA_c is the current between the working and counter electrodes; all potentials are relative to the reference electrode. Thus, Equation 2.44

provides a relationship between the measured potential, Φ_{out}, and the actual potential at the working electrode when the values of iA_c and $R_{RE/WE}$ are known.

At open circuit, both the WE and RE, respond to the varying concentrations of species in solution. The potential of the WE and RE, in Figure 2.5, depend on the [Cl^-], but a simple application of the Nernst equation ignores the potential induced by concentration gradients between the WE and RE; a liquid junction region would exist between them, where the concentration changes[18]. This liquid junction region will cause an additional potential drop, depending on the nature of the junction[18]. The potential drop can be estimated when the nature of the system is known and is usually on the order of 10's of mV, for dilute systems (~.1M)[18]. Liquid junctions require extensive modelling, but can be neglected in the case of higher ionic concentrations[19] used here.

2.f.1.i Solution Potential

Similar to the potential of an electron in an electrode, the potential of an ion in solution depends on its chemical and electrical environment. However, as an ion is moved from infinity to its final state, it will alter the electrical and chemical environment. Thus, the potential of an ion in solution is theoretically more ambiguous than an electron in an electrode. Assuming that the dielectric constant of the solvent between ions remains constant, the potential of an ion can be related to its surroundings by the Poisson equation:

$$\nabla^2\Phi = -\frac{F\sum z_i C_i}{\varepsilon} \quad (2.45)$$

where F is Faraday's constant, z_i and C_i are the charge and concentration of ion i and ε is the permittivity of the solvent[18]. Equation 2.45 provides a relationship between the electrical state of the ion environment and gradient of the electric field, $\nabla\Phi$. It is clear from Equation

2.45 that if the solution is electrically neutral, the electric field will be a constant, as $\nabla^2\Phi = 0$. Also, keeping in mind the strict definition of the potential, if the solution is so dilute that the ion does not experience any electrical forces, the potential would be zero; its potential would necessarily be zero, as no electrical work would be required to bring the ion to its final state. In cases where the solution is not dilute, the absolute scaling of Φ depends on the boundary conditions where the potential can be assumed to be zero at one boundary or some value at the electrode, depending on the system. Because it is typically the change in potential that is needed for transport calculations, absolute scaling is somewhat arbitrary and can be scaled so that it is approximately equal to the electrode potential, at the reaction plane.

2.f.2 Current

In the systems studied here, a potential is applied to force the metal to dissolve, resulting in a measured current density, i. In this case, the current and electrode potential are related by a Butler-Volmer relationship:

(2.46) $$i = i_0 \left[e^{\left(\frac{\Phi-\Phi_0}{\alpha_a}\right)} - e^{\left(\frac{\Phi-\Phi_0}{\alpha_c}\right)} \right]$$

where Φ_0 is the potential at a zero net current flow, at the same conditions as Φ, α_a and α_c are kinetic parameters and i_0 is the exchange current density, which depends on the concentrations of the reactants and products at the reaction plane. For large overpotentials (Φ- Φ_0), only one exponential term in Equation 2.46 is dominant and Equation 2.46 reduces to a Tafel relationship, where the first exponential term is dropped for large negative overpotentials and the second exponential is dropped for large positive potentials.

Equation 2.46 is a powerful relationship that predicts the amount of current passed, when i_0, Φ, Φ_0 and α_a or α_c are known. In general, the kinetic parameters, α_a or α_c depend on electrode

reaction and do not have a strong dependence on Φ, Φ_0 or the concentration of reactants or products at the reaction plane[18]. The value of Φ_0 is expected to change with the reactant and product concentrations at the reaction plane. Neglecting the liquid junction between the working and reference electrodes, the value of Φ_0 could be calculated by the Nernst equation:

$$\Phi_0 = \Phi_0^0 - \frac{RT}{nF} ln \prod C_i^{s_i} \Gamma_i^{s_i} \quad (2.47)$$

where Φ_0^0 is the standard potential compared to some reference, R is the gas constant, T is the temperature, n is the number of electrons produced by the dissolution reaction, F is Faradays constant and C_i, Γ_i and s_i are the concentrations, activity coefficients and stoichiometric coefficients of the reaction species, respectively[18]. According to Equation 2.47, the value of Φ_0 varies with the concentration and activity coefficient. The general trend in Equation 2.47 can be experimentally observed if, for example, an actively dissolving metal is placed in galvanostatic control at zero current, immediately following anodic dissolution. In this case, the measured potential will increase, as the product species diffuse away from the reaction plane.

Finally, the value of i_o depends only on the concentration of ionic species, at the reaction plane by the relationship:

$$i_o = k \prod C_i^{\xi_i} \quad (2.48)$$

where k is a constant and C_i and ξ_i are the concentrations and reaction orders of species i. Equation 2.48 is a general relationship used to characterize the concentration dependence of species participating in a given electrochemical reaction. As an example, previous work has shown that value of i_o for a dissolving nickel metal system is related to the H^+ concentration and Cl^- concentration, with the respective reaction orders of 1 and 0.5.[19]

Equations 2.46 through 2.48 serve to show that the current response depends on the applied potential and the concentration of ionic species at the reaction plane. In the experiments performed here, the potential is measured with a Potentiostat. In systems where a large resistance is present between the working and reference electrode, Equation 2.44 would need to be employed to convert the measured potential to an actual potential; however, the resistance between them must then be known. On the other hand, solving for the concentration of ionic species at the reaction plane is non-trivial and requires knowledge of the ionic transport away from the reaction plane.

2.f.3 Ionic Transport

Ionic transport is an irreversible process by which ions have a net motion as a result of particular driving forces. In this study, the change in concentration of ionic species as a function of time and space is important. Therefore a brief introduction to ionic transport is presented starting with the simplest case of a very dilute system, followed by transport in a concentrated solution, with a focus on additional factors that are not accounted for in the dilute approach. For simplicity, a one-dimensional system is assumed, whereby the concentration depends on the distance, *x* and time, *t*; no convection is assumed in this system.

2.f.3.i Dilute System

For a dilute system of dissociated ions, the driving forces for transport are the concentration gradient (Fick's first law) and the electric field, which may be described by the Nernst-Planck-Poisson equations, a system of non-linear partial differential equations given by

(2.49) $$\frac{\partial C_i}{\partial t} = \frac{\partial}{\partial x}\left(z_i u_i F C_i \frac{\partial \Phi}{\partial x} + D_i \frac{\partial C_i}{\partial x}\right)$$

(2.50) $\frac{\partial^2 \Phi}{\partial x^2} = -\frac{F \sum z_i C_i}{\varepsilon}$

where u_i is the mobility of species *i* and all other symbols are the same as before. For a system consisting of two species, equations 2.49 and 2.50 may be used to solve for each concentration, *C* and the potential, *Φ*, as a function of *x* and *t* by any number of numerical approaches, with the correct boundary conditions. The first term in the parenthesis in Equation 2.49 is a migration term, while the second is a diffusion term. The mobility, *u*, is a measure of the average velocity of a species in the presence of the electric field, while the diffusion coefficient has a similar meaning but in the presence of a concentration gradient. As a first approximation, The Nernst-Plank-Poisson equations are commonly applied to systems to obtain a general idea about the concentration profiles during an electrochemical transient.

2.f.3.ii Concentration Effects

Although Equations 2.49 and 2.50 are very powerful, they contain a number of assumptions that are not realistic when the electrolyte concentration increases (>0.1 M). The principal assumption in the Nernst-Plank approach is that ions only experience long range electrostatic forces. As the concentration of ions increases, short range forces must also be taken into account. In this section an overview of how short range forces are taken into account is presented starting with ion mobilities and diffusion coefficients, followed by the effect of other ions and the solvent.

2.f.3.ii.a Mobility and Diffusion

Both *u* and *D* are concentration dependent values, and in general decrease with increasing concentration[20]. Values of *D*, as a function of concentration, are readily available in the literature for many systems (for example, $NiCl_2$[21]), and simple interpolation of experimentally determined values is possible. In dilute systems, the Nernst-Einstein relation is used for the mobility where $u = {D}/{RT}$; however, this relationship is not valid for concentrated systems. Although mobilities are not directly experimentally accessible, the conductivity, κ, is and is related to the ion mobility by the equations:

(2.51) $\kappa = \Lambda z_+ s_+ C$

(2.52) $\Lambda = |z_+|F^2 u_+ + |z_-|F^2 u_-$

where Λ is the equivalent conductance of the salt, *C* is the concentration of salt and all other values are the same as before. Using tabulated values of κ, the value of Λ is readily calculated. The mobility of each ion can be calculated with knowledge of the transference numbers and Equation 2.52. The transference numbers are commonly tabulated with the conductivity and provide a measure of how much current is carried by each ion. Therefore, the mobility of each ion can be calculated from experimental data. However, values reported for *D* and *u* are normally only available for experimentally accessible conditions, such as below saturation. For higher concentrations, a theoretical approach can be taken to calculate *D* and *u*, but this is non-trivial and requires assumptions about the nature of the close range interactions [22, 23].

2.f.3.ii.b Relaxation and Electrophoretic effects

As the ions move through a concentrated solution, they will encounter other ions, which results in an ionic cloud of oppositely charged particles around the central ion. As the central ion moves, its cloud becomes distorted resulting in an opposing force on the central ion. This effect is known as relaxation. Another concentration effect is commonly referred to as the electrophoretic effect. This effect is a hydrodynamic effect, whereby the force that opposes transport comes from the viscosity of the solvent and transport of other ions. The electrophoretic effect and relaxation effect can be modelled by assuming that ions are charged "hard spheres." for concentrations up to 1 or 2 M.[22] Finally, ionic transport in such a concentrated system would be modelled by the equation:

$$\frac{\partial c_i}{\partial t} = \frac{\partial}{\partial x}\left(u_i \sum_j O_{ij}(\mathbf{v}_i - \mathbf{v}_j)\right) \quad (2.53)$$

where $\mathbf{v_i}$ and $\mathbf{v_j}$ are the relative velocities of species *i* and *j*, respectively and *O* is a 2-*D* matrix that contains the friction coefficients between species *i* and *j*.[18] Thus, the values of O_{ij} would account for relaxation and the electrophoretic effect[22, 24, 25].

As the concentration of the solution increases beyond *ca* 3 M, the conductivity of many dissolved salts passes through a maximum, indicating a drastic change in the ion mobility. This phenomenon has recently been modelled by assuming the formation of a pseudo-lattice, whereby the ions form a semi ordered structure[23]. In this case, transport of ions occurs through a so called "hopping" mechanism, where ions jump from one cell to the next as opposed to classic Brownian motion[23].

Recent work has provided a framework on how to deal with concentration effects. Modelling concentrated solution transport, via Equation 2.53 has not been performed in this study.

Although no intensive modelling is reported, factors that affect the mobility in concentrated solutions serve to provide an understanding of experimental results obtained in the artificial pit system.

2.f.3.iii Tortuosity/Porosity

Departures from normal transport occur when transport is limited to pores only. Classically, the porosity, ϕ, is the volume fraction[26] or area fraction[27] of pores to the total sample volume or area. The value of ϕ can then be used as a correction factor for the flux of a species in transport or conductivity calculations. For example, Equation 2.49 would be multiplied by ϕ to account for the reduced area available for transport. Alternatively, an effective diffusion coefficient, D_{eff}, can be used and calculated by the equation:

(2.54) $D_{eff} = D\phi$

where the value of D_{eff} is less than D, accounting for a decrease in the mass transport[28]. Although geometrically correct, the porosity assumes that the pores are perfectly straight, which is usually not the case.

When the pores are not straight and the mass is forced to take a tortuous path, the tortuosity, τ, is used to characterize the pores and defined by the equation:

(2.55) $\tau = \frac{L_p}{L}$

where L_p is the total length of the pore and L is the length of the porous membrane. From Equation 2.55, $\tau \geq 1$ because L_p is usually greater than, but never less than, L. Similar to the porosity, the tortuosity can be used to calculate an effective diffusion coefficient, D_{eff}, by the equation:

(2.56) $D_{eff} = \frac{D\phi}{\tau^2}$

where again, the value of D_{eff} is necessarily lower than D, as expected[28]. Equation 2.56 was derived for a packed bed, commonly used in chromatography where migration does not occur. In the presence of migration or conductivity, Equation 2.55 has been used as a first approximation[27], assuming the effect of porosity is the same as that with diffusion. Although Equations 2.55 and 2.56 were derived for diffusion only, it is expected that the presence of porosity and tortuosity will decrease the transport of species through a porous, non-conducting layer.

CHAPTER 3
Experimental Methods

Experimental methods for the AC electrograining and artificial pit systems are covered in this chapter. In order to perform experiments on both systems at a synchrotron, custom designed cells were used in order to obtain quality data. As mentioned in Chapter 2, a high flux of X-rays that interact with a maximum amount of sample is required for a good signal. However, X-rays are also absorbed by electrolyte solutions, which results in an optimization problem of too much sample (full attenuation) and too little sample (weak signal). Experimental cells for each system are presented in this chapter, along with the conditions used in each individual experiment.

Experimental data obtained from the SAXS, radiography and potential response experiments resulted in a very large amount of data, which was further processed so that it could be concisely presented. All data was manipulated by programs written in either Matlab or Igor Pro. The algorithm used in each case is also presented to show how the data were treated; the actual coding is very long and is not shown in this thesis for brevity. Thus, data processing is also incorporated into this chapter for reference in later chapters.

3.a Design Considerations and Methodology

3.a.1 AC Electrograining

Electrograining is a process by which two samples are simultaneously electrograined, which allows for small angle scattering data to be collected from both to increase the signal. The idea behind this setup is to obtain SAXS data from two layers of smut formed on the working and counter electrode, giving data representative of a large area of smut. This setup is only possible for small angle scattering, as the sample to detector distance is much larger than the space between electrodes. A working distance of 1 mm, between electrodes, was chosen to minimize beam attenuation in the electrolyte, prevent arcing and to accommodate for the removal of gas bubbles during electrograining. In most experiments, 40 µm foils were used to provide enough substrate to grain for long times and to minimize beam attenuation; 250 µm sheets were also used to see if the initial substrate would affect the SAXS data.

It has been shown previously that AC electrograining is a mass transport controlled process[29]. Cell flow between the electrodes proved to influence the results and does vary between experiments. The first and second experiments used a constant fluid velocity of ~ 3 mm s^{-1} that allowed for fresh electrolyte at the surface and a constant flow from a 60 ml (maximum syringe pump capacity) syringe throughout the entire experiment. Later experiments required a fluid velocity of 10 mm s^{-1} during electrograining, to effectively remove gas bubbles on the electrodes to obtain a reproducible potential response between samples. In these experiments, a higher flow was obtained by turning the pump off during the quiescent period so that a 60 ml syringe could still be used. *In-situ* transmission experiments were performed with the X-ray beam in the centre of each electrode.

3.a.2 Artificial Pits

Salt films are investigated in an artificial pit system, whereby a 50 um foil is dissolved between kapton tape and epoxy. In this cell, the X-ray beam was positioned on the interface to obtain information from that portion of the sample. The interface was easily found, as the mass absorption of nickel is an order of magnitude greater than any nickel chloride salt. X-ray diffraction, small angle scattering and radiography were then performed in transmission during nickel dissolution by constantly moving the sample upwards to maintain a specified interfacial transmitted intensity. A thickness of 50 μm nickel foil proved to attenuate nickel metal scattering sufficiently, while giving a reasonable X-ray diffraction signal from the salt film.

3.b Experimental Methods

3.b.1 AC Electrograining

3.b.1.i Cell Setup

In-situ SAXS experiments were carried out using the flow cell shown in Figures 3.1a and 3.1b. Cleaned aluminium foils (or sheets) were taped with Kapton tape to the PEEK and aluminium blocks. Holes of 4 mm to 6 mm were punched into the Kapton tape to expose the foils to the electrolyte. A current density of 21 A dm^{-2} was used in all experiments, as this current density is high enough to form smut but low enough to prevent complete removal of the Al foil. The aluminium foils protruded on opposite sides of the sample and connected to the potentio-galvanostat as the working and counter electrodes. The PEEK and aluminium block were separated by a 1 mm PTFE spacer to allow for flow of electrolyte through the

cell. The entire cell was assembled using parafilm as a gasket between the PTFE spacer and blocks (Figure 3.1a).

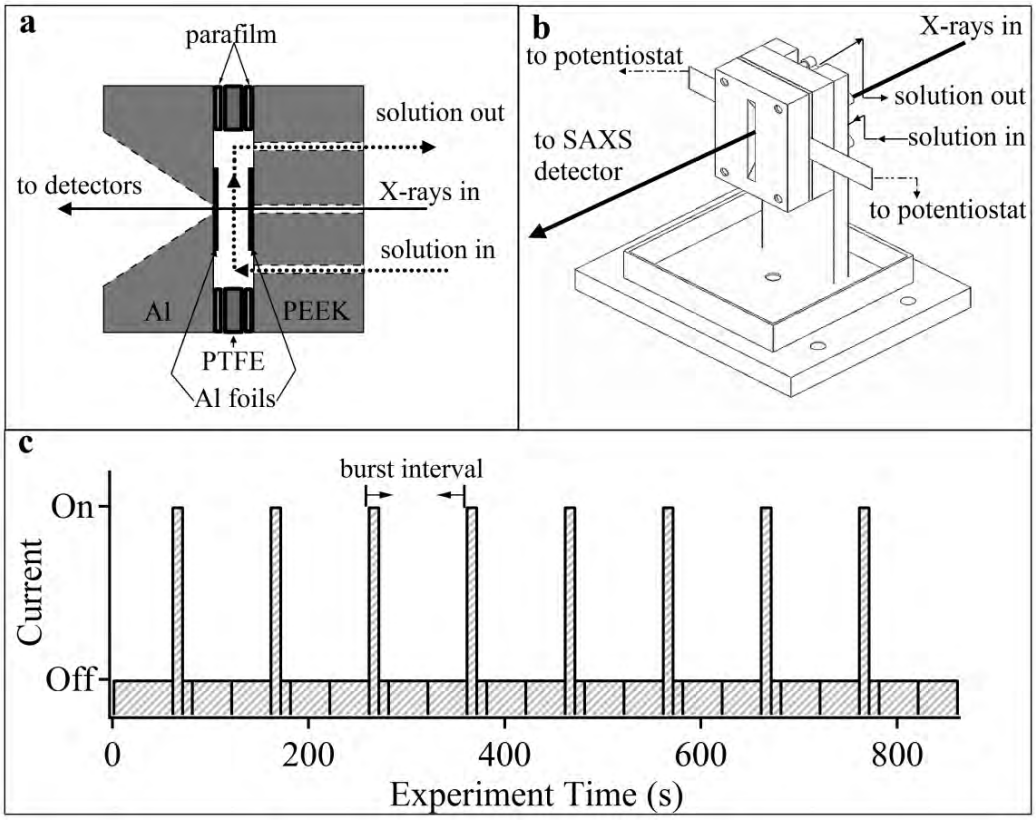

Figure 3.1a is simplified cross-section of the flow cell used in the electrograining experiments, showing the path that the X-rays take through the cell. Figure 3.1b is a drawing of the actual assembled cell as it sits on the beamline, showing how the potentiostat and syringe pump were connected to the cell. Figure 3.1c is the timing sequence for the *in-situ* experiments performed in the first session. In the timing sequence of Figure 3.1c, the potentiostat is triggered for 10 s (electrograining is on), followed by a quiescent period of 90 s. In later experiments the quiescent period was changed, but the general sequence remained the same.

Ex-situ samples were prepared using 250 µm AA1050 sheets in a slowly stirred 1.7 l electrolyte bath; a much larger (3.14 cm^2) exposed surface area was used; these experiments were performed by collaborators at the VUB. The exact same potentio-galvanostat setup was used to apply the AC current. The principle differences between the *ex-situ* and *in-situ* electrograining is the sample size, material and convective transport at the electrode surfaces.

3.b.1.ii Synchrotron Setup

Small angle scattering data was collected from two different beamlines and four separate sessions. The following sub-sections describe the experiments performed during each session. All *in-situ* experiments used the flow cell in Figure 3.1, with the only difference being the final experiments where a Ag/AgCl reference micro-electrode was used inside the cell. All *ex-situ* experiments were performed on samples that were simply taped to a sample holder, whilst data was collected.

3.b.1.ii.1 First SAXS Session

In-situ and *ex-situ* SAXS experiments were performed on AC electrograined samples at the Beamline BM-26 DUBBLE at the ESRF, using a q range of $0.006\ Å^{-1} \leq q \leq 0.15\ Å^{-1}$. In the first and final session an X-ray energy of 12 keV[30] was used while 15 keV was used for the second experiments. A beam size of 2 mm(h) by 0.05 mm(v) was used in all SAXS experiments. In the first session 40 µm aluminium foil (Agfa) samples were electrograined in 0.34 M HCl, 0.32 M HNO_3+0.0033 M $Al(NO_3)_3$ and 0.34 M HCl + 0.9 g l^{-1} of disodium phenyl phosphate dehydrate (DPPD). Scattering data was collected from foils electrograined *ex-situ*, scraped powder and *in-situ*, using the cell in Figure 3.1. The purpose of these experiments was to observe and characterize small angle scattering from within the smut, as well as any changes *in-situ*.

Scattering data acquisition was synchronized[31] to trigger the potentio-galvanostat in order to collect SAXS data exactly during the 10 s burst of electrograining and in a following quiescent period of 90 s using the timing sequence shown in Figure 3.1c. During the quiescent period, a single 10 s frame was collected immediately after electrograining, followed by two 40 s frames.

3.b.1.ii.2 USAXS Experiments

After completion of the first session, the source and structure of the scattering population could not be confirmed with the limited *q* range of SAXS and ultra small angle X-ray scattering (USAXS) experiments were performed on samples electrograined *ex-situ*. Experiments were performed at beamline 32-ID at the Advanced Photon Source (APS) using a *q* range of 0.0001 $Å^{-1} \leq q \leq 1\ Å^{-1}$ and an X-ray energy of 12 keV[32] and a beam size of 1 mm(v) by 2 mm(h). The purpose of these experiments was to separate scattering from the electrograined surface and to evaluate any structuring, within the smut, which can only be observed at very low *q*.

3.b.1.ii.3 Second SAXS Session

In-situ experiments were continued with the second session of beamtime, at a *q* range of $0.006\ Å^{-1} \leq q \leq 0.15\ Å^{-1}$ and an X-ray energy of 15 keV. The primary purpose of these experiments was to collect more data *in-situ* at different electrograining conditions that included addition of different concentrations of DPPD and different frequencies. In addition, 200 um sheets were used instead of foils and longer quiescent periods of 100 s were used. The same triggering setup and electrochemical setup was used in this session as in the first. Due to detector and signal problems, very little data is usable from these experiments and only transmission experiments at 50 Hz in 0.34 M HCl and 0.34 M HCl + 9 g l-1 DPPD are presented.

3.b.1.ii.4 Final SAXS session

Third and final session of experiments were focused on correlating gas retention in the smut with the measured potential, impedance and surface/smut morphology; experiments were again performed at the DUBBLE beamline at a q range of 0.006 $Å^{-1} \leq q \leq 0.15$ $Å^{-1}$ and an X-ray energy of 12 keV using the cell shown in Figure 3.1a. Conditions used were based on experiments that were performed at the Vrije Universiteit Brussel (VUB), prior to beamtime, where the cell in Figure 3.1a was used, except that a Ag/AgCl micro-reference electrode was placed ~1 cm under the working electrode; these experiments were performed using the same electrochemical setup as in the first session.

Aluminium foil (0.04 mm) samples were electrograined at two different frequencies (50Hz and 100Hz) in: 0.34M HCl, 0.34M HCl + 0.3M acetic acid, 0.34M HCl + 0.03M citric acid , 0.34M HCl + 0.03M DPPD. A TTi TGA 1240 function generator was used to supply an AC waveform to a Wenking HP 400 potentiostat, which in-turn supplied the appropriate AC signal to the working and counter electrodes. Each electrode potential was measured *vs.* a Ag/AgCl electrode (Cypress) and recorded using Labview software via a NI SC-2435 A/D converter.

Following results of previous work[33], the experimental methodology was to electrograin for 10 s and wait 40 s; a flow of 10 ml min^{-1} was initiated 5 s before the 10 s electrograining period and stopped at the beginning of the 40 s quiescent period to facilitate slow gas release and minimize smut dissolution. This sequence was repeated eight times, with a single 10 s image obtained during electrograining, followed by 20 consecutive 2 s frames.

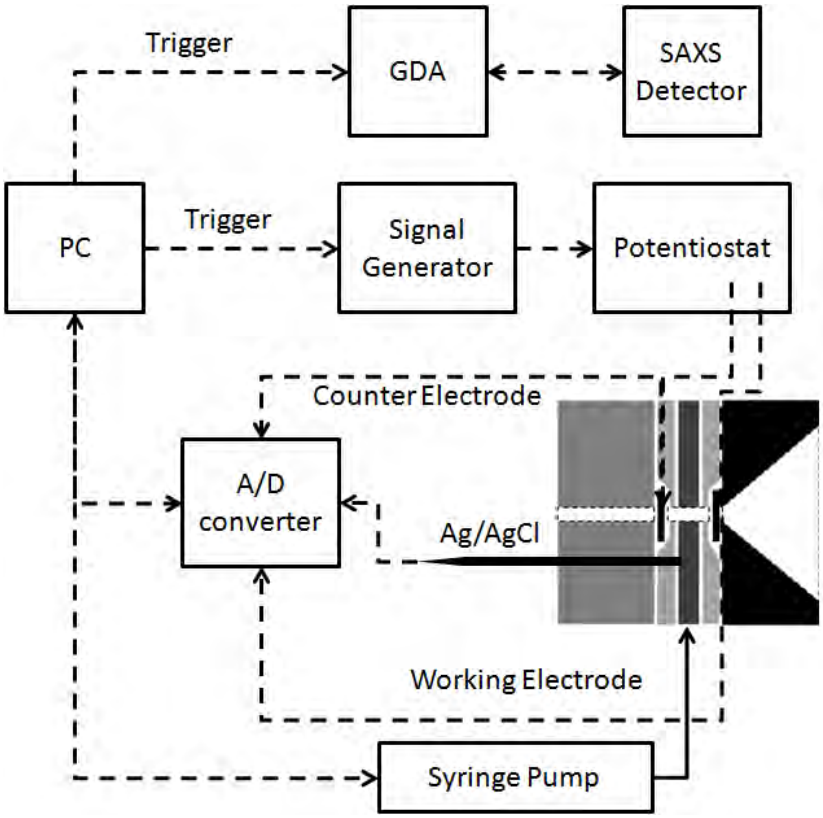

Figure 3.2 is a simplified flow diagram describing how synchronization of the electrograining, potential measurements and SAXS data acquisition was accomplished [31]

A timing sequence, similar to that shown in Figure 3.1c, was entered into a MATLAB macro and executed from a PC by providing the necessary triggers to the syringe pump, GDA and function generator, shown schematically in Figure 3.2. Upon receipt of the trigger, the GDA software began collection of a single 10 s image (during the electrograining) and 20-2 s images. Simultaneously, the function generator sent a sinusoidal AC waveform to the potentiostat that initiated the electrograining inside the *in-situ* cell; collection of the potential response was started manually from the same PC just before the experiment and was not triggered, as it is obvious when electrograining was occurring and when it stopped. After a quiescent time of 40 s, the sequence repeated eight times for a total electrograining time of 80 s.

3.b.1.iii Data Analysis

All SAXS data presented were collected as images. In all *in-situ* experiments a 60 s frame was collected from the ungrained foils in the cell (before electrograining) and subtracted from subsequent frames to remove scattering from the Al substrate and cell according to the equation:

$$SAS2D_i = \frac{\left[\frac{I_i(q)}{I_{o_i}} - \frac{I_{firstframe}(q)}{I_{o_{firstframe}}}\right]}{T_{s_i}} \quad (3.1)$$

$$T_{s_i} = \frac{I_{t_i} / I_{o_i}}{I_{t_B} / I_{o_B}} \quad (3.2)$$

where, $I_i(q)$ and $I_{\text{firstframe}}(q)$ are the raw images of the i^{th} frame and first frame of the sequence, I_{o_i} and $I_{o_{firstframe}}$ are the respective incoming X-ray intensities, I_{t_i} and I_{t_B} are the transmitted intensities from frame i and the previous burst frame, I_{o_B} is the incoming intensity during the previous burst frame and T_s is the relative sample transmission. In a normal calibration, the value of T_s would be relative to the sample plus holder.[5] However, if the non-grained aluminium is considered to be part of the holder, the transmission will be very near one, as the deposited smut is mostly water and a thickness on the order of 1μm.[34-36] Thus, the transmission used is relative to the burst frame (tall bars in Figure 3.1c) of each burst interval. This is done to correct for the lack of bulk solution bubbles after the burst, which causes the scattered intensity from the first foil and incoming intensity to the second foil to be slightly lower during the quiescent period. The units of the resulting scattering cross-section obtained from Equation 3.1, would normally be cm^{-1}. In this paper arbitrary units are used

because the wet smut layer thickness is unknown and a calibration was not performed, but normalized to each respective burst.

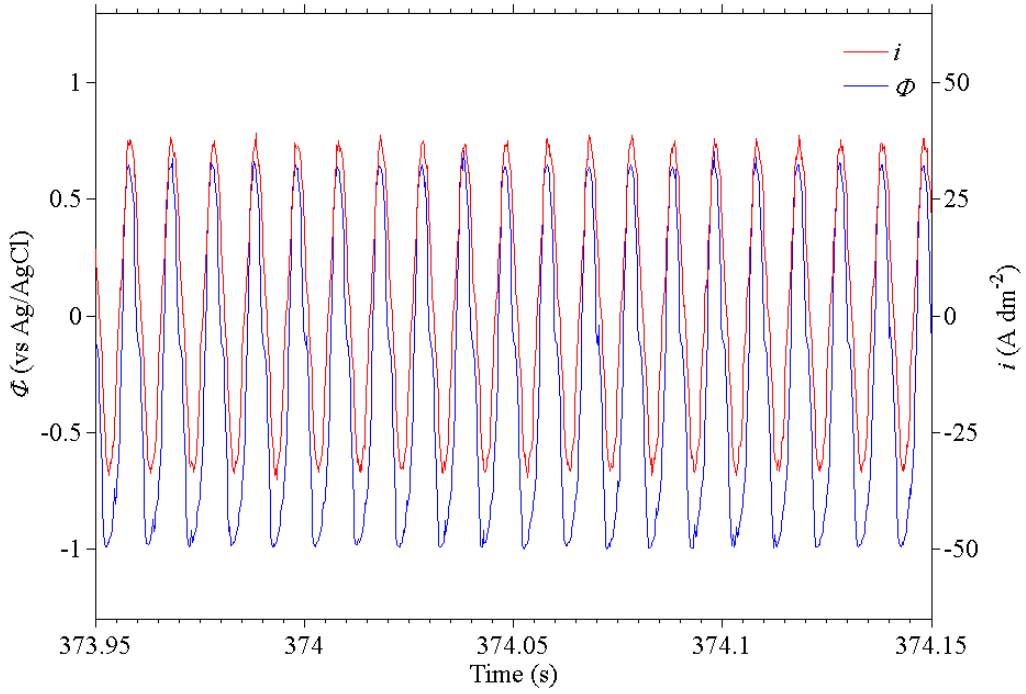

Figure 3.3 is a plot of the potential response and current density from the sample electrograined at 100 Hz.

The measured potential was recorded at 5 kHz from both the working and counter electrodes (*vs.* Ag/AgCl reference). The goal of these experiments was to correlate changes in the measured potential with changes in the gas release and retention; this assumes the presence of gas either at the reaction plane or in the smut (Equations 2.46 and 2.44, respectively). Following previous work, the temporal value of the maximum (anodic) and minimum (cathodic) potential response is attributed to faradaic reactions at the metal surface[37]. Thus, only the minimum and maximum points in each potential cycle, Φ_c and Φ_a, respectively, are needed.

Values of Φ_c and Φ_a were obtained from the potential response of each sample with knowledge of the frequency and the fact that the potential response is always in phase with the current (Figure 3.3). A simple routine was written that extracted the values of Φ_c and Φ_a

from the measured potential and shown in Figure 3.4. Using only the values of Φ_c and Φ_a, the temporal behaviour of the measured potential, from each sample, is compared in Chapter 5. Further, because Φ_c is considered faradaic, differences in its temporal behaviour can be attributed to differences in the gas pressure at the reaction plane or gas present in the smut; although, the DPPD additive is a known surface inhibitor and will increase the magnitude of V_c and is discussed in Chapter 5. Because gas permeation is much slower than the applied AC frequency, both Φ_a and Φ_c are presented in Chapter 5 and are referred to as the potential, Φ, for simplicity.

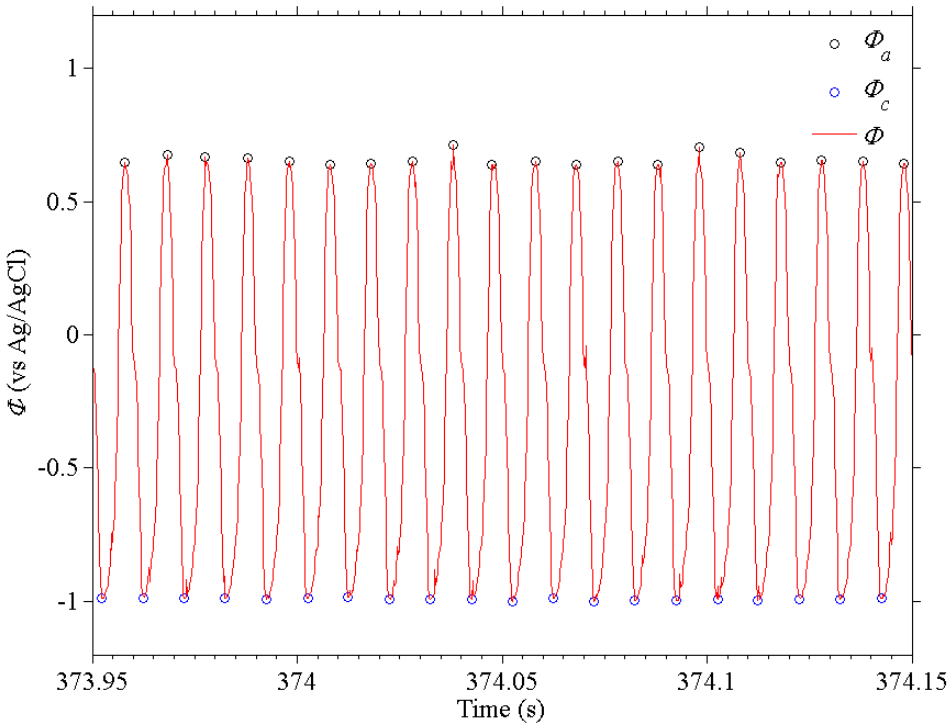

Figure 3.4 is a plot of the measured potential, Φ, and the minimum and maximum potentials, Φ_c and Φ_a, respectively. The plot was obtained from the sample at 100 Hz.

3.b.1.iv SEM imaging

Images from the final smut and pitted surface morphology were obtained for many samples as part of a collaboration with the Department of Materials and Chemistry at the Vrije Universiteit Brussel (VUB). Where SEM images are shown, the electrograining conditions associated with them will be included. The smut morphology was observed with a JEOL JSM-7000F field emission gun scanning electron microscope (SEM) upon deposition of 1.2 nm Pt/Pd layer applied by a Cressington 208 HR sputter coater equipped with a Cressington MTM-20 thickness controller, to avoid charging effects due to the non conductive smut surface. The final surface morphology was examined after removal of the smut by submersing the sample in either 20 g l^{-1} CrO_6 and 35 ml H_3PO_4 85% per l, at 90°C for 180 s or NaOH (6.5 g l^{-1}) for 5 s in 35 ^{o}C.

3.b.2 Artificial Pits

X-ray scattering and radiography experiments were performed on salt films formed in artificial pits. This section provides details of how the experiments were performed and how the data were obtained and converted to something useful for analysis. Results obtained from these experiments were converted to 1-D plots that are presented in Chapter 7.

Salt films were formed using an artificial pit shown in Figure 3.5. A 50 μm nickel foil (Aldrich) was embedded in epoxy (Araldite) and attached to the PVC tube with kapton tape. A Ag/AgCl reference electrode was placed into the top portion of the solution in the PVC along with a platinum wire as the counter electrode. Nickel foils were dissolved to pit depths of between 1 mm to 2 mm prior to collecting data, by using a slowly increasing potential. Once the desired pit depth is reached in the laboratory, the sample was placed in the beam where both steady state and time resolved formation experiments were performed.

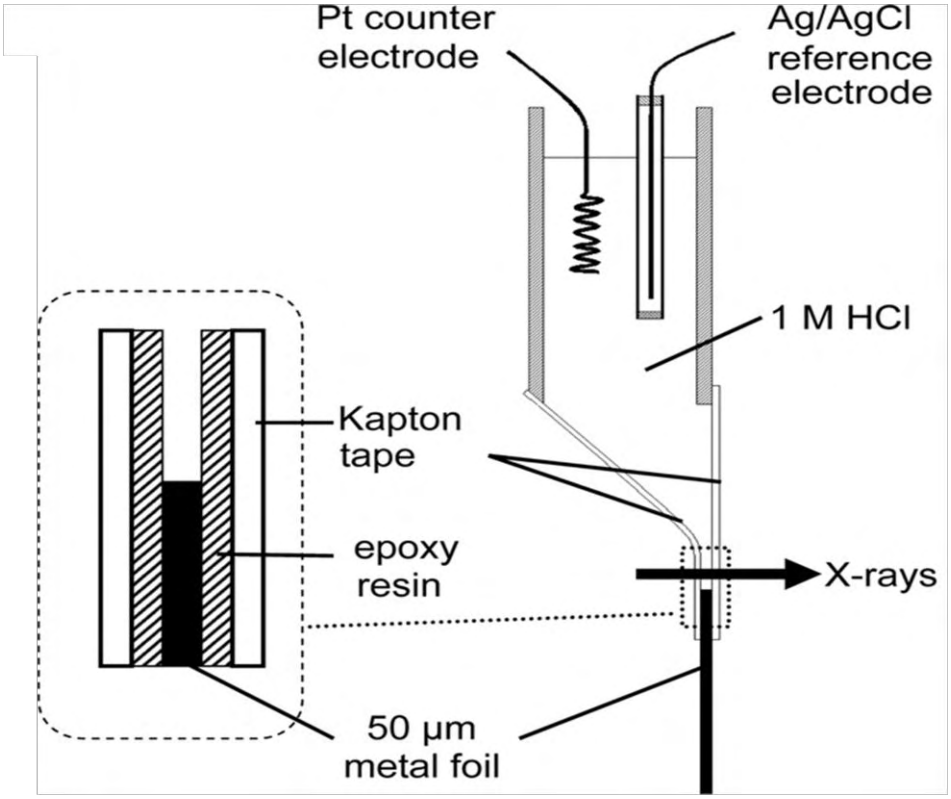

Figure 3.5 is a simplified schematic of the artificial pit cell used. In this cell, the X-rays pass through the interface and allow for diffraction from the salt. A cutaway view of the metal foil, as it is attached to the epoxy and kapton, is shown.

3.b.2.i Salt Film Formation

Salt films were formed by the application of a positive potential step that was chosen to be high enough to ensure salt film formation; applied potentials ranged from 0.4 V to 2.0 V. In this range of voltage step, the general dependence of the current versus time was found to always be the same. The cell voltage was held at 0 V (Ag/AgCl) for a period of five minutes prior to a potential step to ensure no salt film was present before collecting X-ray data. X-ray data was continuously collected before and after the potential step until the current reached a steady state value (~300 s). Exposure times ranged from 1 s to 300 s and are noted where appropriate. X-ray data was synchronized with the electrochemical data by recording the frame number and time throughout the experiment.

3.b.2.ii Time Resolved SAXS/XRD (I22)

Small Angle X-ray Scattering (SAXS) and X-ray Diffraction (XRD) experiments were performed at Diamond Light Source on Beamline I22 with a beamsize of 70 μm (v) by 320 μm (h) at an energy of 10 keV and a q range of 0.004 $Å^{-1} > q > 2\ Å^{-1}$. The XRD data was collected using a 1-D gas microstrip HOTWAXS detector simultaneously with a 2-D photon counting gas wire detector (SAXS), using the RAPID system. Ten second exposure times were used to obtain suitable 2-D SAXS, 1-D XRD patterns, which were calibrated using wet rat-tail collagen and NBS silicon, respectively. Electrochemical data was synchronized with the SAXS/WAXS data as mentioned previously.

The 2-D SAXS images were converted to 1-D using the Nika package available for Igor Pro[14]. During a typical potential step experiment, anisotropic scattering was observed between 10 s and 120 s after the potential step. Anisotropic scattering was converted to 1-D data of intensity (I) versus the scattering vector (q) by integration over a sector spanning from 85^o to 95^o and 265^o to 275^o. The range of integration was chosen such that the intensity profile across the azmuthal angle, ,φ, did not change significantly; The minimum FWHM of $I(\varphi)$ *vs.* φ within $0.05\ Å^{-1} \leq q \leq 0.1\ Å^{-1}$ in all four experiments was found to be *ca* 10^o.

3.b.2.iii Time Resolved XRD(MPW6.2)

X-ray diffraction data was collected at Daresbury SRS on Beamline MPW6.2 with a 300 μm(v) by 2.5 mm(h) beam size and an X-ray energy of 10 keV. The advantage of this beamline is that a much higher 2θ resolution was available, which allowed for a more in depth analysis of crystallite size and total volume with time. Diffraction patterns were obtained via a high speed 1-D curved multi-wire gas-filled detector, RAPID2, at collection times between 0.5 s and 300 s. Time resolved XRD data were obtained by summing 10-1 s

frames together to give a suitable diffraction pattern where a Voigt function could be fit to the strongest peaks. Steady state XRD data were collected over longer summations of between 800 s and 1200 s. During data collection, the sample was periodically moved up to keep part of the nickel foil in the beam by observing the transmitted intensity.

3.b.2.iv Time Resolved Radiography

Fast radiography experiments were performed at the Swiss Light Source (SLS) on the TOMCAT Beamline at 15 keV. The 2-D images were obtained using pixel size of 0.37 µm by 0.37 µm and an imaged area of 760 µm (h) by 260 µm (v). The raw images were synchronized with the electrochemical data by using the same method mentioned in Section *3.b.2.i*.

In order to calculate the transmission, T_r, from radiographs, the incident beam intensity profile was measured with the sample removed from the beam and dark field measurements were made at the start and finish of every sequence of measurements. An average intensity profile of transmission versus vertical distance from the electrode surface $T_r(x)$ was obtained by averaging of all vertical profiles in each image (Figure 3.6a). Errors in the resulting average are taken to be the minimum and maximum transmission encountered during the averaging. Because the interface is not perfectly horizontal, the vertical profiles were shifted to align them to a common reference point defined as the point of maximum derivative in each vertical transmission profile. This is a good reference point since the absorption of nickel metal is an order of magnitude greater than $NiCl_2(H_2O)_6$ salt (Figure 3.6b) and therefore the reference point will be located within the metal and hence unaffected by the presence or absence of a salt film.

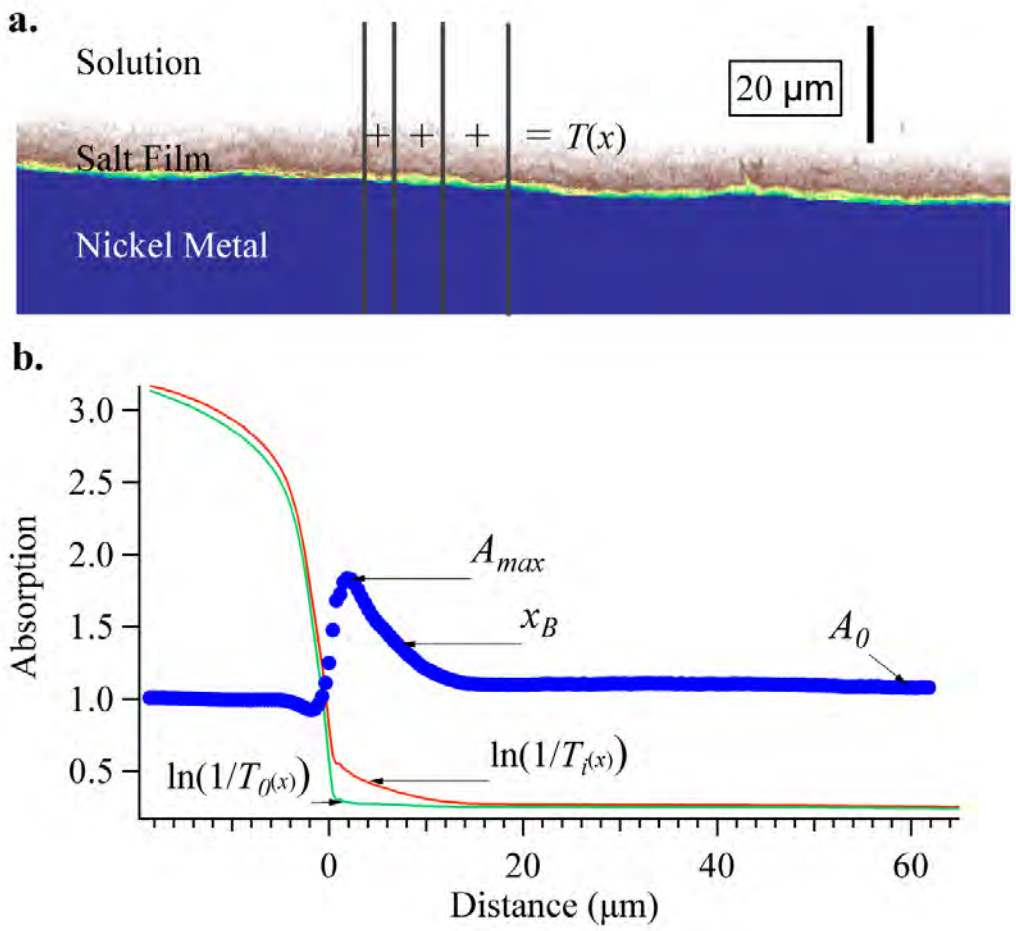

Figure 3.6 illustrates how the raw radiograph images were converted to 1-D data. Figure 3.6a is an example of a raw radiography image with vertical profile lines (gray lines) that contain the transmission as a function of distance. Figure 3.6b shows how the $A(x)$ profile is obtained for each frame and the single variables maximum absorption (A_{max}), salt film boundary (x_B) and Diffuse Region (A_0) used in the results and analysis.

Quantitative interpretation of the transmission profiles requires knowledge of the path length of X-rays in the solution. Unfortunately this is not known due to the necessary presence of a layer of epoxy resin of unknown thickness used during cell construction and because of the likelihood of some distortion of the kapton windows. To circumvent this uncertainty, profiles $A(x)$ were derived that are proportional to the supersaturation of the solution as well as any salt by the Beer-Lambert Law.

The absorption profile of frame i, $A_i(x)$, is defined by the equation (Figure 3.6b):

$$A_i(x) = \frac{\ln\left(T_{r_i}(x)\right)}{\ln\left(T_{r_o}(x)\right)} \quad (3.3)$$

where T_{r_i} is the averaged transmission profile at frame *i*, and T_{r_o} is the averaged transmission profile taken during a period when the potential $\Phi = 0$ (Figure 3.6b) after a sufficient time had elapsed to ensure that all salt crystals had dissolved and to allow the concentration profile to level out in the 50 μm region of interest in this study. For a 1.5 mm deep pit and a step from 1.6 V to 0 V the profiles collected between 50 s and 150 s provide a suitable reference. It can be shown that the concentration of Ni(II)Cl does not change by more than 0.3 M between 50 s and 150 s for all data presented here. Errors arising from minor changes in $A(x)$ during this period and errors in the averaging are combined appropriately and will be applied to the final results shown in Chapter 7. The value of A represents contributions from concentrations of Ni(II) and Cl species above saturation as well as any salt present i.e. $NiCl_2(H_2O)_6$[38].

The $A(x)$ profile in Figure 3.6b can be described by A_{max}, the maximum absorption, A_0 the base level absorption far from the interface and x_B, the salt film boundary, respectively. At steady state, A_0 is taken as the constant excess absorption far from the interface and is not considered to have an appreciable salt fraction. The salt film boundary x_B is arbitrarily defined as the position having absorption of 0.2 above the base level A_0. Changes in A_{max} and x_B during a potential step experiment are reported here.

CHAPTER 4
AC Electrograining: Literature Review

AC Electrograining is a process by which a roughened surface is produced on aluminium for applications in high quality lithographic printing and for energy storage super-capacitors. A fundamental understanding is paramount to improve the electrograining process, which produces an estimated 800,000,000 m^2 per year of specified roughened aluminium. Upon electrograining an aluminium surface, the effective surface area of the aluminium is increased by the presence of convoluted pits on the surface. The focus of this study is to understand the effect that the inherent smut (formed during electrograining) has on the final surface morphology. A complete understanding of the effect of smut on final surface morphology, together with previous work, will provide the understanding necessary to tailor the final surface morphology to a specific application.

4.a. Electrograining Mechanism

Electrograining is typically accomplished by imposing an AC current waveform[35], on the aluminium electrodes, with either HNO_3 or HCl as the electrolyte[39-41]. In general, electrograining can be described by dissolution during a positive (anodic) cycle, where aluminium is dissolved, and forming sub-micron pits at the surface. During the cathodic cycle, hydrogen evolution occurs at the surface, which increases the pH causing additional cathodically dissolved aluminate ions to form leading to precipitation of the amorphous $Al(OH)_3$ smut layer.[34, 35]

4.a.1 Dissolution

The main difference between the two electrolytes is the dissolution of the aluminium during the anodic cycle. In HCl solution, oxidation of the aluminium occurs during the anodic cycle by the equations:

(4.1) $Al+3Cl^- \rightarrow Al(Cl)_3+3e^-$

(4.2) $Al(Cl)_3 \rightarrow Al^{3+}+3Cl^-$

where Reaction 4.1 is the rate limiting reaction.[29] The resulting morphology, characteristic of graining in HCl, is the presence of fine crystallographic, cubic pits[42, 43].

Conversely, anodic dissolution in HNO_3 occurs by a mechanism whereby individual "cups" of the aluminium are anodized at the beginning of the anodic cycle.[39] As the anodic current increases, thermal breakdown of the oxide layer causes the underlying aluminium to be exposed and attacked, removing the anodic oxide.[39] Removal of the cup-shaped aluminium

oxide results in hemispherical primary pits formed in HNO_3, which are different from the cubic-shaped pits formed in HCl[40].

4.a.2 Repassivation

As the current is reversed to the cathodic half-cycle, local H_2 evolution causes a rapid increase in the pH local to the newly formed pit by the reaction:

(4.3) $$H^+ + e^- \rightarrow {}^1/_2\, H_2$$

As the pH increases, dissolved Al(III) is expected to precipitate at pH 5, where aluminium hydroxide solubility is minimum[44]. However, it has been shown through comparison of total smut formed and total anodic charge passed that more smut is formed than is theoretically possible at 100 Hz and below.[34] These experimental results were explained by considering the occurrence of cathodic corrosion at pH values > 5[34, 45], by the reaction:

(4.4) $$Al + 4H_2O + e^- \rightarrow 2H_2 + Al(OH)_4^-$$

Thus, dissolved Al(III), from anodic dissolution and Reaction 4.4, both precipitate as amorphous $Al(OH)_3$ when the near interface pH drops below 5 as the current returns to the anodic cycle.[34]. This $Al(OH)_3$ smut has been shown to be an amorphous gel-like surface layer, containing a dilute (<5%) population of fine $Al(OH)_3$ particles and some metallic Al particles on the order of 1 μm.[34, 40, 41] This so-called "smut" is firmly attached to the surface after electrograining and must be removed by chemical means[34].

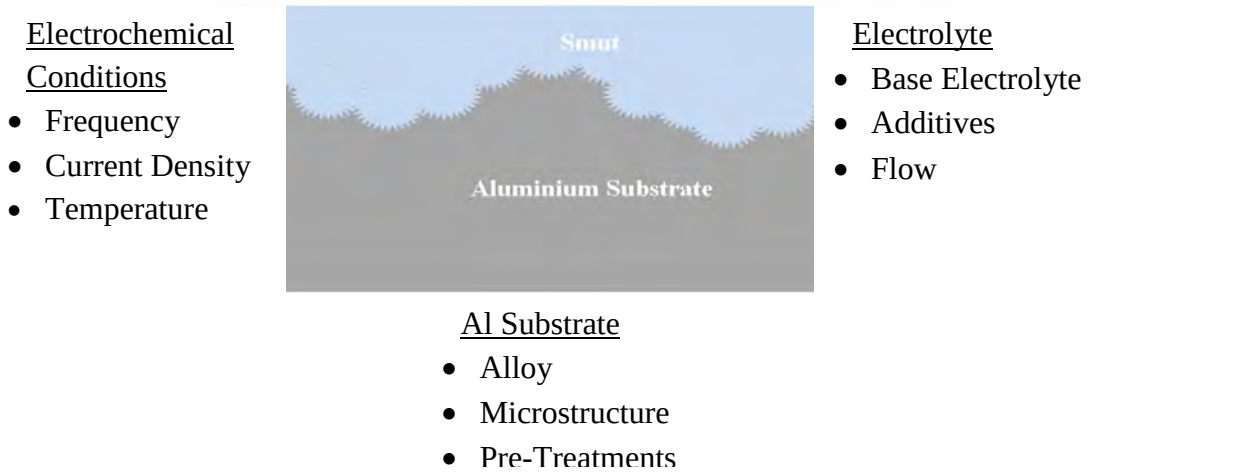

Figure 4.1 is a schematic illustration showing the factors that affect the final surface morphology after electrograining at different conditions.

4.b. Manipulation of Surface Morphology

To tailor the roughened surface to the specific application, factors that affect the final surface morphology have been studied and summarized in Figure 4.1. Traditionally, changes in the aluminium substrate, electrochemical conditions and electrolyte have been directly correlated with some specific changes in the final surface morphology. The focus of the current research is the influence of the smut on the final surface morphology. Because some factors in Figure 4.1 affect the smut and final surface morphology, their influence on the final surface morphology is discussed in each of the following sub-sections. In general, the final surface morphology can be characterized by the presence of hemispherical pits of varying size and depth, which contain smaller primary pits inside them[40] and shown schematically in Figure 4.1.

4.b.1 Substrate

In general, the state of the substrate affects the surface activation and thus where pits can form in either HCl or HNO_3.[46-48] Pit initiation and nucleation have been shown to occur at metallurgical, mechanical or compositional flaws in the alumina layer[47, 49]. However, the presence of the inherent rolled-in oxide and inter-metallic particles causes the presence of

large ungrained "plateaus," even at longer graining times in both electrolytes[48]; although a two-step pre-treatment reduces the effect of both.[48] Also, the presence of manganese in the aluminium substrate results in a change in the surface morphology in both electrolytes, with an immediate effect on pit initiation in HNO_3[46]; in HCl, the presence of manganese affects only the growth of hemispherical pits.[46] Recent *in-situ* experiments have shown that intermetallic particles cause an initial increase the measured potential.[37] Continued electrograining results in degradation of the oxide layer, resulting in a temporary decrease in the measured potential within the first second.[37] Thus, the presence of oxide layers, inter-metallic particles and manganese changes the surface activation and cause non-uniformity in the final surface morphology; although most substrate effects diminish with longer graining times.[48]

4.b.2 Electrochemical Conditions

Electrochemical conditions include the current density, frequency and temperature. Typically, either an alternating sinusoidal voltage or current is used, with the latter being more common. Differences between the two are minimal and are not discussed here. The size of the primary pits in both HCl and HNO_3 has been shown, experimentally, to depend on electrochemical parameters.[40, 42, 43, 50, 51] Theoretical calculations, taking into account the number density of active sites, current density, frequency and the anodic current efficiency, show that the primary pit sizes follow the expected trend with respect to the charge passed in each cycle[43]; though, experimentally observed pit sizes are always smaller than predicted owing to uncertainty in the number of active sites and the anodic efficiency.[43]

Although the primary pit sizes depend on the frequency and current density, the overall surface morphology is also characterized by larger features on the micron scale. The overall

surface morphology has been characterized by having one of three possible morphologies shown in Figure 4.2:

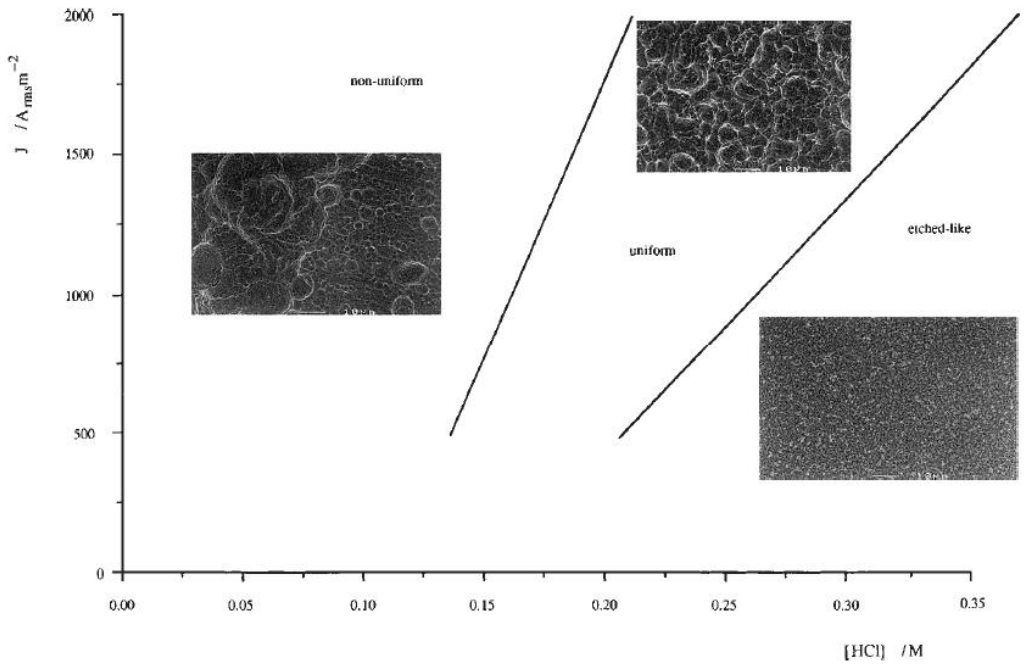

Figure 4.2 is a plot showing the general types of surface morphologies obtained after electrograining under different conditions. Although, only the current density and electrolyte concentration are varied, the general features for each morphology describe what is observed when changing other parameters. Image is taken from Laevers et al.[29]

non-uniform pit morphology, uniform pit morphology and an etched-like morphology, depending on the electrolyte concentration, current density and electrolyte flow.[29] At high electrolyte concentrations and low current densities an "etched-like" morphology is obtained and is characterized as a uniform surface with small primary pits and little to no micron-sized pits.[29] With increasing current density and decreasing concentration, the surface morphology moves to a uniform pit morphology[29] where hemispherical pits are observed,[29, 43, 51] with their size depending on the frequency[40, 43]. At the lowest concentrations and highest current densities, a non-uniform pit morphology is obtained,[29] as hemispherical pits grow laterally until they intersect[29, 51]. As the electrolyte flow is increased across the electrodes, the surface morphology will tend towards an etched-like morphology, with no hemispherical pits. Altough no mechanism behind overall surface morphology has been

proposed, samples having a uniformly pitted surface were associated with higher surface overpotentials immediately after electrograining.[29]

4.b.3 Electrolyte

Primary pits in HNO_3 are hemispherical[40, 41] and larger[41] than in HCl (at frequencies greater than 1 Hz), owing to the different dissolution mechanisms. In general, the overall surface morphology is similar, with hemispherical pits that are composed of the respective primary pits.[40, 41] Although, under certain conditions, electrograining in HNO_3 results in a more convoluted surface, compared to HCl where both deep pits and relatively flat areas are observed.[41]

Recently, the addition of citric acid, acetic acid and disodium phenyl phosphate dehydrate (DPPD) to the HCl electrolyte have also shown to change the surface morphology significantly.[36] The addition of acetic acid results in a final surface morphology with fewer plateaus and larger pits having finer features, due to enhanced pit consolidation.[36] Similar to HCl only, the addition of citric acid results in hemispherical pits of similar size but are shallower.[36] Finally, the addition of DPPD results in large plateau areas in between very deep pits and was analogous to samples electrograined in HCl with a cathodic bias.[36] Differences in resulting surface morphologies with these additives was correlated with differences in the smut morphology.[36]

4.c. Manipulation of Smut

Both the amount of smut and its corresponding morphology can be manipulated, just as the final surface morphology. The temperature of the electrolyte does not significantly change the amount of smut formed between 15 ^{o}C and 50 ^{o}C[43] and is not discussed further. The amount of smut is typically characterized by its total mass[34] and thickness, with the latter being more ambiguous because it is obtained after the smut is dried. Porosity[36] and

uniformity[40, 52] are normally used to characterize the smut, with the latter referring to large changes in the dried thickness across the aluminium surface.

4.c.1 Electrochemical Conditions

Of all the electrochemical conditions that can be manipulated, the frequency has been shown to have the largest effect. It has been shown that the amount of smut and smut morphology does change with frequency[34]. When the frequency is increased from 1Hz to 100Hz, the total mass of smut formed decreases[34] and the total aluminium weight loss increases[34, 50]. Although other electrochemical parameters can be varied, their effect on the smut is not as significant as the frequency.

4.c.2 Electrolyte

Regardless of the electrolyte, smut inherently forms on the surface and its morphology is very different between HNO_3 and HCl. In general, smut formed in HCl can be described as a uniform "mud-like" layer on the surface.[34] On the other hand smut formed in HNO_3 is very non-uniform with the presence of smut around the rim of deep pits. The addition of acetic acid results in a uniform smut layer that contains very small pores, while the addition of citric acid results in larger pores.[36] Finally, the addition of DPPD drastically changes the final smut morphology, as the smut is very non-uniform with the presence of large, isolated deposits.[36]

4.d $Al(OH)_3$ Gels

Previous work has concluded that $Al(OH)_3$ particles are precipitated by changes in pH during the current cycle.[34] Structure and speciation of precipitated $Al(OH)_3$ in solution have been extensively studied with NMR and SAXS.[15, 53-57] Speciation and aggregation within the solution has been a topic of much interest and depends on the amount of $[OH]^{-1}$ added.[15, 53-55, 57] It has been shown that at moderate pH values, Al_{13}[58] as well as other dinuclear[55] and

oligomer species[59] exist along with the hydrated monomer [55]. Later studies showed that fresh gels were composed of aggregated Al_{13}, followed by pseudo-boehmite and a hydroxide phase upon aging.[60] Recent ^{27}Al NMR studies showed that smut formed in HCl only is comprised mostly of the hydroxide phase, with some peak broadening which was attributed to the presence of a low-level oxide (e.g. $Al(OH)_{2.5}$).[36] Because of variations in the speciation and large species, such as Al_{13}, in $Al(OH)_3$ gels, it is likely that electron density fluctuations on the same order as their size exist in their parent aggregates; this will become important in the SAXS analysis.

The shape and structure of aluminium hydroxide particles within precipitated gels has generally been modelled as oblate spheroids (platelets)[54] or polydisperse spheres[61, 62] that are made up of individual (solid) aggregated $Al(OH)_3$ molecules. It has also been shown by SAXS measurements that these aggregate particles do agglomerate inside the gel.[54, 62] Thus, the general features of $Al(OH)_3$ particles inside gels are that they are aggregate particles, which can be comprised of different $Al(OH)_3$ species. Further, these aggregates tend to form agglomerates.

4.e. Motivation for Current Research

Most studies of smut have been carried out on dehydrated materials using vacuum-based techniques such as electron microscopy, AES, XPS, and SIMS depth profiling.[34-36, 39, 41, 51, 63] Using these data to understand the role of smut structure during electrograining requires an assumption that the gel, which contains about 90% water by mass when formed, is unaltered by dehydration.[34] In the absence of firm evidence, this is hard to defend. Small angle X-ray scattering (SAXS) is well suited for characterisation of amorphous and porous materials[10, 54, 55, 57, 62, 64] and is used as the primary technique for these *in-situ* studies.

In order to understand the role that the structure of the smut plays in the electrograining process, different electrochemical conditions and electrolyte solutions were chosen in which the dried smut morphology and final pit morphology are very different.[36, 41, 63, 65] In each round of experiments, samples electrograined at 50 Hz in HCl is used as the reference. Results obtained are compared to electrochemical and electrolyte trends reported previously, with respect to the final surface morphology.

CHAPTER 5
AC Electrograining Study

This chapter describes an experimental study of AC electrograining of aluminium. The results and analysis, discussion and conclusions are presented in three successive sections. In the first section, *ex-situ* and *in-situ* SAXS/USAXS data are analysed, which focus on identifying the scattering population from data obtained from *in-situ* SAXS experiments. Following the identification of the scattering population as being from $Al(OH)_3$ particles, the size and structure of the particles are discussed. The second section will focus on the total scattering analysis of the first and second experiments, which lead to the identification of gas in the smut[33]. In the final section, the *in-situ* results from electrochemical/SAXS experiments are presented and analysed, followed by the final discussion and conclusions.

5.a. Scattering from $Al(OH)_3$ particles

Following Equations 2.11 and 2.12, in Chapter 2, small angle X-ray scattering is only observed for particles on the nanometre scale, where the size of the particle is on the order of $2\pi/q$.[3] In addition, there must be a difference in electron density between the particle or pore and the surrounding matrix.[3] Before the *in-situ* SAXS data, obtained from the smut, can be properly analysed, all possible populations that meet the above requirements must be considered. No anisotropy was observed and isotropic scattering theory is applied in this chapter.

5.a.1 Scattering from Surface Pits

As stated in the Experimental section, an ungrained Al foil was used as a background (for the *in-situ* data) to remove scattering contributions from metal foil. However, the most appropriate background would actually be the grained Al foil, with the smut removed, because primary pits formed on the surface are less than a micron[43, 51] and have an electron density (Al metal) different from the electrolyte or air that occupies the pit; although smut removal is possible, it was not feasible to achieve this immediately after the *in-situ* SAXS experiments. Therefore, scattering from the pitted surface must be measured before it can be assumed the *in-situ* scattering obtained is from the smut alone.

To obtain the scattering from pits, ultra-small X-ray scattering (USAXS) *ex-situ* experiments were performed on foils electrograined at 3 different conditions, varying the frequency at: 1 Hz, 50 Hz and 100 Hz, all at 20 A_{rms} dm^{-2}. These experiments serve to provide a reference for characteristic scattering from the pitted surface so that pit scattering can be accounted for in the *in-situ* data.

A typical electrograined surface is characterized as micron sized hemispherical pits that contain many small, cubic pits.[35] The resulting small angle scattering pattern from the hemispherical pits must therefore follow (from low to high q) a Guinier knee associated with the larger hemispherical pits followed by a decay in q between q^{-1} and q^{-3}, characteristic of mass fractal-like scattering[9]; the latter is a consequence of the nature of the convoluted pits that make up the hemispherical pit. Also, because the primary pits are in close proximity to each other, there must be some interference between them. Because the size of these primary pits and distance between them are on the nanometre scale[35, 43, 51], the mass fractal decay in q will terminate when the size of the pits (or space between them), corresponds to the Guinier approximation (Equation 2.21). Following this Guinier knee there will be a Porod decay proportional to q^{-4} arising from the well defined surface of the pits. Finally, a constant background is expected at high q, as the scattering is isotropic with respect to the incoming X-rays.

Figure 5.1 shows a plot of the USAXS data measured on *ex-situ* samples, electrograined at three different frequencies, from which smut has been removed. Characteristic to all curves are Porod decays in intensity proportional to q^{-4} at $q > 0.003$ Å^{-1}. Preceding these power law regions are Guinier regions that are related to either the pit sizes or the distance between them. Given the q range available for the *in-situ* SAXS data discussed later (0.006 Å$^{-1} \leq q \leq 0.15$ Å^{-1}), a Porod decay will be observed at $q > 0.003$ Å^{-1} if scattering from the pitted surface dominates over scattering from the smut.

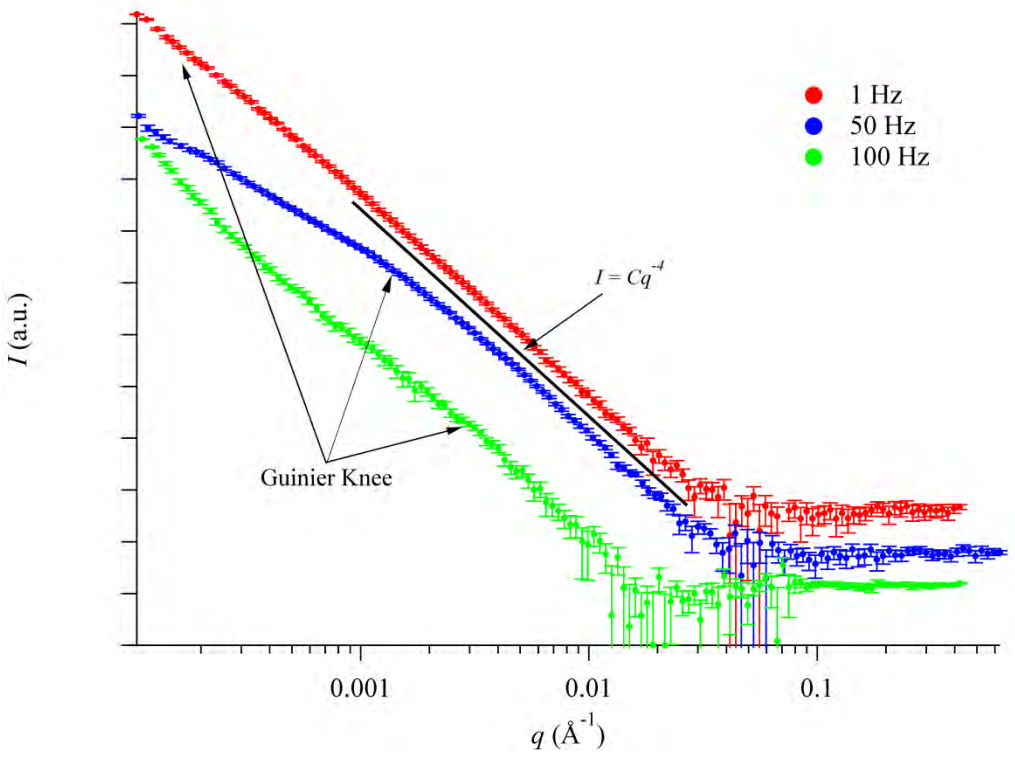

Figure 5.1 is a plot of *I*(*q*) of the USAXS data obtained from the pitted surface of samples electrograining at three different frequencies. The plot shows that characteristic pit scattering results in a Porod decay in *q* at *q* values greater than 0.003 Å^{-1}, which is not observed in *I*(*q*) curves obtained from the smut.

Modelling the USAXS data in Figure 5.1 is non-trivial owing to the close proximity of the primary pits. However, a simplified model can be obtained by assuming: the pit sizes have a narrow size distribution, associated with the charge passed in the anodic half cycle[43], and assuming the space between the pits is random and very polydisperse, which will result in a negligible contribution to the scattered intensity. Assuming the scattering curve is dominated by scattering from the primary pits, their associated Guinier knee would be found at lower *q* with decreasing frequency as larger pits are formed[43]. This phenomenon is directly observed in Figure 5.1 and confirms that the USAXS data are able to resolve the primary pit dimensions.

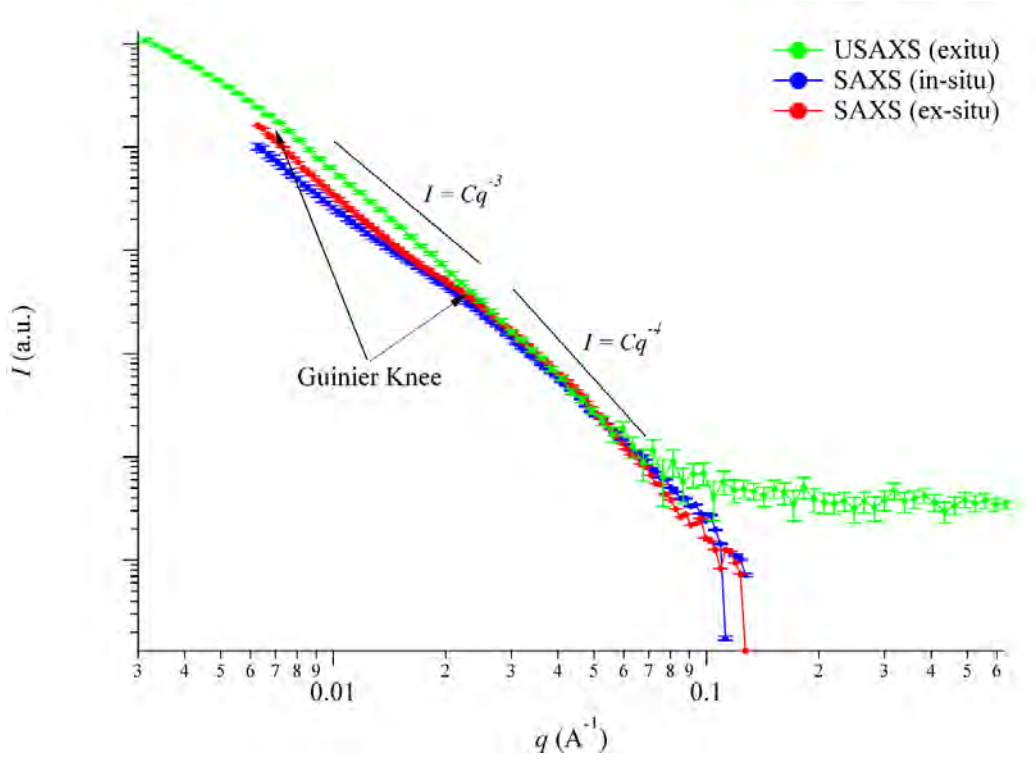

Figure 5.2 is a log-log plot of *ex-situ* USAXS (green) data obtained from the smut, *ex-situ* SAXS data obtained from scraped powder (red) and *in-situ* SAXS data (blue) obtained after 80 s of electrograining.

5.a.2 *In-situ*/*Ex-situ* results in HCl

To confirm that *in-situ* small angle scattering is dominated by scattering from the smut, smut was mechanically scraped from a grained sample. The resulting SAXS curve was obtained for comparison to the *in-situ* SAXS curve and *ex-situ* USAXS data obtained from the smut. Figure 5.2 shows a plot of all three data sets for comparison. Clearly, no Porod decay can be observed at q>0.003 Å^{-1} in any of the data, which confirms that scattering from the pitted surface is not present in the *in-situ* data. Because the pitted surface scattering has been subtracted from the USAXS data it is also observed that the smut has no characteristic features similar to the pitted surface, which further allows for characteristic scattering from the smut and pits to be separated. Similarities between the USAXS and *in-situ* SAXS data (Figure 5.2) lead to the conclusion that scattering from the smut, obtained in the *in-situ*, dominates over the pit scattering.

Small angle scattering from the smut (*in-situ* and *ex-situ*) can be characterized by a Guinier knee at q~0.006 Å, followed by a power-law decay in q approaching q^{-3}, which terminates at another Guinier knee at q~0.025 Å. Following the high Guinier knee, is a power-law decay slightly less than a typical Porod decay of q^{-4}. Each of the previously mentioned regions of the scattering curve gives information about the scattering population(s) in the smut.

Based on previous work, the smut is a gel that contains 5% $Al(OH)_3$, 5% Al and 90% water.[34] Previous SEM imaging has reported the presence of large Al metallic particles in the smut, which are likely due to undercutting and detachment of grains.[34, 66] Detached Al metal grains were reported to be on the micron scale and were thought to also cause the dark appearance of smut formed under certain conditions[34]. Given the size of these Al metal particles, a clear Porod decay would be observed in Figure 5.2 in the low q region. Although, these particles may be present in the smut, their scattered intensity is not observed and is likely due to their large size or proportionally small number. Thus, the two remaining possible scattering populations are either pores or $Al(OH)_3$ particles.

5.a.3 Time Dependent Scattering

To better understand the nature of the scattering population, changes in the *in-situ* SAXS data under different conditions were studied. Two characteristic times are considered from the experiments described in Chapter 3. The electrograining time is the total time that electrograining was applied and the quiescent time is the total time after a ten second electrograining burst. As the total electrograining time increases, more smut is formed, with most smut formed in the first 50 s.[34] With the formation of more smut, any changes in the SAXS data will reflect how the scattering population changes in either number or size and shape. During the quiescent period, following electrograining, the pH slowly returns to the

bulk pH and smut begins to dissolve[67]; SEM imaging performed at the VUB revealed that observable smut dissolution occurred at 90 s and most smut was removed after 800 s. Other factors such as gas release could also influence the scattering shape, but will be discussed in Section 5.b.3.

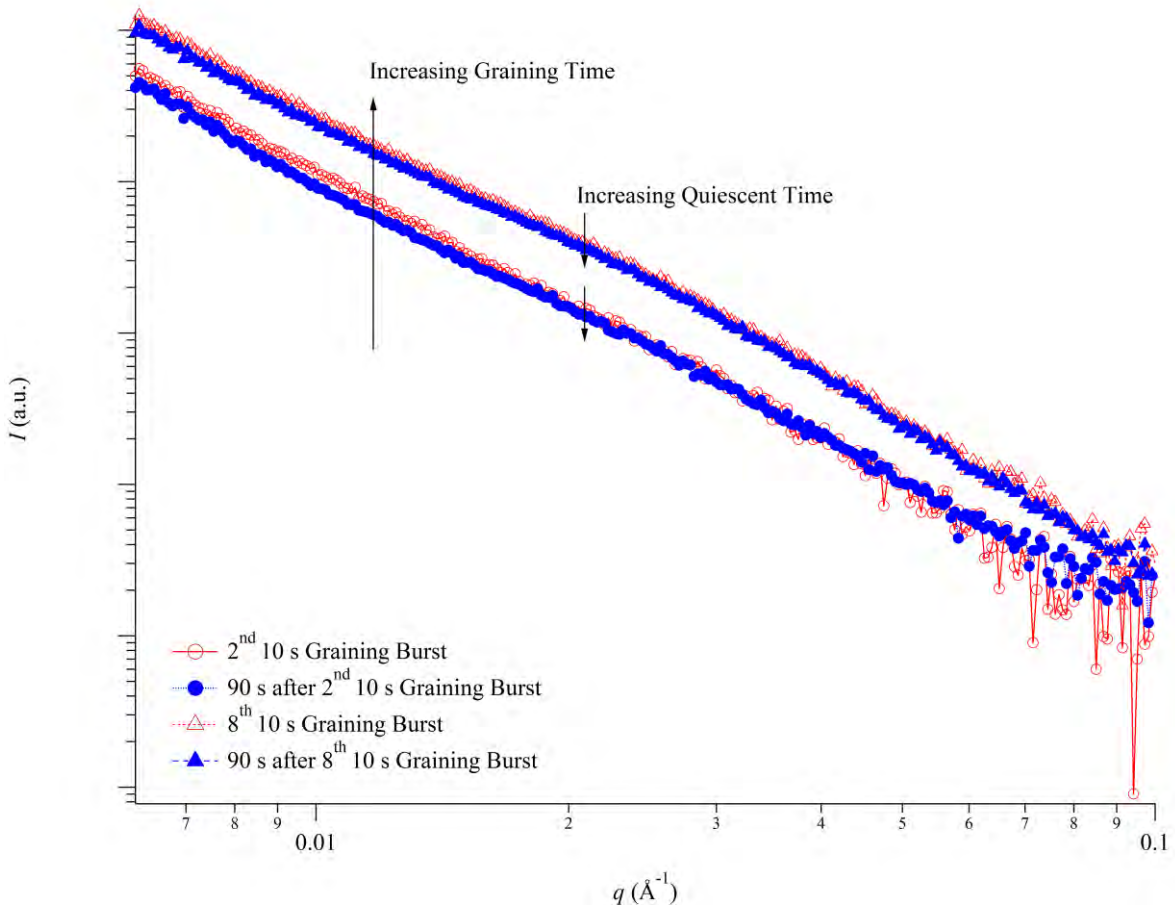

Figure 5.3 is a log-log plot of the *in-situ* scattering obtained during (red) and 90 s after (blue) electrograining for the 2nd and 8th electrograining burst.

Figure 5.3 shows the SAXS data obtained during and 90 s after the 2nd and 8th electrograining bursts. During and after the 2nd electrograining burst the scattering shape changes only at low *q*. By the 8th electrograining burst there is little change in shape in either during or after electrograining. Only changes in the intensity scaling are observed. Because the general

features, characteristic of smut scattering (Figure 5.2), are always observed in the higher q region, it is concluded that the size, shape and possible structure of the smaller scattering population remain constant through the experimental electrograining sequence.

Therefore, to account for changes in the scattered intensity at lower q, the presence of additional scattering populations, at low q, are considered. Because this population scatters only at low q, it is assumed that only Porod scattering is present from large particles, which decays rapidly at high q. The scattered intensity from separate populations is modelled by simple addition, by the general equation:

(5.1) $$I(q) = \sum I_i(q)$$

where $I_i(q)$ is the scattered intensity from each individual population. The limited q-range makes it difficult to characterize the changes in the scattering shape, at low q, during and after the 2nd electrograining burst. Because the general features, at higher q, remain unchanged during and after the burst, it can be assumed an additional population exists during the 2nd electrograining burst. Assuming this population is very large and meets the Porod conditions (Chapter 2), the resulting scattered intensity, $I(q)$ after the 2nd burst would follow the equation:

(5.2) $$I(q) = Bq^{-4} + I_{smut}(q)$$

where the first term accounts for Porod scattering from a population of large scatterers and $I_{smut}(q)$ would be the same as at 90 s after the burst. It can be shown that with the correct value of B, the scattered intensity, $I_{smut}(q)$, during and after the 2nd graining burst are almost identical; although, the value of B obtained is meaningless without knowing anything else about this large population. Even though the shape of the scattered intensity changes only at

low *q* in some data (particularly early in the electrograining experiment), the main scattering population is considered to be unchanged with time. Thus, the scattering population within the smut does not change significantly with respect to their size, shape or possible structuring.

Experimental SAXS results from all samples also show that the scaled intensity increases with electrograining time as shown in Figure 5.3. No change in the shape or size of the high-*q* scattering population is observed by the lack of a change in the Guinier region with quiescent time or electrograining time. Thus, the scattered intensity would scale according to either the total number of scattering particles or pores or the contrast by Equation 2.18.

An increase in the scaled intensity with electrograining is consistent with the formation of more smut, which would result in an increase in the number of particles or pores in the smut[34]. On the other hand, a decrease in the scaling during the quiescent period can be due to either a decrease in the total number of particles/pores, due to smut dissolution[67] or the contrast.

5.a.4 Discussion

Results from *ex-situ* USAXS experiments of a pitted surface, with and without smut, led to the conclusion that small angle scattering from the smut gives a specific $I(q)$ curve very different from the pitted surface (Figure 5.1 and Figure 5.2). This signature $I(q)$ curve was also obtained in *ex-situ* smut mechanically scraped from a sample and from *in-situ* data, which led to the conclusion that SAXS data obtained *in-situ* is associated with the smut. Considering all known populations that could give a SAXS signal, it was concluded that SAXS data obtained *in-situ* can be associated with either particles or pores.

5.a.3.i Porous Scattering

The presence of pores in the smut would give a SAXS signal, by the Babinet principle of reciprocity discussed in Chapter 2. The Guinier region in Figure 5.2 corresponds to scattering sizes on the order of 10 nm, which would correspond to nano-porosity that exists in the smut gel. These pores could be formed by the necessary hydrogen evolution that occurs during the cathodic cycle[34], resulting in nano-bubbles suspended in the smut; of course, most of this gas must move through the smut to the electrolyte[68]. Assuming that the scattering is from nano-porosity requires that this porosity is unaltered by dehydration, as the same scattering shape is observed in both the dried powder and wet smut (Figure 5.2). Because the smut has been shown to be a gel of ca 90% water, these pores are likely surrounded by water. As the water is removed from the smut, the size distribution of pores is expected to change and is not observed, especially after the smut is mechanically scraped from the surface (Figure 5.2). In addition, the pores would need to maintain their size and shape during each subsequent electrograining burst, where gas flows rapidly through the smut[68]. Thus, SAXS data obtained from the smut is not considered to be from pores inside the smut and must therefore be associated with the $Al(OH)_3$ particles because the size and shape of the scattering population does not change throughout the experiment.

On the other hand, gas must be present in the smut during electrograining and could result in a SAXS signal because of the difference in electron density between gas and water. Changes in the shape of the $I(q)$ curve during early bursts were accounted for by the presence of a larger scattering population. The source of this larger population can be attributed to gas, as these pores would fill with electrolyte after the electrograining burst causing the low-q SAXS signal to disappear (Figure 5.3). Although gas containing pores are possibly observed *in-situ*, their sizes are too large to be observed in the available q range.

5.a.3.ii Modelling

The presence of two Guinier regions in Figure 5.2 must be associated with: anisotropic particles, two separate populations or structured particles such as agglomerates[6]. Because the intensity decay, between the Guinier knees, is always greater than q^{-2}, scattering from anisotropic particles is not considered. To differentiate between the agglomerate scattering and two separate populations, the nature of the $Al(OH)_3$ particles must be considered.

The tendency of precipitated $Al(OH)_3$ particles to agglomerate in gels formed by pH precipitation[15, 57] requires the SAXS data to be treated as an agglomerate system. Because of the similarities between the *ex-situ* USAXS and *in-situ* SAXS, the USAXS data was used in the initial model fit, owing to the larger available *q*-range. A two level Unified equation is well suited to model an agglomerated system[7] and is given by the equation:

(5.3)

$$I(q) = G_2 e^{\frac{-q^2 R_{g_2}^2}{3}} + B_2 e^{\frac{-q^2 R_{g_1}^2}{3}} \left(\frac{\left(erf\left(\frac{qR_{g_2}}{\sqrt{6}}\right)\right)^3}{q} \right)^{P_2} + G_1 e^{\frac{-q^2 R_{g_1}^2}{3}} + B_1 \left(\frac{\left(erf\left(\frac{qR_{g_1}}{\sqrt{6}}\right)\right)^3}{q} \right)^4 + B_{ckg}$$

where R_g, G, B and P are defined in Chapter 2 and whose subscripts 1 or 2 are associated with scattering from the primary $Al(OH)_3$ particles and their agglomerates, respectively; the parameter R_{CO} serves to terminate the power-law scattering from the previous level[7]. Because the scattering is isotropic, a constant background, B_{ckg}, was used. A power-law decay of q^{-4} is also assumed for the primary particles. Equation 5.3 was fit, by least squares, to the USAXS data in Figure 5.2 using the Irena package available for Igor Pro[14].

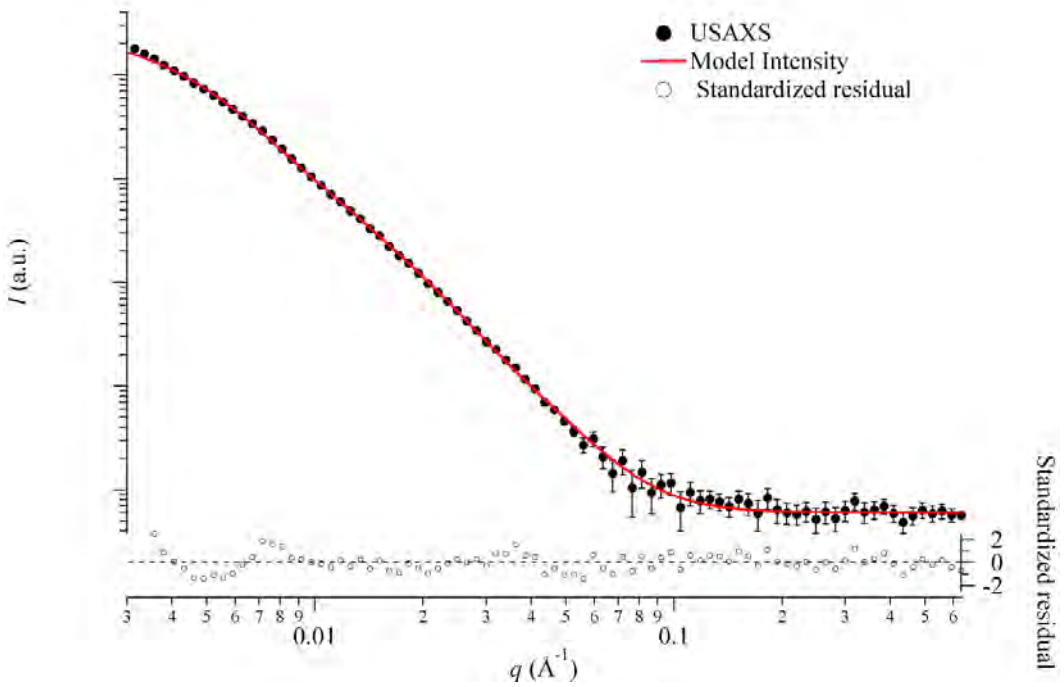

Figure 5.4 is a log-log plot of the USAXS data with the model fit of Equation 5.3 by least squares (red line). The standardised residual is shown at the bottom to be sufficiently random for most of the *q*-range fit.

Figure 5.4 shows that the model fits well within experimental error, as taken from the randomness of the standardized residual at $q>0.01$ Å^{-1}. Oscillations of the standardized residual, at $q<0.01$ Å^{-1}, can be explained by polydispersity effects in the parent agglomerates that Equation 5.3 cannot completely account for. Results from the fit are shown in Table 1.

Table 1 is the results obtained from fitting Equation 5.3 to the USAXS data.

	1st Level	2nd Level
G (a.u.)	$1.2\times10^{4}\pm0.9\times10^{4}$	$3.2\times10^{6}\pm0.1\times10^{6}$
R_g (Å)	90±16	444±7
B (a.u)	$3.0\times10^{-3}\pm0.3\times10^{-3}$	0.30[1]
P	4	2.79±0.03

[1] Calculated from G_2, P_2 and R_{g2}. [69] G. Beaucage, *Physical Review E* **2004**, *70*.

The value of R_{g1} obtained from the fit is slightly larger than 5 nm obtained from Na_2CO_3 precipitation of 0.93 M aluminium nitrate salts[57] and smaller particles of 2.5 nm[54] and 5 nm[15] thick disks formed from lower aluminium salt concentrations. Although previous studies of precipitated aluminium gels concluded that the primary particles are actually aggregates[15, 54, 57] that have decays less than q^{-4} at high q, USAXS data collected from the smut cannot account for this because of the high background.

The agglomeration of the $Al(OH)_3$ particles can be characterized from the results shown in Table 1, by calculating physically meaningful parameters such as: mass fractal dimension, d_m, degree of agglomeration, z_{deg}, and the connectivity dimension, c. The degree of agglomeration is related to the number of primary particles in each agglomerate and d_m is explained in Chapter 2 as being related to high agglomerate densities as d_m increases from 1 to 3. Connectivity dimensions, c, have been derived based on the shortest possible path through an agglomerate and whether or not this path contains primary particles or voids[69]; if the shortest path contains primary particles, the agglomerate is considered to be linear and have little to no branching.[69] Thus, values of c equal to 1 are associated with linear chains and values of c that approach d_m for branched agglomerates.[69] Values of z_{deg}, d_m and c may be calculated by the equations:

(5.4) $$z_{deg} = \frac{G_2}{G_1} = 200$$

(5.5) $$c = \frac{d_m}{d_{min}} = 1$$

(5.6) $$d_{min} = \frac{B_2 {R_g}_2^{df}}{\Gamma\left({}^{d_m}/_2\right) G_2} = 2.8$$

=where d_m is equal to P_2, Γ is the gamma function, d_{min} is the minimum dimension and all other values are defined in Chapter 2 and given in Table 1.[69] The degree of agglomeration, z_{deg}, is related to the number of primary particles in the agglomerate and the value of c is calculated to be one. Using errors from the model fit, c can vary between 0.77 and 1.24. Even considering a maximum c value of 1.24, very little branching is likely; errors on the order of 100 are obtained for z_{deg}. Results obtained from the model fit indicate that the $Al(OH)_3$ agglomerates are compact agglomerates with little to no branching; although some branching can be calculated when taking into account errors in Table 1, it is negligible[69].

Compact agglomerates with little to no branching indicate that the $Al(OH)_3$ particles must be isolated in the gel and do not form any branched network. The same method can be applied to the *in-situ* data shown in Figure 5.2, with c = 1, z_{deg} = 200 and d_m = 2.77. However, the primary particle size, obtained from R_{g1} is slightly smaller at 69 Å. Larger primary particles obtained *ex-situ*, could be due to drying and aging whereby some of the primary particles aggregate further to increase their size. Similar results obtained from the wet gel indicate that the structure of the agglomerates does not change significantly with drying. Given that the mass fraction of $Al(OH)_3$ has been calculated to be ~5% in the wet gel[34] and the presence of linear agglomerates, it is concluded that the $Al(OH)_3$ particles must exists as isolated, compact particles and not as a branched network.

5.a.5 Conclusions

1) Using ultra small angle X-ray scattering, the scattered intensity from a pitted surface can be obtained. Although modelling the entire $I(q)$ curve is non-trivial, general trends in the Guinier regions (associated with the primary pit sizes), are in agreement with decreasing pit size with increasing frequency.

2) Small angle scattering from smut formed *in-situ* is very different from pit scattering in terms of shape. Although pit scattering was not experimentally removed from *in-situ* SAXS data, it was shown that the scattered intensity from pits does not significantly contribute and that scattering from the smut is dominant. Thus, contributions to the scattered intensity from pits can be neglected in the analysis of the scattered intensity from smut formed *in-situ*.

3) By considering the q-range of the Guinier region found in SAXS data, the size of the scattering population in the smut was determined to be on the order of 10 nm. Considering that the size of this small population does not change with electrograining or quiescent time, it was initially assumed that the SAXS data is not from pores within the smut.

4) The scattering curve, $I(q)$, was modelled as agglomerated $Al(OH)_3$ particles using an appropriate two level unified equation. In accordance with previous SAXS studies on $Al(OH)_3$ gels, the USAXS data was fit to a two-level agglomerated system. Analysis of parameters obtained from the fit result in the presence of compact agglomerates that contain little to no branching, within experimental error. The same equation was also fit to the *in-situ* SAXS data, with similar results to the USAXS data. Given the mass fraction of $Al(OH)_3$ found in the wet smut, it is concluded that the $Al(OH)_3$ particles exist as isolated agglomerates in the wet gel, as opposed to a branched structure.

5.b. Gas Retention

In the previous section, the *in-situ* SAXS data obtained during and after graining showed that the size and shape of the $Al(OH)_3$ particles do not change with electrograining or quiescent time. However, consistent changes in the magnitude of the $I(q)$ curve were observed, keeping in mind that Figure 5.3 is a log-log plot. To quantify the change in magnitude, the so-called "Invariant," Q, is used and defined by the equation:

$$Q = \frac{1}{2\pi^2}\int_0^\infty q^2 I(q)dq = k\,V\overline{\eta^2} \quad (5.7)$$

$$\overline{\eta^2} = \langle\left(\rho_{e_i} - \langle\rho_e\rangle\right)^2\rangle = \sum_{i=1}^{3} \nu_i\left(\rho_{e_i} - \langle\rho_e\rangle\right)^2 \quad (5.8)$$

$$\langle\rho_e\rangle = \nu_A\rho_{e_A} + \nu_{gas}\rho_{e_{gas}} + \left(1 - \nu_A - \nu_{gas}\right)\rho_{e_{sol}} \quad (5.9)$$

where k is a calibration factor, V is the total scattering volume (smut), ρ_{e_i} and ν_i are the electron density and volume fraction of phase i, and $\overline{\eta^2}$ is the "average square fluctuations in electron density" (contrast), and calculated by Equations 5.8 and 5.9; the summation in Equation 5.8 is carried out over all three phases in the smut[70]; the subscript A refers to the $Al(OH)_3$ phase.

To help differentiate between changes in volume, V, and contrast, $\overline{\eta^2}$, SEM imaging and gravimetric mass experiments were performed at the VUB. SEM imaging of smut formed after electrograining and 90 s after electrograining showed that some smut dissolution does occur. Unfortunately, the amount dissolved cannot be readily quantified, because of dissolution during each quiescent period; also, the exact amount of smut formed during each electrograining burst cannot be quantified electrochemically by either, because of the

cathodic corrosion phenomenon[43]. However, V should increase during electrograining as smut grows and decrease during the quiescent period, owing to some dissolution.

Because the scattering is attributed to the $Al(OH)_3$ particles, the presence of gas in the smut will increase $\overline{\eta^2}$ by Equations 5.8 and 5.9. During electrograining, the presence of gas, in the smut, will also increase Q. Any gas released during the quiescent period will then cause Q to decrease. Therefore, contributions from the gas fraction, in the smut, will have the effect on Q as the total volume, V.

5.b.1 DPPD additive

Because V and $\overline{\eta^2}$ have the same effect on Q, two different concentrations of DPPD were added to the HCl electrolyte to purposely form more smut. At the end of 80 s of electrograining, the smut thicknesses obtained in each electrolyte were obtained by SEM imaging, performed by the VUB. In general, the addition of 0.034 M DPPD resulted in a similar smut thickness (Figures 5.5a and 5.5b), but when the concentration was increased, a much thicker and more non-uniform smut was obtained as shown in Figures 5.5c and 5.5d. For better quantification, the total mass of smut formed per area was found to be 1.5 g m^{-2}, 1.5 g m^{-2} and 3.7 g m^{-2} in HCl, HCl + 0.034 M DPPD and HCl + 0.34 M DPPD, respectively. By knowing the amount of smut formed in each case, contributions to Q from the total smut volume, can accounted for.

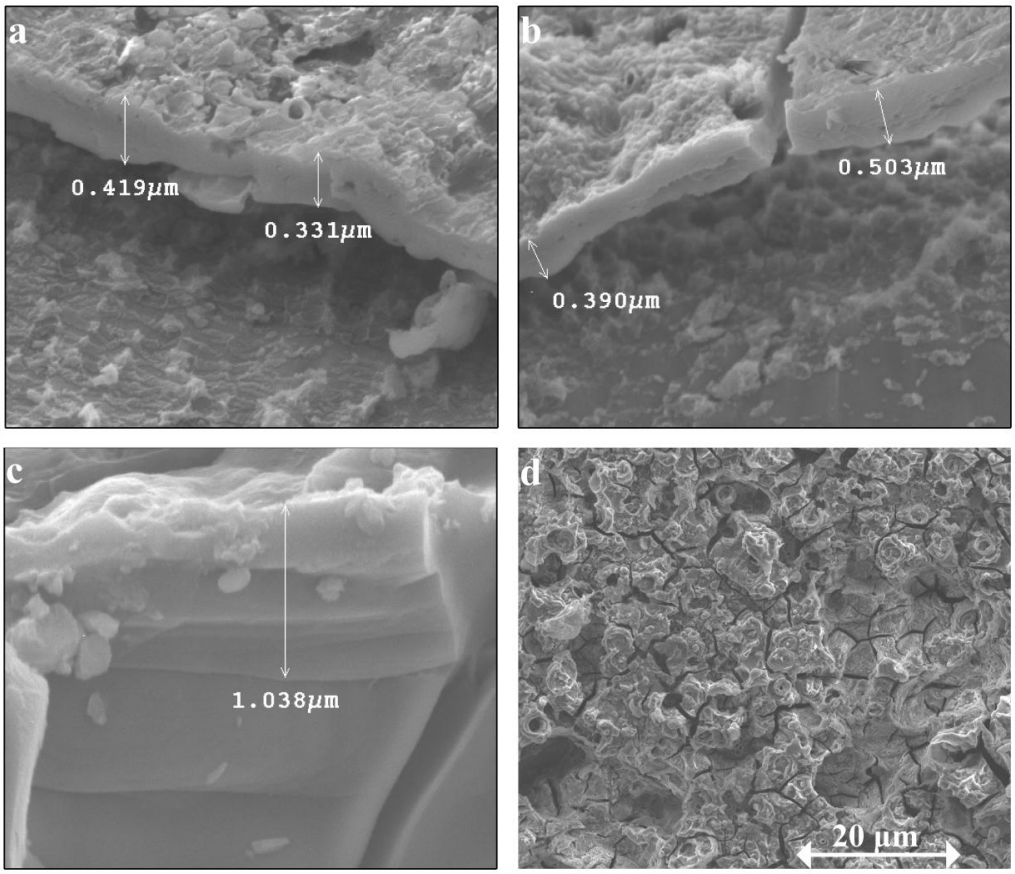

Figure 5.5a, 5.5b and 5.5c are SEM images showing the smut thickness in HCl, HCl+0.034M DPPD and HCl+0.34M DPPD, respectively. Figure 5.5d shows the highly nonuniform smut morphology obtained in HCl+0.34M DPPD.

Figure 5.6 shows that the time dependence of Q for each electrolyte follows a saw-tooth pattern with Q increasing rapidly during electrograining, followed by a slower decay during the following quiescent period. During the quiescent period, the value of Q decreases, except for 10 s after the electrograining burst where Q can be higher than during electrograining. If Q increases more during electrograining than it decreases afterwards, the time average will be higher in the latter case. Therefore, plots of Q *vs.* time have a "saw-tooth" pattern that is expected as V and $\overline{\eta^2}$ change during and after electrograining; this pattern was reproducible for 11 separate samples electrograined in HCl, HCl + DPPD and HNO_3 (not shown here).

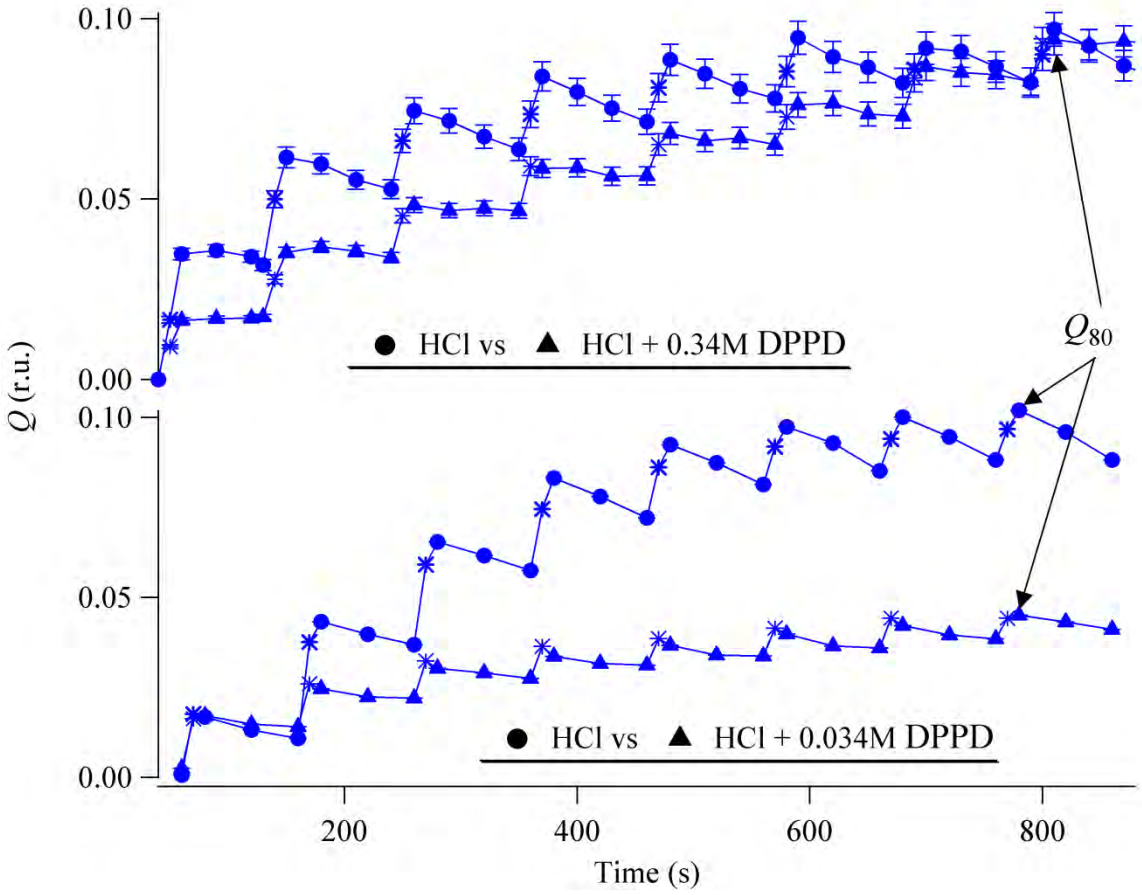

Figure 5.6 is a stack plot of the total scattering, *Q*, versus time for four separate samples electrograined in HCl, HCl + 0.34 M DPPD (top) and HCl, HCl + 0.034 M DPPD (bottom). This figure represents the total scattering for each of the SAXS frames obtained *in-situ*.

Given any two values of Q in Figure 5.6 the additional gas volume, within the smut, can be calculated if the relative volume of smut, V, between the two points is known; the maximum value of Q, obtained after 80 s of electrograining, Q_{80}, is used for this calculation and shown in Figure 5.6. The maximum value of Q, Q_{80}, for smut formed in HCl is a factor of two greater than that observed with 0.034 M DPPD and approximately equal to the sample electrograined in HCl + 0.34 M DPPD. Taking into account the relative amount of smut formed in each electrolyte, this behaviour is unexpected. Since the volume of smut is likely to be very similar, with and without 0.034 M DPPD, the simplest explanation (referring to Equation (5.7)) for the increase in Q_{80}, is an increase in contrast, $\overline{\eta^2}$, found in smut formed in

HCl, caused by the presence of additional hydrogen gas retained in the smut. Gas retention during electrograining is consistent with previous work reporting an increase in resistance observed *in-situ*.[37]

The smut has been shown to contain *ca* 90% water by mass in HCl [34] if equal smut densities are assumed for smut formed in all samples in Figure 5.6; the data may be used to link the smut mass and $Al(OH)_3$ volume. From Equation 5.8, a fractional contrast, $\overline{\eta_f^2}$, can be defined for smut formed in HCl compared to smut formed with HCl + 9.0 g l^{-1} DPPD and HCl + 0.9 g l^{-1} DPPD by the equation:

$$(5.10)\quad \overline{\eta_f^2} = \frac{Q_{80}^{DPPD}/V_{HCl}}{Q_{80}^{HCl}/V_{HCl}} \cong \frac{Q_{80}^{DPPD}/m_{HCl}}{Q_{80}^{HCl}/m_{HCl}} \overset{Eq.5.7}{=} \frac{\overline{\eta_{DPPD}^2}}{\eta_{HCl}^2}$$

where Q_{80}^{HCl} and Q_{80}^{DPPD} are the values of Q_{80}, V_{DPPD}, m_{DPPD} and V_{HCl}, m_{HCl} are the volumes and mass of $Al(OH)_3$ and $\overline{\eta_{DPPD}^2}$ and $\overline{\eta_{HCl}^2}$ are the contrasts in the smut formed with and without DPPD, respectively. Using Equation 5.10 with the Q_{80} values obtained from Figure 5.6 and the respective $Al(OH)_3$ mass, $\overline{\eta_f^2}$ values are calculated to be between 0.37 and 0.43 for both DPPD concentrations. Referring to Equations 5.8 and 5.9, if $\overline{\eta_{HCl}^2} > \overline{\eta_{DPPD}^2}$ a higher volume fraction of gas must be present in smut formed without DPPD, at the two concentrations evaluated. Within experimental error, there is no observable correlation between $\overline{\eta_f^2}$ and DPPD concentration. Gas retention during electrograining is consistent with previous work [37] where the resistance increases with graining time in HCl.

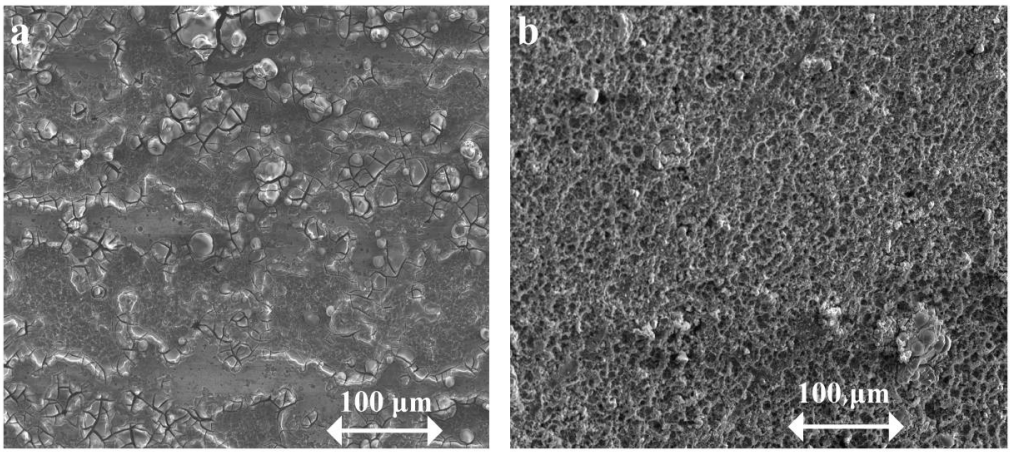

Figure 5.7a and 5.7b are SEM images of the final smut morphology after the graining sequence in Figure 5.6 is a stack plot of the total scattering, *Q*, versus time for four separate samples electrograined in HCl, HCl + 0.34 M DPPD (top) and HCl, HCl + 0.034 M DPPD (bottom). This figure represents the total scattering for each of the SAXS frames obtained *in-situ*.in HCl and HCl+0.034M DPPD, respectively.

Images of the dried smut morphology were obtained from the samples electrograined in HCl and HCl + 0.034 M DPPD, corresponding to the bottom two samples in Figure 5.6. The dried smut morphology obtained from electrograining in HCl can be described as a uniform "mud-like" layer and shown in Figure 5.7a. On the other hand, addition of 0.034 M DPPD resulted in a porous smut morphology very different from that obtained in HCl and shown in Figure 5.7b. The smut morphology obtained in HCl + 0.34 M DPPD was very nonuniform, as shown in Figure 5.5d.

5.b.2 Discussion

Using the custom designed flow cell described in Chapter 3, *in-situ* SAXS data was obtained during electrograining experiments. During the long quiescent times, there was a constant flow, during which smut dissolution occurs. This prevents extraction of any quantitative decay in the gas fraction from *Q*. Similarly, without knowing the smut production rate during each burst, the gas fraction retained during electrograining cannot be calculated. However, by incorporating data from gravimetric experiments with different concentrations of the

DPPD additive, the final smut volume is known and the presence of an additional gas fraction may be determined via minimal data manipulations. The presence of gas gives a rational explanation for the additional resistance present during electrograining.[37] Given the room temperatures that these experiments were performed at, the concentration of dissolved H_2 gas is predicted to be a maximum of 0.1 M during bubble growth, at the interface[71]. Values this low would have a negligible effect on the electron density, as the concentration of water and $AlCl_3$ (saturation) must be at more than an order of magnitude greater. Thus, the gas is considered to exist as a separate bubble phase.

Bubbles that stick to the metal surface (from H_2 evolution during the cathodic cycle) would render it inactive[71], while other portions of the surface dissolve. This effective decrease in the active electrode area would cause a non-uniform current across the surface, which would certainly result in non-uniform pitting that is paramount in this study. Bubbles that do not stick to the surface (possibly held up in the smut) would cause the required potential to increase (Equation 2.44), observed in recent *in-situ* experiments.[37]

The presence of pores observed in the dried smut formed with HCl + 0.034 M DPPD (Figure 5.7b) would accommodate gas release during electrograining, while no such porosity is directly observed in the HCl sample. In addition, SEM imaging shown in Figure 5.5d reveals a smut layer that contains large holes and thicker mounds on the electrode surface as the concentration of DPPD is increased to 0.34 M,[36] which could also accommodate gas release. In the absence of DPPD, the hydrogen seems to permeate through the smut in a more uniform manner, which does not result in observed porosity shown in Figure 5.7a.

5.b.3.i Gas Fraction

By applying Equation 5.10 to Q_{80} values in Figure 5.6, an increase in Q was attributed to a gas fraction, without any estimation of the gas fraction. An estimation of the gas fraction is useful as a reality check to be sure the values are not too high or too low. Gas fractions too high (approaching 100%) would imply that most of the water in the gel is replaced by gas, and values this high would be unrealistic if most of the smut remains intact during electrograining. Conversely, gas fractions less than 1% would imply that very little of the gas is retained in the smut. To obtain an estimate of the gas fraction in the smut formed in HCl, the values of Q_{80}, obtained from HCl and HCl+0.034 M DPPD (bottom two curves in Figure 5.6) were used.

To estimate the gas fraction using Equation 5.6, knowledge of the $Al(OH)_3$ speciation, density and volume fraction of $Al(OH)_3$ in the smut. In addition, Equation 5.10 requires knowledge of the gas fraction in one of the samples. Because the smut formed with 0.034 M DPPD was shown to retain a lower gas fraction than with HCl only, a negligible gas fraction is assumed in the 0.034 M DPPD sample. This assumption can be validated by considering the ratio of Q_{80} to Q_L, with the latter being the last point in the HCl + 0.034 M DPPD curve in Figure 5.6. Experiments carried out independently at the VUB showed that density of dried smut is 3.6±0.63 g cm^{-3} using the average smut mass and thickness measurements in HCl; further, the exact stoichiometry was found to be $Al(OH)_{2.7}$. Using these values, the scattering length density for the $Al(OH)_3$ particles can be calculated by the equation:

(5.11) $\rho_{e_A} = \frac{n_e \rho_m N_A}{MW} r_e = 31.26 \times 10^{10}\ cm^{-2}$

where n_e is the number of electrons in each molecule, ρ_m is the mass density, N_A is Avogadro's number, *MW* is the molecular weight and r_e is the electron radius. The scattering length density of the electrolyte and gas were taken to be that of water and a vacuum, 9.36×10^{10} cm^{-2} and 0 cm^{-2}, respectively. The volume fraction of $Al(OH)_3$, ν_A, was taken as 0.014, obtained from the 5% mass fraction reported[34] and mass density previously mentioned. It follows that the value of ν_{gas}^{DPPD} is calculated by the equation:

$$\frac{Q_{80}^{DPPD}}{Q_L^{DPPD}} = \frac{\left(\nu_A\left(\rho_{e_A}-\langle\rho_e\rangle\right)^2+\nu_{gas}^{DPPD}\left(\rho_{e_{gas}}-\langle\rho_e\rangle\right)^2+\left(1-\nu_{gas}^{DPPD}-\nu_A\right)\left(\rho_{e_{sol}}-\langle\rho_e\rangle\right)^2\right)}{\left(\nu_A\left(\rho_{e_A}-\langle\rho_e\rangle\right)^2+\left(1-\nu_A\right)\left(\rho_{e_{sol}}-\langle\rho_e\rangle\right)^2\right)} \quad (5.12)$$

where $\nu_{gas}^{DPPD}$is the gas fraction in smut formed in HCl + 0.034 M DPPD after 80 s of graining and $\langle\rho_e\rangle$ is calculated by Equation 5.9, using the corresponding gas fractions. The value of ν_{gas}^{DPPD}, at Q_{80}, is calculated to be 0.8%, assuming no dissolution 90 s after the last electrograining burst. Because of the uncertainty in ν_{gas}^{DPPD} and ν_A, a contour plot of ν_{gas}^{HCl} was made with values of ν_{gas}^{DPPD} and ν_A varying between 0 to 0.01 and 0.01 and 0.05, respectively. Using these values of ν_{gas}^{DPPD} and ν_A with the scattering length densities, the final equation to solve for the gas fraction in HCl, ν_{gas}^{HCl}, is:

$$\frac{Q_{80}^{HCl}}{Q_{80}^{DPPD}} = \frac{\left(\nu_A\left(\rho_{e_A}-\langle\rho_e\rangle\right)^2+\nu_{gas}^{HCl}\left(\rho_{e_{gas}}-\langle\rho_e\rangle\right)^2+\left(1-\nu_{gas}^{HCl}-\nu_A\right)\left(\rho_{e_{sol}}-\langle\rho_e\rangle\right)^2\right)}{\left(\nu_A\left(\rho_{e_A}-\langle\rho_e\rangle\right)^2+\nu_{gas}^{DPPD}\left(\rho_{e_{gas}}-\langle\rho_e\rangle\right)^2+\left(1-\nu_A-\nu_{gas}^{DPPD}\right)\left(\rho_{e_{sol}}-\langle\rho_e\rangle\right)^2\right)} \quad (5.13)$$

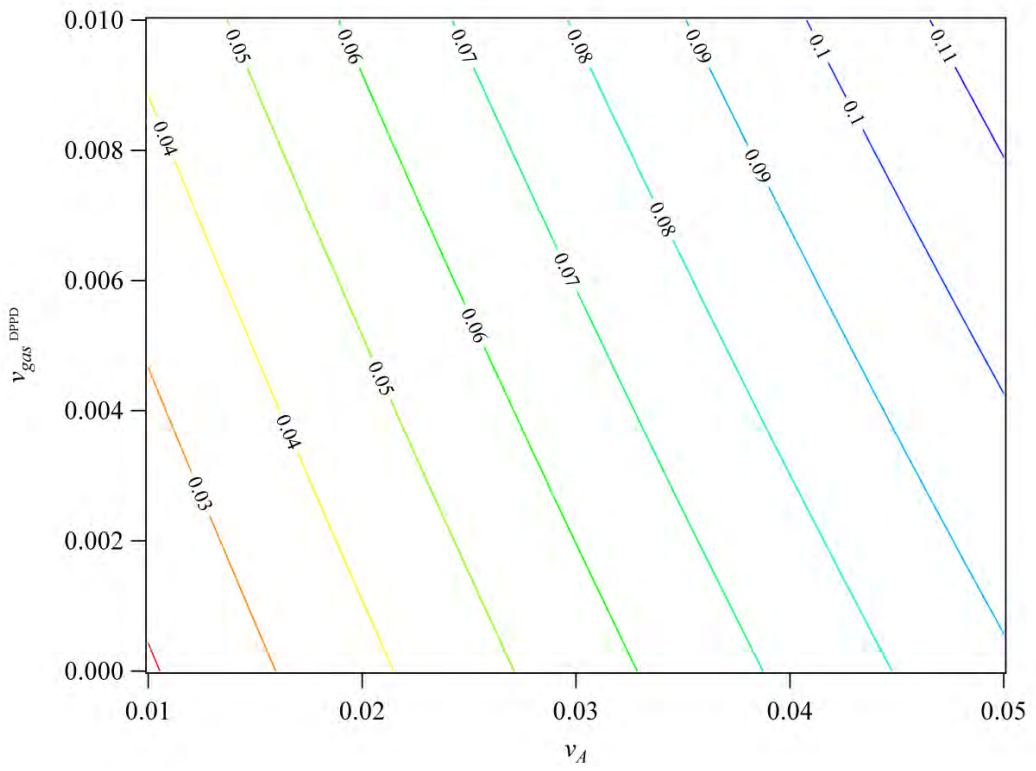

Figure 5.8 is a contour plot showing the estimated gas fractions for different volume fractions of $Al(OH)_3$ and gas fractions present with the 0.034 M DPPD additive.

Figure 5.8 is a contour plot of the gas fraction, v_{gas}^{HCl}, as a function of v_{gas}^{DPPD} and v_A. Because of the low values of v_{gas}^{DPPD} and v_A, the relationship is approximately linear, as expected. Gas fractions between 2% and 11% are estimated to be present in the smut formed in HCl only. These values indicate that the evolved gas occupies only a small volume of the smut just after electrograining. However, because the values of Q_{80} are time averaged values, gas fractions calculated would be underestimated. Therefore, gas fractions between 2% and 11% can be considered a minimum range.

Because the $Al(OH)_3$ particles are shown to be isolated agglomerates, in the smut, the smut would not be expected to be mechanically rigid and would be prone to rupture if too much gas was passed through it; although, no threshold gas fractions for smut rupture can be obtained, the gas fractions calculated are believed to be small enough to prevent rupture. On

the other hand, gas fractions approaching 100% would imply suspended $Al(OH)_3$ agglomerates in a convective gas flow, which would easily remove them from the smut. Therefore, the estimated gas fraction range is considered to be a reasonable estimate, given the nature of the $Al(OH)_3$ structure in the smut.

5.b.3 Conclusions

1) *In-situ* SAXS experiments were successfully performed, in transmission, to identify the presence of gas in a gel (smut) layer, which forms on the surface of each electrode during AC electrograining.

2) Analysis of the total scattering, *Q*, together with smut mass measurements, led to the conclusion that there is a higher gas fraction in smut formed in HCl compared with smut formed with 0.034 M DPPD. A qualitative electrochemical argument was developed to explain how the presence of retained gas could affect local dissolution kinetics during electrograining in agreement with *in-situ* potential measurements.

3) Using the density and speciation of the $Al(OH)_3$ particles, obtained by the VUB, a method of estimating the gas fraction is presented. This method requires prior knowledge of the relative smut volumes and the gas fraction in at least one of the samples. The gas fraction, in smut formed in HCl, was estimated to be between 2% and 10% and was considered to be reasonable, given the nature of the smut.

5.c Gas Permeation and Final Surface Morphology

Work presented in the previous sections has demonstrated that under certain conditions, the smut formed during electrograining is able to retain a fraction of gas. With this knowledge, final experiments were designed to improve understanding of gas release and retention under different electrograining conditions. Since gas present in the smut is believed to be the source of the increase in the measured potential reported previously[37], the potential response was measured throughout the experiment, during SAXS data collection; the potential, Φ, reported here is the maximum (anodic) and minimum (cathodic) potential during each cycle, instead of the measured potential during the entire cycle. To minimize the effect of smut dissolution, during the quiescent period, flow was stopped immediately after electrograining; and in addition, shorter quiescent times were also used. The role of gas permeation, through the smut, and its influence on the final surface morphology was investigated by measuring the gas release, retention, potential response and dried smut and final surface morphology.

Based on previous work, three additives were used to manipulate the smut and final surface morphology[36]. The frequency has been shown to inversely affect the amount of smut formed[34], and preliminary experiments showed that very different potential responses were observed at 50 Hz and 100 Hz, with the latter showing a much higher potential response. Thus, samples were electrograined in 0.34 M HCl, 0.34 M HCl + 0.3 M acetic acid, 0.34 M HCl + 0.03M citric acid , 0.34 M HCl + 0.03M DPPD, all at 50 Hz and 100 Hz for a total of eight samples. Samples electrograined in 0.34 M HCl at 50 Hz and 0.34 M HCl + 0.03M citric acid at 50 Hz were reproducible for two separate experiments; reproducibility for other samples could not be evaluated because the ion chamber data recorded to the calibration file were not reliable values of I_o and I_t, as they abruptly changed values throughout the experiment. This made a plot of Q *vs.* time impossible to analyse for these experiments.

5.c.1 $Al(OH)_3$ Small Angle Scattering

SAXS data was collected in a series of 2 s frames that could be summed together subsequently to optimize the intensity signal and time resolution. After the 10 s graining period, one 4 s frame followed by 6-6 s images was found to give the best time resolution, whilst providing a smooth scattering curve characteristic of $Al(OH)_3$ gels. Figure 5.9 is a plot of the intensity (I) *vs.* the magnitude of the scattering vector (q) 40 s after the last electrograining burst (last 6 s frame). The general behaviour of each $I(q)$ curve, common to all SAXS data, is the same as observed in previous *in-situ* experiments and was modelled as discussed previously.

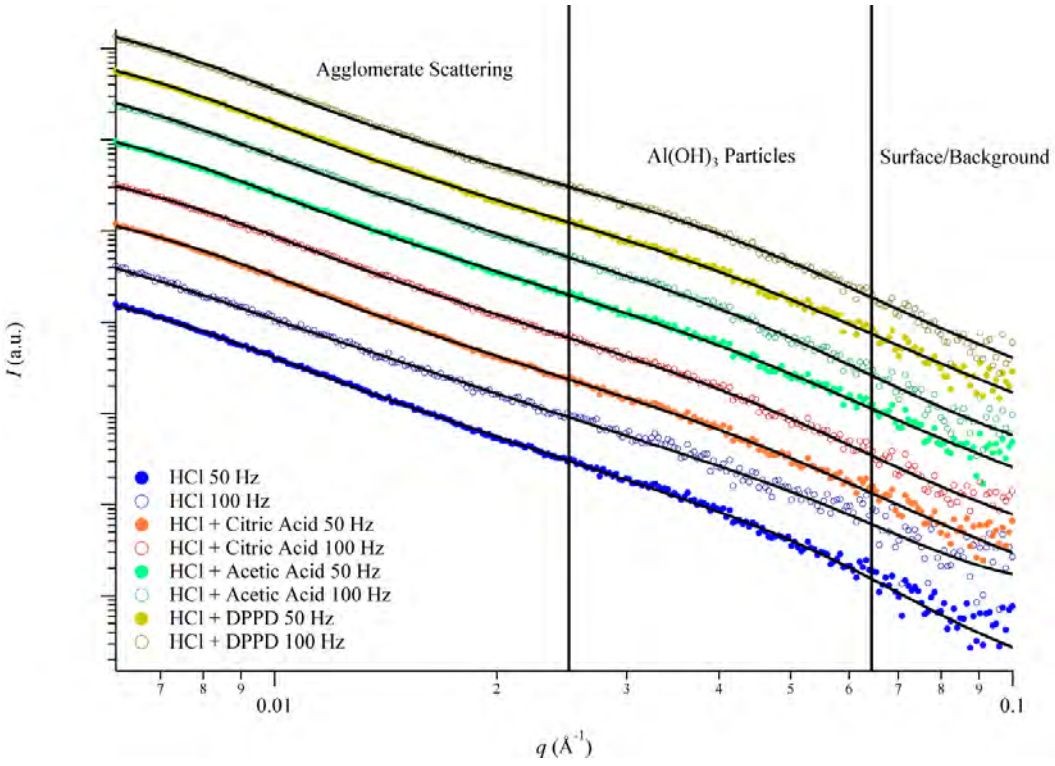

Figure 5.9 is a log-log plot of the SAXS data obtained 40 s after a total electrograining time of 80 s for all samples.

Results obtained from the fit of Equation 5.3 to the data are tabulated in Table 3. In all cases, values of c~1 were obtained, indicating linear agglomerates with little to no branching, as before. Interestingly, smaller primary particle sizes were obtained in all cases, compared to

previous *in-situ* experiments performed at much slower flows and longer quiescent times. Smaller $Al(OH)_3$ particle sizes are consistently observed in every sample here, which could be due to the increase in mass transport of electrolyte to the aluminium surface by the increase in flow during electrograining (10 ml min^{-1}), compared with 3 ml min^{-1} used previously.

The degrees of agglomeration, z_{deg}, are the same order of magnitude as those obtained from the *ex-situ* USAXS data. The sample electrograined at 100 Hz in HCl has a much higher value of z_{deg}, smaller primary particle size, R_{g1} and lower mass fractal dimension, d_m than other samples, which indicates the presence of loosely packed agglomerates that contain a larger number of smaller particles. On the other hand, the opposite is observed with the DPPD additive, at 100 Hz, where z_{deg} is lowest, R_{g1} is largest and d_m is highest, indicating compact agglomerates that are made up of fewer but larger primary particles. Results indicate that the size of the agglomerates remain unchanged. However, because of the limited *q*-range available, the complete size distribution of the agglomerates is unknown and the Guinier knee at very low *q* represents only the smallest measurable agglomerates in all samples.

Clear differences in z_{deg}, R_{g1} and d_m between the two samples indicate that the internal structure of the $Al(OH)_3$ agglomerates can be affected by the electrolyte and frequency. Although, the change in the internal agglomerate structure is not understood, the change in structure is not considered to directly influence gas permeation because the agglomerates are considerably compact ($d_m > 2.7$). Because agglomerates are isolated and dilute[34], the space inside the agglomerates would likely not trap gas. It is more likely that gas would take the path of least resistance around the agglomerates; all agglomerates should still be considered isolated, "linear" agglomerates, with little to no branching because $c \sim 1$ for all samples.

Therefore, it is concluded that whilst there are some structural differences in the $Al(OH)_3$ agglomerates at different electrograining conditions, all can be considered isolated, linear agglomerates (c~1), as observed previously.

Table 2 lists the results obtained from the unified equation fit to the raw data shown in Figure 5.9.

Parameters/ Sample	z_{deg}	R_{g1} (Å)	R_{g2} (Å)	d_m
HCl 50 Hz	300	46 ± 1	333 ± 16	2.87 ± 0.02
HCl 100 Hz	500	40 ± 1	368±36	2.71 ± 0.02
HCl + Citric Acid 50 Hz	200	51 ± 1	316 ± 11	2.92 ± 0.03
HCl + Citric Acid 100 Hz	200	52 ± 1	316 ± 12	2.88 ± 0.02
HCl + Acetic Acid 50 Hz	200	52 ± 2	331 ± 15	2.88 ± 0.03
HCl + Acetic Acid 100 Hz	200	50 ± 1	350 ± 20	2.85 ± 0.02
HCl + DPPD 50 Hz	200	53 ± 1	334 ± 15	2.92 ± 0.03
HCl + DPPD 100 Hz	100	53 ± 1	329 ± 13	2.95 ± 0.03

5.c.2 Gas and Measured Potential

The temporal behaviour of Q and V are shown in Figure 5.10 for samples electrograined with HCl at 50 Hz and 100 Hz. As before, the same saw-tooth pattern can be observed, with Q increasing during and (sometimes) just after electrograining, followed by a decrease during the quiescent period. At 100 Hz, the temporal changes in Q are smaller than at 50 Hz, while Φ is larger in magnitude. Differences in the magnitude of Q can be attributed to differences in the total $Al(OH)_3$ volume or a gas fraction, in the smut, by Equation 5.10. Using the relative smut masses from each frequency, differences in the retained gas can be calculated

(Section 5.c.4.i), but the *Q* curves cannot be normalized to the smut mass throughout the experiment because only the final smut masses are known. On the other hand, differences in *Φ*, particularly during the cathodic cycle, are attributed to differences in gas pressure at the reaction plane of the working electrode or gas present in the smut (Equations 2.46 and 2.44, respectively). Differences in the gas fraction and gas pressure, taken from the *Q* and *Φ* data, respectively, are analysed further in Section 5.c.4.

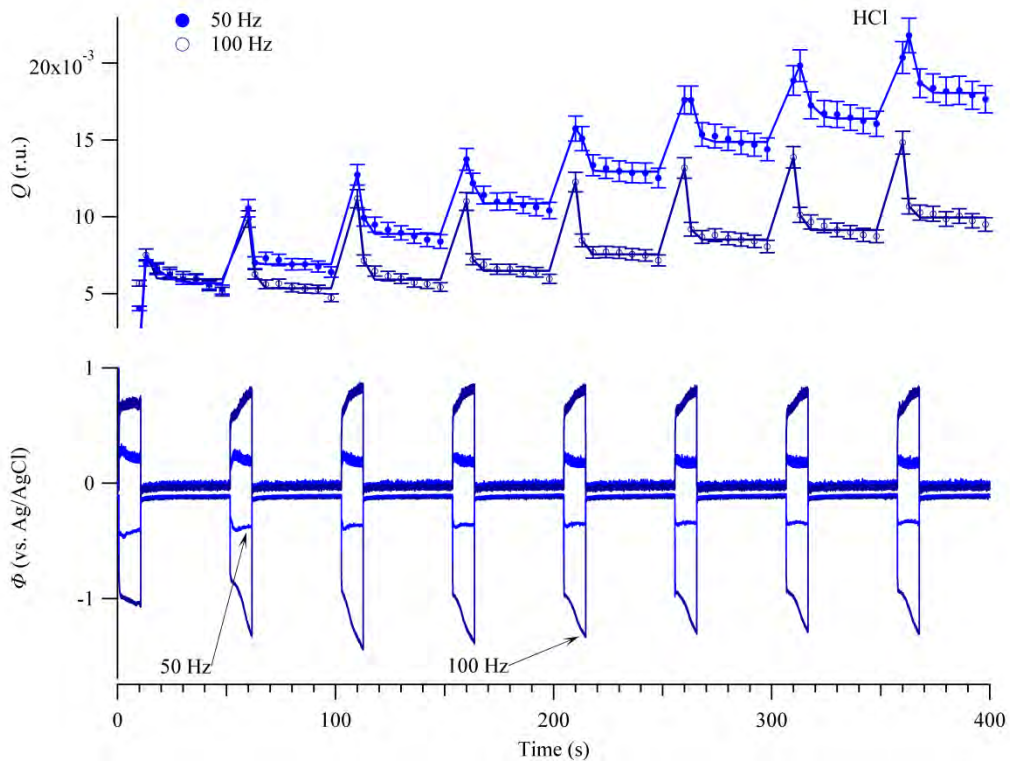

Figure 5.10 is a stack plot of Q *vs.* time (top) and the potential response *vs.* time (bottom) for the samples electrograined in HCl, at 50 Hz and 100 Hz. The first point in the Q *vs.* time curve is not zero and is the value of Q obtained during the first electrograining burst.

The decrease in *Q*, after graining, also depends on the frequency as shown in Figure 5.10. Following previous results that led to the inference of gas retention in the smut, differences in the decrease in *Q* after electrograining indicate differences in gas release between the two frequencies. To characterize the decay in *Q*, *Q vs.* time data were fit to a model assuming a linear increase in *Q* during electrograining and a sigmoid type function during each quiescent

period; previous experiments of 5 s frames during electrograining have shown that a linear increase in Q is a good assumption. The empirical, sigmoid type, function is given by the equation:

(5.14) $$Q(t) = Q_f + S(t) - S(t_f)$$

(5.15) $$S(t) = \frac{-K_1}{\left(1+e^{-\left(\frac{(t-t_f)-K_2}{K_3}\right)}\right)}$$

where Q_f and t_f are the values of Q and time at the end of electrograining burst, K_1 determines the total decrease in Q and K_2 and K_3 are related to the rate at which Q decreases. Equations 5.14 and 5.15 are entirely empirical and serve only to characterize the initial (~10 s) decrease in Q, as smut dissolution will begin to influence Q at longer times. From Equations 5.7 through 5.9, the value of Q will vary linearly with v_{gas} at small values of v_A, estimated in Section 5.b.3.i. Thus, to a first approximation, K_1 would be related to the total gas released in each burst. The fit of Equations 5.14 and 5.15 to the Q *vs.* time data are shown as a solid line in Figure 5.10; the solid line is always contained within the experimental error, except for the first burst in each sample where the data is very noisy.

By convention, gel or membrane diffusion is characterized by a time, t_{lag}, at which the flux of the diffusing species, in the membrane, reaches a steady state value.[72] It is not possible to use this quantity here because gas concentration is not maintained at the metal/smut interface during the quiescent period. Diffusion of gas through the smut is therefore characterized by the time required, t_m, for Q to decrease to a midpoint value between the initial and final Q value. The value of t_m, though strictly empirical, serves to identify differences in gas transport in the absence of a larger pressure gradient present during electrograining. The

value of t_m would therefore be inversely related to the diffusivity, D, of gas in the smut and is used to relate the gas diffusivity, through the smut, after electrograining in each sample. The gas is considered to be mostly hydrogen in all samples and differences in t_m are attributed to the smut's ability to allow the gas to diffuse.

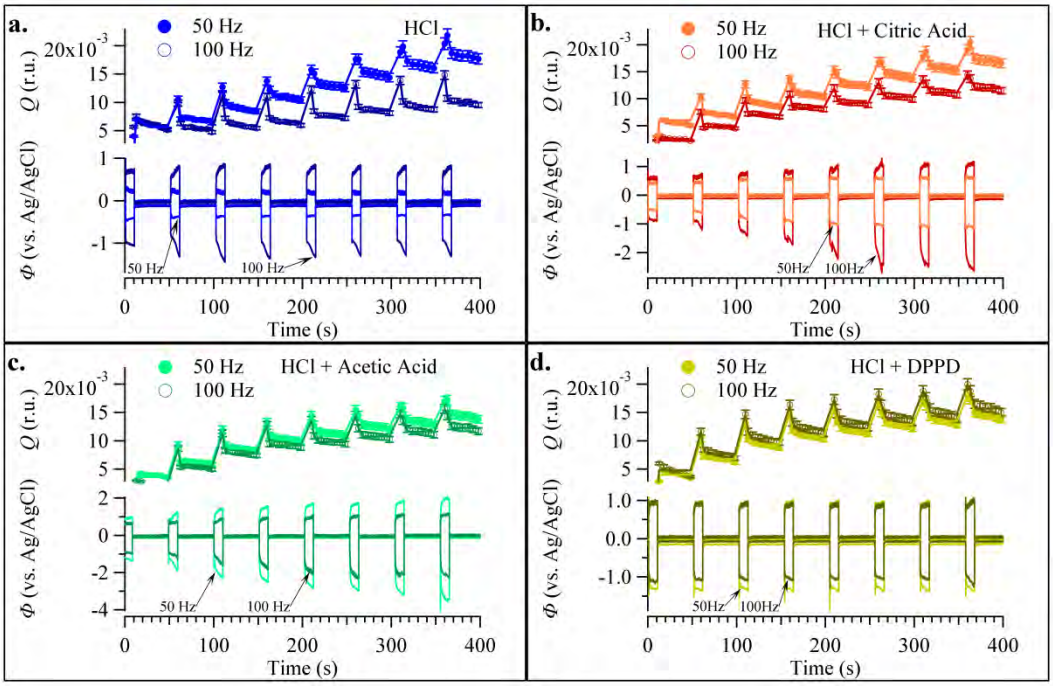

Figure 5.11a, 5.11b, 5.11c and 5.11d are plots of *Q* and potential response *vs.* time for each electrolyte. Each plot contains results obtained from 50 Hz and 100 Hz.

Figures 5.11a, 5.11b, 5.11c and 5.11d show plots of Q (Equation 5.7) and the measured potential *vs.* time for samples electrograined with HCl, HCl+citric acid, HCl+acetic acid and HCl+DPPD, respectively. Equations 5.14 and 5.15 were fitted to the data (solid lines in Figures 5.11a through 5.11d) to extract values of t_m and K_1 from each sample, to evaluate differences in gas release between each sample. Significant differences between 50 Hz and 100 Hz are observed only for HCl and a citric acid additive, with respect to the temporal behaviour of Q and Φ (Figures 5.11a and 5.11b).

With acetic acid and DPPD, there is little difference in the temporal behaviour of *Q* at different frequencies (Figures 5.11c and 5.11d); although small differences in the *Q* decay after electrograining can be observed. The potential response, with acetic acid, generally increases at both frequencies during electrograining; in contrast to HCl only, the measured potential is higher at 50 Hz than 100 Hz, with acetic acid. On the other hand, the potential response with the DPPD is approximately the same at either frequency, with both increasing during electrograining.

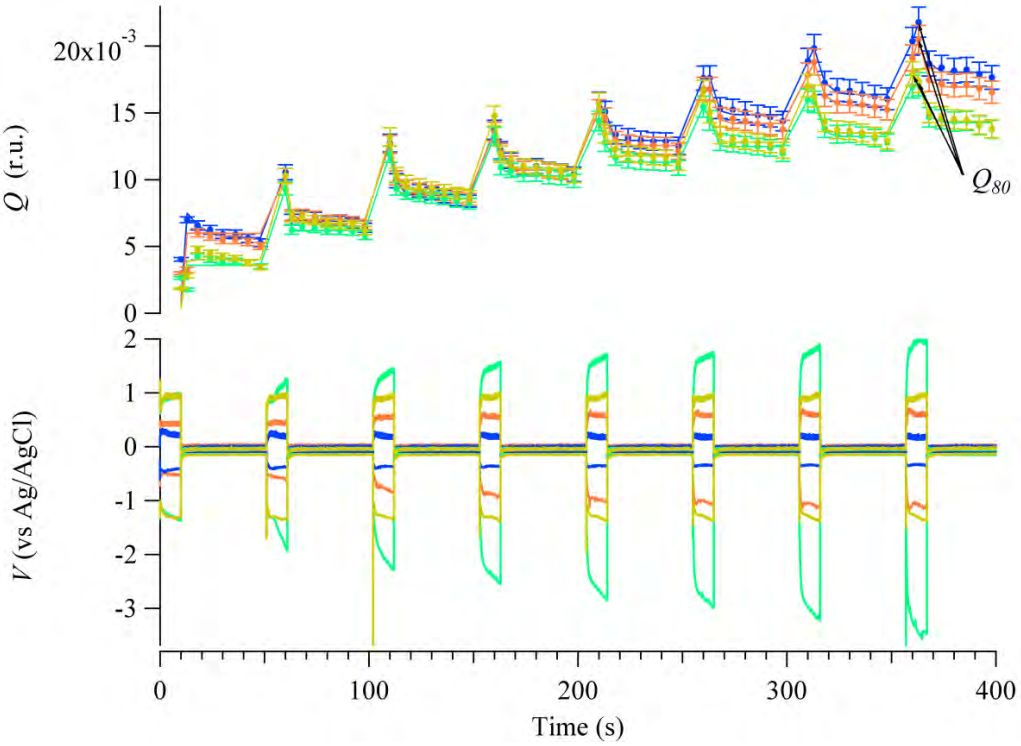

Figure 5.12 is a stack plot showing the differences in the temporal behaviour of Q (top) and V (bottom) for each of the four electrolytes electrograined at 50 Hz. Plots of Q cannot be scaled to the relative amounts of smut because the relative smut masses are only known after a complete electrograining sequence.

Finally, at 50 Hz, the temporal behaviour of *Q* and *Φ* change with additive used and shown in Figure 5.11. Differences shown in Figure 5.11 are expected, as the addition of additives has been shown to drastically change the smut morphology[36]. Samples electrograined with HCl only and with citric acid have relatively higher *Q* values compared to the other two samples.

Higher *Q* values could be due to a difference in retained gas or total smut volume and is discussed later. The measured potential, for the HCl and HCl+citric acid, is lower in magnitude and does not increase monotonically during electrograining, as both are the case with acetic acid and DPPD. Thus *in-situ* data, obtained from HCl and HCl + citric acid, is markedly different compared to samples electrograined in acetic acid and DPPD.

5.c.3 SEM imaging

Figures 5.13a through 5.13h show SEM images of the dried smut obtained from different electrograining conditions. In general, smut morphologies can be described by their porosity, which is defined traditionally as the area fraction available for transport; although transport through the gel itself is also possible the term porosity used here refers to the area fraction of holes. The dried smut at 50 Hz in HCl displays very few noticeable pores and can be described as a uniform mud-like layer. Smut formed in citric acid is similar to that formed in HCl, but does contain some visible holes. When the frequency is increased to 100 Hz, an increase in the porosity is observed in all samples; these pores appear to have some tortuosity to them and are not straight line paths to the metal. The incorporation of additives also produces porosity at 50 Hz, with the size of the pores smallest in acetic acid and largest in DPPD.

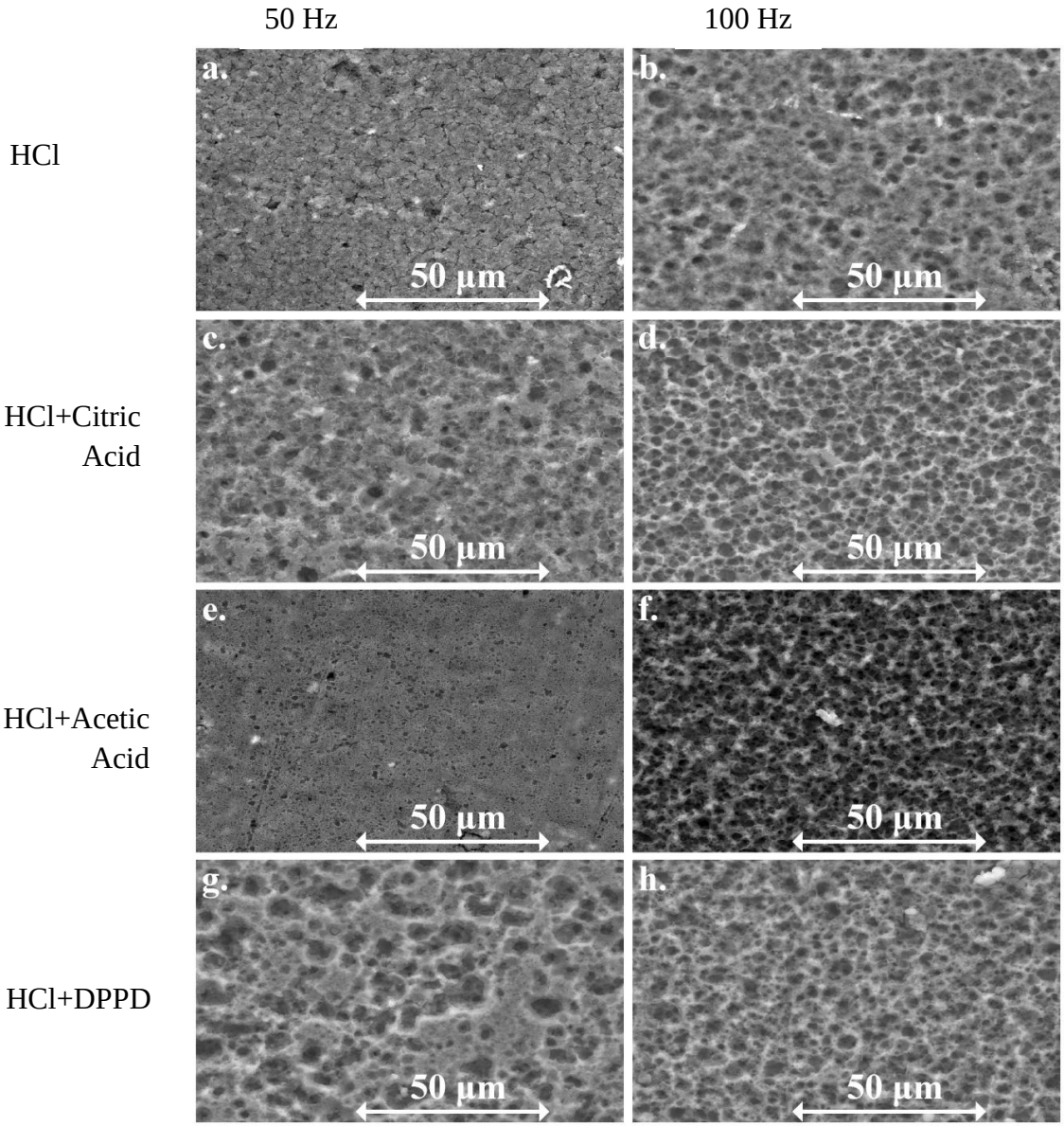

Figure 5.13 are SEM images from dried smut obtained from the experimental sequences shown in Figure 5.11. Figures 5.13a and 5.13b are images of smut formed in HCl at 50 Hz and 100 Hz, respectively. Figures 5.13c and 5.13d are images of smut formed in HCl +citric acid at 50 Hz and 100 Hz, respectively. Figures 5.13e and 5.13f are images of smut formed in HCl +acetic acid at 50 Hz and 100 Hz, respectively. Figures 5.13g and 5.13h are images of smut formed in HCl + DPPD at 50 Hz and 100 Hz, respectively

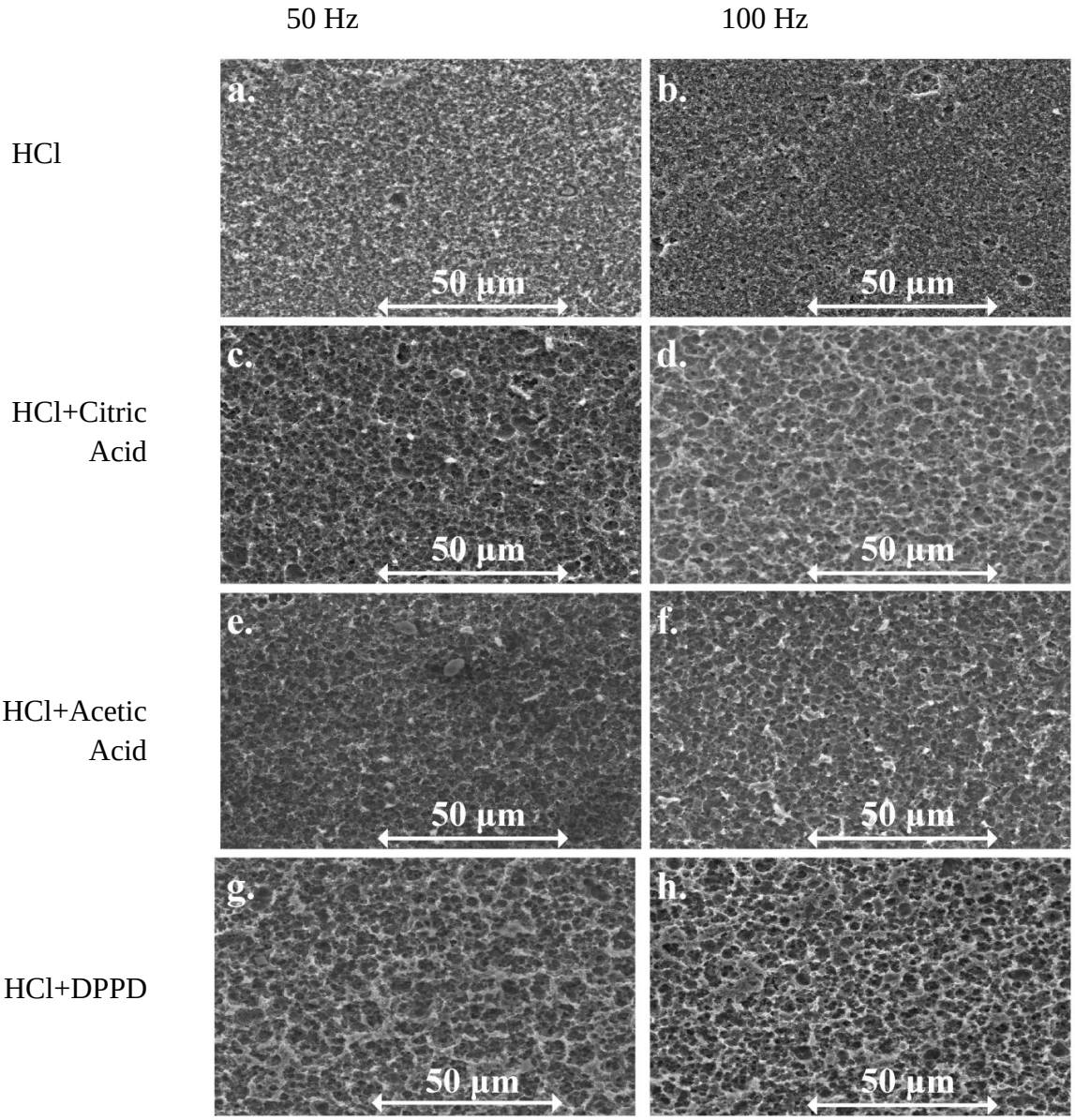

Figure 5.14 are SEM images after smut removal obtained from the experimental sequences shown in Figure 5.11. Figures Chapter 1 Introduction5.14a and 5.14b are images of metal surface formed in HCl at 50 Hz and 100 Hz, respectively. Figures 5.14c and 5.14d are images of the metal surface formed in HCl +citric acid at 50 Hz and 100 Hz, respectively. Figures 5.14e and 5.14f are images of the metal surface formed in HCl +acetic acid at 50 Hz and 100 Hz, respectively. Figures5.14g and 5.14h are images of metal surface formed in HCl + DPPD at 50 Hz and 100 Hz, respectively.

Figures 5.14a through 5.14h show SEM images of the aluminium surface after smut removal described in the experimental section. In all samples, a uniform pit morphology[29] is observed except for the sample grained in HCl at 50 Hz. At this frequency, an etched-like morphology[29] is observed. Thus, all images in Figure 5.14 are categorized as having either a uniform pit morphology or an etched-like morphology. However, pits observed with the

DPPD additive are much deeper than all other samples. The absence of observable porosity in Figure 5.13a correlates with the absence of micron sized pits observed in Figure 5.14a, both of which are observed in all other samples.

5.c.4 *In-situ* Data Interpretation and Analysis

Recent *in-situ* work has shown that information about the gas retention can be obtained from the magnitude in Q[33], as discussed in Section 5.b. The potential response (after the initial smut formation) has previously been attributed to the presence of the smut[37] and is taken to be from the gas in this study, which induces an overpotential, owing to the presence of the smut. To evaluate any possible correlation between the gas/smut and measured potential, meaningful parameters must be extracted from the Q *vs.* time data that characterise gas retention and release. In the sections that follow, differences in the magnitude of Q^{80}, shown in Figure 5.12, are used to estimate differences in gas retention during the final electrograining burst.

Following a comparison of retained gas between samples electrograined at 50 Hz, an interpretation of the measured potential is presented. This interpretation relates the temporal behaviour of Φ to the partial gas pressure during electrograining. Because factors such as differences in electrolyte conductivity and surface inhibition will clearly affect the magnitude of the potential response, differences in the temporal behaviour of Φ during electrograining are relevant to this study. In general, the potential response shown in Figures 5.11a through 5.11d either increases during electrograining or does not, with the latter being the case for the samples electrograined at 50 Hz in HCl and HCl + citric acid. These two general trends indicate differences in the smut permeability and are discussed further in Section 5.c.4.ii.

Differences in the smut permeability, smut morphology and aluminium surface morphology can provide insight into how the smut affects aluminium dissolution. However, to better understand how the gas is permeated through the smut, information about gas diffusion can be used, as it is readily available from values of t_m. Gas diffusion and gas permeation are two different gas transport phenomena, with the former occurring in the absence of a pressure gradient. Because the same gas (H_2) is evolved in all samples, the same differences in the gas permeability and gas diffusion should be observed. However, it will be shown that this is not the case and suggests that the smut's mechanical properties, which ultimately determine gas transport, depend on the frequency and electrolyte.

5.c.4.i Gas Retention

If the relative amount of smut formed is known, differences in gas retention can be evaluated using Equation 5.10. The amount of smut obtained, at 50 Hz, was calculated by gravimetric experiments at the VUB and shown in Table 3. The frequency dependence of smut formation, in HCl, has been reported previously[34] and also shown in Table 3; relative smut masses for samples electrograined at 100 Hz, with different additives, were not obtained. Using smut masses, relative to HCl at 50 Hz, the fractional contrast, $\overline{\eta_f^2}$, for sample, *i*, are calculated by the equation:

$$\overline{\eta_f^2} = \frac{{Q_{80}}_i / m_i}{{Q_{80}}_{HCl-50Hz} / m_{HCl-50Hz}} \quad (5.19)$$

Taking the relative smut masses into account, values of $\overline{\eta_f^2}$ calulated by 5.18 are a measure of the relative gas fraction present in the smut after 80 s of electrograining and tabulated in Table 3. The amount of gas present in the smut, during the electrograining burst, increases

according to the order: HCl+Acetic acid at 50 Hz < HCl at 100 Hz < HCl+DPPD at 50 Hz < HCl+Citric acid at 50 Hz < HCl at 50 Hz.

Table 3 is the results obtained for the relative smut masses, relative gas fractions during electrograining calculated by Equation 5.19. Errors in can be taken as $\pm$ 0. 1, as estimated from the errors in Figures 5.11a through 5.11d

Parameter/Sample	Relative smut mass[2] ($m_i/m_{HCl\text{-}50\ Hz}$)	Fractional contrast During Electrograining $(\overline{\eta_f^2})$
HCl+Acetic acid 50 Hz	1.25	0.6
HCl 100 Hz	0.86	0.8
HCl+DPPD 50 Hz	1.00	0.8
HCl+Citric acid 50 Hz	1.10	0.9

The smut formed in HCl, at 50 Hz, contains the most gas. The fractional contrast calculated with the DPPD additive is greater than that obtained in Section 5.b.1 and could be due to differences in the electrolyte flow, as hydrogen evolution has been shown to be mass transport controlled[29]. Refering to SEM images obtained from the dried smut morphology from samples electrograined in HCl and HCl + citric acid at 50 Hz, higher gas retentions correlate with a low smut porosity (Figures 5.13a and 5.13c). Furthermore, the temporal behaviour of Φ for these two samples, does not steadily increase during electrograining, unlike all other samples (Figure 5.11). Although relatively large errors are associated with $\overline{\eta_f^2}$, there appears to be a correlation between the relative gas retention, temporal behaviour of Φ and dried smut morphology.

[2] From work performed and documented by Ben Wilson at the VUB.

5.c.4.ii Potential Evolution

The peak cathodic potential measured is the potential required for hydrogen reduction[73] and aluminium dissolution[45] by the equations:

(5.16) $2H^+ + 2e^- \rightarrow H_2$

(5.17) $Al + 4H_2O + e^- \rightarrow 2H_2 + Al(OH)_4^-$

Both reactions produce H_2 gas during electrograining[34] and are considered to be mass transport controlled[29]. As discussed in Section 5.b.2, bubbles that stick to the metal surface (from H_2 evolution during the cathodic cycle) would render it inactive[71] and increase the required potential during electrograining. The measured potential would also increase if the pores within the smut contain an appreciable volume fraction of non-conducting gas, which would increase the resistance between the working and reference electrodes (Equation 2.44). In addition, an increase in the gas pressure, at the reaction plane, could result in a reaction overpotential (Equations 2.46 and 2.48); however, Equations 2.46 and 2.48 assume the gas is dissolved. Because gas nucleation is believed to occur at the metal interface, the concentration of dissolved gas is expected to be near saturation and approximately constant during electrograining. Thus, a temporal increase in Φ during electrograining is taken to be from the presence of interfacial bubbles and an increase in the smut resistance, which is due to the presence of a gas fraction in the smut. Because H_2 is immediately evolved at the onset of electrograining, Φ is expected to increase, at least initially, as gas is evolved. This initial increase is observed in all samples (Figures 5.11a, 5.11b, 5.11c and 5.11d), but is only sustained in some samples.

During electrograining, the measured potential shown in Figures 5.11a through 5.11d and Figure 5.12 can be described as either steadily increasing or not; the latter is associated with samples electrograined at 50 Hz in HCl and with citric acid and former with all other samples. Following the previous discussion, this increase is likely dominated by interfacial gas. Thus, the gas permeability of the smut is different in these two samples. The potential response in samples electrograined at 50 Hz in HCl and HCl+citric acid also correlates with higher gas retentions shown in Table 3. The final smut morphology for these two samples also contains fewer observable pores and shown in Figures 5.13a and 5.13c.

5.c.4.iii Gas Diffusion

Gas diffusion, after each electrograining burst, is characterized by t_m, which is inversly related to the gas diffusivity through the smut and shown in Figure 5.15 for each sample in Figures 5.11a through 5.11d. All samples electrograined at 100 Hz also have consistently lower values of t_m, indicating higher gas diffusivities compared to 50 Hz. This correlates with an observable increase in the smut porosity observed in the SEM images shown in Figures 5.13b, 5.13d, 5.13f and 5.13h and would facilitate gas diffusion in the absence of a pressure drop, consistent with lower values of t_m observed in all samples grained at 100 Hz in Figure 5.15. Differences in t_m between 50 Hz and 100 Hz are less pronounced with acetic acid and DPPD.

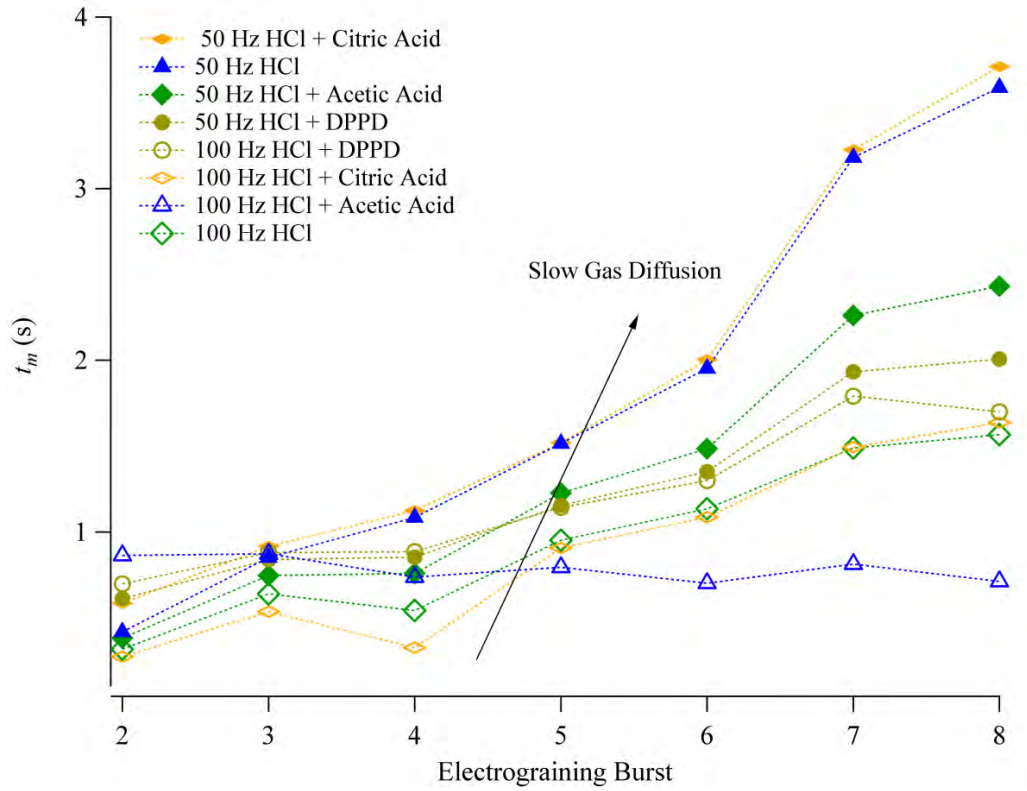

Figure 5.15 is a plot of t_m obtained from the fit of Equations 5.14 and 5.15 to the data shown in Figures 5.11a through 5.11d.

Gas diffusion is markedly slower at 50 Hz in HCl and HCl+citric acid, compared to all other samples. This is consistent with a different potential evolution during electrograining observed with these samples, whereby the potential increase is not sustained throughout the electrograining burst and shown in Figures 5.11a through 5.11d and more clearly in Figure 5.12. Markedly slower gas diffusion in these samples also correlates with the SEM images of the dried smut morphology (Figures 5.13a and 5.13c), which contain few observable holes compared to other samples.

5.c.5 Discussion

In this section, differences in the gas release, during and after electrograining, which correlate with differences in the potential response and dried smut morphology are discussed. First, the differences observed between 50 Hz and 100 Hz, in HCl only, are discussed. By considering the differences in the dried smut morphology, potential evolution and gas release, two general mechanisms for gas permeation are proposed in each case. These mechanisms are general in nature and provide an explanation for the experimental data. Using these two general mechanisms, experimental data obtained from other samples are explained as having a mixture of the two candidate mechanisms. Finally, the correlation between the different gas release mechanisms and final surface morphology are discussed.

5.c.5.i 50 Hz vs. 100 Hz in HCl

In the presence of HCl alone, higher gas diffusivities correlate with lower gas retention when the frequency is increased to 100 Hz. The increased porosity, observed in the final smut morphology, at 100 Hz, would be expected to facilitate gas diffusion after electrograining and thereby provides an explanation for the increase in gas diffusion observed at 100 Hz, as shown in Figure 5.15. On the other hand, very few holes are observed in the dried smut morphology, at 50 Hz, and results in slower gas diffusion. Thus, differences in the smut porosity, observed by SEM imaging of the dried smut morphology, provides an explanation for differences in the gas diffusion for the two samples.

The potential response, during electrograining, steadily increases at 100 Hz (Figure 5.11a), as the smut permeability is not high enough to maintain a constant potential gradient. At 50 Hz, the potential increases within the first second, but then remains approximately constant because the smut permeability is high enough to maintain a constant potential gradient.

Because similar amounts of H_2 gas are evolved at either frequency, it is concluded that the smut permeability is very different for these two samples, but this contradicts the gas diffusion results shown in Figure 5.15. To explain how smut formed at 100 Hz can have lower gas permeability and higher gas diffusion, factors that affect gas transport must be considered.

Once electrograining is initiated, the solution becomes supersaturated in H_2, gas and bubbles nucleate[74]. Traditionally, bubble nucleation is considered to occur at surface irregularities (i.e. pits) and grow in size until they reach a certain break-off diameter, at which time the bubbles detach[71] and permeate through the smut to the electrolyte. Assuming that the gas transport is restricted through micron sized pores, the pressure drop across the smut Δp would be proportional to the porosity, ϕ, and tortuosity, τ, by the relationship:

$$-\Delta p \propto \frac{(1-\phi)^2}{\phi^3}\tau^2 \quad (5.18)$$

$$\tau \equiv \frac{L_e}{L} \quad (5.19)$$

where L_e is the actual pore length and L is the smut thickness[28]. Considering that the pressure at the smut/electrolyte interface is the same for both frequencies, an increase in the partial pressure of hydrogen, p_{H_2}, is expected at 100 Hz if the gas transport is restricted to the tortuous pores only in Figure 5.13b.

On the other hand, the dried smut morphology obtain at 50 Hz has very few pores, indicating that gas transport does not occur through the same micron sized pores at 100 Hz. Instead, gas is expected to permeate through either smaller pores, or possibly through so called "water passage-ways[75]," that collapse after the electrograining burst, at 50 Hz. As these pores collapse, gas diffusion would be much slower, as the gel viscosity is much higher than the

electrolyte; slow gas diffusion would also result in a higher gas fraction retained in the smut. In fact, both slower gas diffusion and higher gas fractions are in Figure 5.15 and Table 3, respectively. Although gas diffusion is slower through these "collapsible" pores (50 Hz), gas permeation is much faster as opposed to gas permeation through possibly larger pores that do not collapse (100 Hz).

Unfortunately, the experimental results do not support any reason why gas permeates faster through collapsible pores. One possible explanation could be that the pores which collapse and reform have a lower tortuosity (Equation 5.19). This could be possible if, for example, the pores form by the gas at the beginning of each burst and takes the path of least resistance from the aluminium surface to the electrolyte. On the other hand when the pores do not collapse, new pores that form would not necessarily form directly underneath the previous pore path, which results in the tortuous pores observed by SEM (Figure 5.13b). It is also possible that more pores form in the smut electrograined at 50 Hz, which results in an increase in the porosity and decreases the pressure gradient across the smut (Equation 5.18). Of course, there is no direct experimental evidence to support the previous arguments because the smut porosity was not imaged *in-situ*.

It is currently unclear whether the pores observed in smut formed at 100 Hz are formed from the gas or because of the way the $Al(OH)_3$ is precipitated at a higher frequency. Regardless, the presence of gas flow through open pores, at 100 Hz, could partially dehydrate the adjacent $Al(OH)_3$ gel. Removal of water from the gel has been shown to also decrease gas permeation[75] and would force gas through the non-collapsible pores. Larger water content, in smut formed at 50 Hz is likely as the dried smut is much more uniform compared to that at 100 Hz. Thus, it is possible that the open pore gas permeation at 100 Hz further decreases the permeability of the gel itself, forcing evolved gas through open pores.

5.c.5.ii Effect of Additives (50 Hz)

Visible porosity, on the micron scale, is observed in the dried smut morphology at 50 Hz upon addition of all three additives (Figures 5.13a through 5.13h). The area fraction of holes increases according to the order: HCl only < citric acid < acetic acid < DPPD. A similar trend in t_m is observed in Figure 5.15 as gas diffusion increases according to the same order as the porosity, with values of t_m obtained with and without citric acid being very similar. Similar trends in the area fraction of holes and t_m, indicate that the non-collapsible pores promote gas diffusion. Because values of t_m for all samples are in between the HCl 50 Hz and 100 Hz samples, gas diffusion occurs through both collapsible and non-collapsible pores with the additives.

5.c.5.ii.1 Citric Acid

Addition of citric acid results in a smooth, continuous smut film, similar to HCl, as reported previously[36]. However, more holes are observed in the dried smut morphology, compared to HCl only. The micron sized holes observed with citric acid suggest that some of the gas permeates through the non-collapsible pores, which is consistent with less gas retention estimated by Equation 5.19 and shown in Table 3. Gas diffusion through the smut formed with citric acid is similar from HCl, as observed in Figure 5.15 and indicates that most of the gas permeates through collapsible pores.

During electrograining, Φ initially increases to a maximum with and without citric acid; this maximum is reached within the first second without citric acid and within the first few seconds with citric acid. The initial increase can be attributed to the increase in gas pressure, which stabilizes as Φ approaches a maximum value. After the maximum is reached, the potential decreases. The reason for this decrease is unclear, but could be due to expansion of

the pores that form at the onset of electrograining. This potential response is only observed with and without citric acid, at 50 Hz. Similar potential responses, with and without citric acid, suggest that the smut permeability is very similar in these two samples, consistent with similar gas diffusion shown in Figure 5.15 and similar gas retention (Table 3).

5.c.5.ii.2 Acetic Acid

From Figure 5.15, gas diffusion in smut formed with acetic acid is much faster than with HCl only at 50 Hz. Considering the presence of many small pores[36] in the dried smut morphology (Figure 5.13e), faster gas diffusion is expected with acetic acid at 50 Hz compared to HCl at 50 Hz. Unlike HCl only and HCl+citric acid, the measured potential steadily increases during electrograining to values much higher than other samples. This potential response is similar to that obtained at 100 Hz, in HCl, and suggests relatively low smut permeability. Compared to the HCl-100 Hz sample, higher potentials are observed with acetic acid and could be due to less porosity present in the latter, which would cause an increase in the interfacial gas pressure according to Equation 5.18.

Although gas permeation with acetic acid is very similar to that observed at 100 Hz in HCl, gas diffusion after each electrograining burst is slower and shown in Figure 5.15. Slower gas diffusion suggests that some of the evolved gas may permeate through collapsible pores. However, taking into account the relative smut masses, far less gas is retained in smut formed with acetic acid compared to other additives at 50 Hz and is closer to the gas retention calculated in HCl at 100 Hz. Therefore, gas permeation in smut formed in acetic acid is considered to occur through mainly the non-collapsible pores observed by SEM imaging (Figure 5.13e) and is very different with HCl only at 50 Hz.

5.c.5.ii.3 DPPD

Figures 5.13g and 5.13h show that very large pores on the order of 10 µm are present in the dried smut with the addition of DPPD. Gas diffusion is also much higher (Figure 5.15), which is consistent with rapid gas is release from the large pores after each electrograining burst. Less gas is also retained with DPPD compared to HCl at 50 Hz and was also reported previously[33]. The measured potential also steadily increases during electrograining, similar to acetic acid and HCl at 100 Hz. Based on the presence of large pores, high gas diffusion, low gas retention and an increasing potential response, smut formed with DPPD is considered to permeate gas through mainly non-collapsible pores, as with acetic acid and smut formed at 100 Hz in HCl only.

5.c.5.iii Effect of Frequency with Additives

Regardless of the additive used, an increase in the macro porosity is observed at 100 Hz (Figures 5.13c through 5.13h). An increase in the gas diffusion is also observed in Figure 5.15 at higher frequencies, as the presence of more pores facilitates gas diffusion after each electrograining burst. Although no gas retention calculations were made at 100 Hz with the additives, an increase in the porosity and gas diffusion indicate that gas permeation occurs through non-collapsible pores and likely results in little gas retention.

At 100 Hz, the increase in porosity observed with citric acid has a similar effect as that discussed with HCl only. In these samples, the measured potential is higher at 100 Hz because gas permeation occurs through more torturous pores and possibly fewer of them, according to Equations 5.18 and 5.19. In contrast, the sample electrograined with acetic acid, at 100 Hz, has a lower measured potential compared to 50 Hz. However, gas permeation is believed to occur primarily through small pores at 50 Hz. When the frequency is increased to

100 Hz, the presence of a larger area fraction of holes is observed (Figure 5.13f) and is expected to result in a lower gas pressure at the metal interface (Equation 5.18), resulting in a decrease in the measured potential. Finally, there is no difference in the gas retention or gas release in the samples electrograined in DPPD, within experimental error.

5.c.5.iv Gas Release Mechanism vs. surface morphology

In general two different gas release mechanisms have been proposed, where gas permeates through collapsible and non-collapsible pores. In HCl, at 50 Hz, gas permeates through either small pores or passageways that close after the electrograining is turned off; similar gas permeation is also shown in citric acid. Conversely, all other samples, having visible porosity in the smut and permeate and diffuse gas through pores that do not collapse after electrograining is turned off. Gas permeation through these larger and more torturous pores causes an increase in the interfacial gas pressure that result in a steady increase in the potential response during electrograining. In addition, gas permeation through open pores results in consistently low gas retention.

In all samples having observable porosity (Figures 5.13b through 5.13h), a uniform pit morphology is observed (Figures 5.14b through 5.14h). The HCl-50 Hz sample has a very different etch-like morphology that contains very few hemispherical pits. We propose that the difference between the HCl-50 Hz sample and all others lies in the difference in the gas permeation mechanism, which results in a lower potential response. This correlates well with previous work where higher overpotentials were associated with a uniform pit morphology.[29] Following previous work, the source of these high overpotentials can be attributed to the interfacial gas pressure and possibly more gas bubbles, which can influence the final surface morphology by changing the local dissolution kinetics[71]. However, the

exception to this model is with citric acid (50 Hz), where an etch-like morphology is not observed. This may be due to the presence of pores in the smut morphology, which may affect the local dissolution kinetics, compared to HCl only. All other surface morphologies (Figures 5.14b through 5.14h) have little difference between them. However, very deep pits are observed with the DPPD additive and could be due to aggressive attack through the large pores, which fill with electrolyte during the quiescent period.

5.c.6 Conclusions

1) *In-situ* SAXS measurements were performed while simultaneously measuring the electrode potentials. Analysis of the total scattering, *Q*, was used to measure trends in the gas retention and gas diffusion from the smut and correlate with different potential responses. Differences in gas retention and diffusion were observed at most all conditions and were determined to not be caused by differences in the size or local structure of the $Al(OH)_3$ agglomerates.

2) Smut formed in HCl only, at 50 Hz, had little visible porosity, which is consistent with SAXS measurements that indicate a gel permeation mechanism, whereby gas permeates through pores that collapse after electrograining. The principal characteristic for pores that reopen is a less torturous path for gas flow, which results in a lower potential response. After electrograining is stopped, the pores or passageways close, resulting in a low gas diffusion and high gas retention observed by SAXS measurements.

A change in the applied frequency from 50 Hz to 100 Hz, in HCl, resulted in gas permeation through open pores that do not collapse after electrograining is turned off. Unlike the pores that collapse and reform, these tortuous pores cannot permeate gas as fast and results in a potential response that steadily increases during electrograining. When the electrograining is

turned off, the pores do not collapse, which leads to faster gas diffusion through the smut, compared to the sample electrograined at 50 Hz in HCl; consequently, less gas is retained at 100 Hz.

3) Each additive resulted in an increase in the smut porosity, compared to the reference HCl only sample. Addition of citric acid resulted in a smooth smut morphology, similar to HCl, but with more porosity. Although, a gas permeation mechanism, similar to HCl only, was experimentally observed in the SAXS data, an increase in the smut porosity (and decrease in the retained gas) indicates that some gas permeates through non-collapsible pores and could explain the difference in the final pit morphology, compared to the reference HCl-50 Hz sample.

Addition of acetic acid resulted in more porosity than citric acid and the reference HCl-50 Hz sample, which correlated with little gas retention and high gas diffusion similar to the HCl-100 Hz sample. The resulting pit morphology was also shown to be very different to that obtained with the HCl-50 Hz sample.

The addition of DPPD resulted in a large amount of smut porosity with less gas retention and higher gas diffusion, compared to the reference HCl-50 Hz sample. The presence of these large pores, in the smut, correlate with a surface morphology that contained very deep pits that was vastly different from the reference HCl-50 Hz sample.

4) A change in frequency, in all electrolytes, resulted in an increase in the smut porosity, which resulted in faster gas diffusion; little frequency dependence was observed with the DPPD additive, with respect to the measured potential and gas diffusion. In all electrolytes electrograined at 100 Hz, the final surface morphology was very different from the HCl-50 Hz sample and is described as a uniform pit morphology containing hemispherical pits.

CHAPTER 6
Pitting Corrosion and Salt Films: Literature Review

Pitting corrosion is a particularly pernicious form of corrosion that dominates in many stainless steels. In general, pitting corrosion results in an occluded cavity that penetrates deep into the metal substrate. Pitting corrosion is a major concern for applications that use stainless steel as pressurized vessels and can result in exposure of the contained fluid to the atmosphere; this is undesirable if for example the contained fluid is crude oil or nuclear waste. Current knowledge about how pitting corrosion is initiated is used in many corrosion prevention programs (e.g. chloride concentration). On the other hand, a detailed knowledge of how a pit propagates, once it has formed, is very important in corrosion management programs, where pitting corrosion cannot be avoided. In particular, it is well known that certain pits will passivate early in their life, while others continue to propagate. This idea of pit stability has been well studied and even modelled and has been shown to depend on the concentration of dissolved species inside the pit, which maintain the dissolution kinetics[76].

One of the factors that have been shown to be crucial to the dissolution kinetics inside the pit is the presence of a salt film at the pit bottom, which maintains the aggressive solution chemistry required for metal dissolution[77-79]. The focus of this study is the composition of this salt film, towards a physical understanding of how the salt film forms and maintains the aggressive interfacial chemistry during pit propagation. Artificial pits are used to simulate the pitting process on a larger scale, which allow the study of salt films in a more controlled

and predictable manner. Additionally, nickel metal is used here, instead of stainless steel, to produce a thicker salt film.

6.a Pitting Corrosion

Pitting corrosion can be described in three steps: pit initiation, galvanic cell and pit propagation, as shown in Figure 6.1. A pit is initiated when the oxide layer is attacked until a void is formed (Figure 6.1). This attack typically involves the Cl^- ion and eventually results in exposing an actively-dissolving bare metal surface underneath the oxide layer.[80] Once the bare metal surface is exposed, a galvanic cell is formed because the electrochemical potential of electrons in the oxide layer and metal are different (Section 2.f.1).

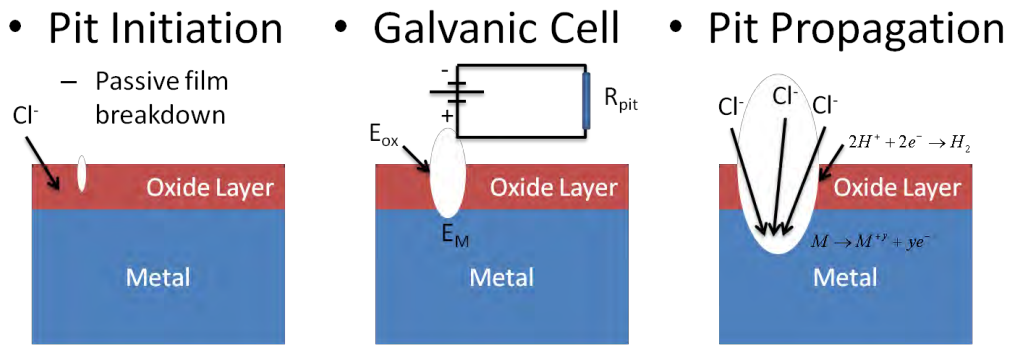

Figure 6.1 is simplified drawing showing three stages of pitting corrosion: pit initiation, galvanic cell (also called metal-stable stage) and pit propagation. The focus of this study is pit propagation, where the pit relies on aggressive solution chemistry

This potential difference causes the bare metal to continue to dissolve, shown in Figure 6.1; the solution resistance between the metal and oxide layer will also contribute to the potential drop. At this point, the pit can be considered meta-stable, as it can either passivate or continue to grow[76, 77]. Continued dissolution is aided by the influx of Cl^- to the pit bottom[81] to maintain electroneutrality, shown in Figure 6.1; in addition, the high concentration of dissolved metal cations, at the pit bottom, causes a decrease in the pH by hydrolysis, which also increases the dissolution kinetics[81]. The aggressive solution

chemistry at the reaction plane is maintained by restricted transport, out of the pit, by the presence of a partial "lacy cover," at the pit mouth and a precipitated salt film at the bottom of the pit.[77] By restricting transport away from the interface, salt films also play a significant role in the stability of corrosion pits by providing a "reservoir" of metal ions that can maintain an aggressive acidic solution chemistry near the interface even when there is a high rate of ion transport out of pits, for example after the rupture of a protective cover.[77, 78] Subsequent growth of the pit may then be controlled by ion transport through the salt film.[82] In addition to pitting corrosion, "brightening" and "levelling" are important properties of electropolished and electromachined processes that are known to be controlled by the presence of a salt film.[83] Thus, salt films play an important role in high rate dissolution processes and are the focus of this study, toward an understanding of how salt films form and how transport occurs through the film at steady state.

6.b Artificial Pits

Artificial pits simulate pit propagation on a larger scale, by applying a potential difference between the working and counter electrode, similar to what is present between the oxide layer and bare metal in a real pit (Figure 6.1). Similar to a real pit, ionic transport is restricted by the 1-D geometry in an artificial pit (Figure 3.5), which results in the precipitation of a salt film[38]. Artificial pit cells generally have two designs: a metal foil, embedded in epoxy or a thin wire encapsulated in a glass tube. In either case, the metal is dissolved down to a desired pit depth, typically on the millimetre scale. Transport in these systems can be considered one dimensional throughout the pit, until the pit mouth where the cross-sectional area (and transport) is increased. To a first approximation, the conditions at the pit mouth can be considered to be the bulk concentration values because of the drastic increase in area at the

pit mouth[27]; this assumption is based on the fact that transport at the pit mouth is much faster than in the pit because the transport goes from 1-D to 3-D.

When the pit reaches a critical depth, ionic transport is restricted enough to cause a salt film to precipitate. Continued dissolution occurs at a limiting current density over a wide potential range in nickel and stainless steel artificial pits and has been attributed to the presence of this salt film[27, 82]. Although the limiting current is not a function of potential, it does decrease with increasing pit depth.[27]

6.c Salt Film Formation

When the pit is deep enough, a salt film forms at higher anodic potentials (*ca* >300mV *vs.* Ag/AgCl in nickel pits). In the presence of the salt film the total overpotential is a combination of the reaction overpotential (Equation 2.46) and the IR drop across the salt film, pit and bulk solution[27, 82, 84, 85]; this region is commonly referred to as the diffusion-controlled region[27, 84]. At lower potentials, the salt film dissolves and the IR drop across the salt film vanishes and the system is said to be in the active dissolution region[27, 82, 84, 85]. Formation of a salt film is accomplished by simply increasing the applied potential by either a potential step[27, 84] or potential sweep[77, 78] to anodic potentials. A potential increase results in an increase in the flux of dissolved metal with the current by Equation 2.46. As the concentration of dissolved metal increases, the mobility and diffusion coefficient of these ions also decreases[18], restricting ionic transport near the interface. At this point, the near interface concentration reaches supersaturation[85]. Based on numerical transport modelling, supersaturation ratios greater than one are reached[85], before precipitation of a porous crystalline[38] "salt film"[86].

6.c.1 Supersaturation and Crystal Nucleation

The idea of supersaturation and crystal nucleation is well established in crystal nucleation theory.[87] In artificial pits, the exact supersaturation, prior to nucleation, is not well defined or experimentally accessible. Crystal nucleation theory predicts supersaturation ratios, $\left({}^{C}/_{C_{sat}}\right)$, greater than 2[88], while transport modelling calculations have obtained lower values[84, 85]. Kinetic crystal nucleation theory calculates the supersaturation ratio by considering the monomer-monomer, monomer-solvent interaction and the crystal structure.[89] Although this model has been applied to many simple structures[89] (i.e. FCC), it has not been applied to any of the metal salt systems studied here.

Alternatively, one could calculate the supersaturation ratio by solving Equations 2.49 and 2.50, with the appropriate boundary conditions, for example:

(6.1) $C_i = C_i^{\infty}$

(6.2) $\Phi = 0$

} Pit mouth

(6.3) $J_{M^{+n}} = \frac{i}{nF}$

(6.4) $J_j = 0$

(6.5) $\frac{d\Phi}{dx} = \frac{i}{\kappa}$

} Pit bottom

where the conditions at the pit mouth are taken to be the bulk values and the current is used for the metal flux and potential gradient, at the interface. Of course, the Nernst-Plank-Poisson equations, with these boundary conditions, assume that the system is dilute and neglect short range interactions[23], relaxation[24, 25] and electrophoretic effects[24] that are

expected at concentrations greater than about 2 M; saturation of metal chlorides are typically around 4 M[20] and decreases with the pH. The boundary conditions used for the species flux, at the pit bottom, are exact and experimentally accessible. However, the boundary condition, at the pit bottom, for the potential, Φ, assumes no concentration gradient exists there and is an extension of Ohm's law[90].

This general modelling approach has been used fruitfully in pitting corrosion and other electrochemical systems. Real pits have been successfully modelled with this approach[79], which predicted pit growth behaviour, observed experimentally.[79] In that particular study, salt film precipitation was accounted for by a semi-empirical equation that related the change in salt concentration with time to the supersaturation ratio which was not allowed to exceed 1.1.[79] Supersaturation ratios can also be estimated in artificial pits where the metal foil is potentiostatically stepped to a sufficiently high anodic potential. A simple estimation of the supersaturation has been performed by assuming negligible migration and unrestricted diffusion at the metal interface. The resulting current response, shortly after the Potentiostatic set, should decrease proportional to $t^{-1/2}$ and has been experimentally observed in the initial current response in nickel[27] and iron[91] systems. Assuming the mutual diffusion constant of metal chloride is constant, the supersaturation ratio has been estimated to between 1.8 and 2.6 in an iron artificial pit.[91] Similar arguments have also been made in artificial pits that result in similar supersaturation ratios.[84, 92] By neglecting concentration effects, interfacial metal concentrations greater than saturation have been previously calculated, consistent with crystal nucleation theory that also predicts supersaturation conditions prior to crystal nucleation. However, supersaturation ratios estimated from the current density assume dilute transport, which is clearly not the case and neglect concentration effects discussed in Section 2.f.3.ii.

6.d Steady State Salt Films

Once a salt film has precipitated, the current decreases to a minimum, at which point the salt film is believed to reach a maximum thickness.[27, 84, 91] The current then increases to the steady state limiting value, as the salt film is believed to dissolve back to a smaller, steady state thickness.[27, 84, 91] One of the most important characteristics of a precipitated salt film is its thickness, as this will affect transport through it (effectively, the resistance), which ultimately is responsible for the limiting current density. Salt film thicknesses have been calculated using electrochemical methods and are generally considered to increase with increasing potential in both iron[82, 93] and nickel[27, 38, 82, 94] systems; the thickness of salt films calculated are on the micron scale. The principal assumption made in all of these approaches[27, 93, 95] is that no concentration gradient exists inside the film, as the concentration is considered to be at saturation; most often, it is assumed that there is a bulk salt film that is uniformly composed of salt and saturated metal chloride solution[27, 79, 82, 94, 96].

Although the salt film thickness does change with potential[27, 38, 82, 93, 94], it has not been proven that the entire potential drop is accommodated by the presence of salt (porosity or thickness) and it could also be a consequence of the presence of high ionic concentrations, which would also decrease ion mobility significantly[23]. Thus, it is unclear whether ion transport of dissolved metal chloride is restricted by the presence of salt or by its own mobility.

Previous work has focused on the electrochemical properties of salt films[27, 82, 93-96], but there has been very little work on their structural and chemical characterization apart from some X-ray diffraction[38] and Raman spectroscopy[94] owing to the difficulty of carrying out in situ

measurements on rapidly dissolving surfaces. To a first approximation, the composition of the salt film would be related to the concentration profile of dissolved $NiCl_2$ through the equilibrium constant, which assumes that crystal growth and dissolution are much faster than the ion transport. Thus, with information about the salt composition, the concentration profiles (and thus the transport) can be characterized. Fundamental understanding of the transport in such concentrated environments is important in the design process of many electrochemical processes as well as in corrosion prevention.

6.d.1 Steady State Transport

There has been some work involving transport modelling to predict concentration gradients inside the film[97, 98], but this is difficult to verify experimentally. The application of transport theories[18] that neglect short range interactions[23] and other concentration effects[24, 25] have successfully explained many phenomena of pitting in both artificial pits[78, 98] and real pits[79]. Most often, diffusion is assumed to be the dominant transport mechanism near the interface and even throughout the entire pit.[84] This assumption requires a negligible potential gradient (migration term in Equation 2.49) through the salt film, even though it is generally accepted that salt film accommodates most of the potential drop in the pit[27, 82, 84, 85, 91, 94, 96, 98] Electrochemical impedance spectroscopy measurements have deduced a capacitive component[93, 94], within artificial pits, which implies the presence of a large electric field. This was explained as a non-porous layer that exists between the dissolving metal and salt film.[93, 94] Thus, there appears to be uncertainty in the mechanism of transport across the salt film.

The presence of a non-conducting salt film results in a resistance, as ions can only transport between salt crystals. Salt film resistivity has been calculated for stainless steel[82], iron[93]

and nickel[27, 82] systems and can be related to the porosity[26], with few assumptions. Previous authors have assumed that saturation conditions exist inside the salt film regardless of the applied potential.[27, 93] The source of this assumption is that the salt film is a homogenous film that maintains saturation conditions through the equilibrium constant.[27, 93] Using Raman spectroscopy, it has also been shown that the speciation in nickel salt films is $Ni(H_2O)_6^{2+}$, [94] indicating no Cl^- ligands in the nickel complex, which may be expected at higher concentrations[23]. Using the resistivity of the salt films, their porosity, ϕ, has been estimated to be ca 0.001 in nickel artificial pits.[27] However, from Equations 2.55 and 2.56 the tortuosity can also influence transport through the film. Tortuosity can be expected in salt films but difficult to quantify, as the salt crystals move freely in response to ion transport and Brownian motion during dissolution. Thus, a physical characterization of the salt film would provide insight into its porosity and ion transport within the salt film.

6.e Motivation of Current Research

The motivation of this study is to provide experimental data that can be used for future transport modelling in systems such as pitting corrosion where high dissolution rates occur in highly concentrated solutions. Artificial pits, used in this study, are a unique and challenging case where transport can be restricted by concentration effects and the presence of a precipitated salt film near the interface. As opposed to traditional methods used to relate physical properties of the salt film to its electrochemical properties, the aim of this study is measure the physical properties near the interface by using synchrotron techniques. To our knowledge, there has been no work to directly characterize the supersaturated solutions adjacent to dissolving interfaces from which salt films precipitate. The nature of these near interface solutions are not only important to corrosion, electropolishing and

electromachining, but are also likely to influence other electrochemical processes such as those in batteries.[99]

Nickel artificial pits are used in this study because they tend to form thicker salt films and because of the difference in attenuation between the metal and adjacent solution. Time resolved small angle X-ray scattering (SAXS) and X-ray diffraction (XRD) are used here to observe scattering populations and crystalline material at the interface, respectively. A scattering population is defined as any population, on the nanometre scale, which has an electron density different than that of the surrounding matrix[3]. Details of the SAXS methodology and theory are discussed in the following Chapter.

CHAPTER 7
Salt Film Formation in Artificial Pits

Artificial pits, maintained at high anodic potentials, are high rate dissolution systems that are most frequently used to simulate pit propagation; however, their study is also relevant to other applications such as electropolishing. As discussed in the previous chapter, salt films form as a result of high rate dissolution and restricted transport. These salt films limit the transport and maintain the aggressive solution chemistry at the pit bottom. The presence of salt films is especially important for a pit to continue to grow[78]. In this Chapter, experiments are described whereby salt film formation was simulated by a potential step to understand salt film formation, which could be important if for example salt film formation could be prevented all together. In these experiments, the structural changes observed in the salt film are correlated to changes in the measured current. In all of the experiments reported here, nickel artificial pits were used, which were grown to pit depths between 1 mm and 2 mm before the synchrotron experiments were performed. The same cell design was used in all experiments and shown in Figure 3.5

7.a Salt Film Formation

A potential step, when used to simulate salt film formation, is a very simple technique where the potential of the working electrode is increased within a second and maintained for at least 300 s. In a typical experiment, X-ray and electrochemical data collection are synchronized by recording the X-ray frame number and electrochemical time. This synchronization is essential in the analysis, as conditions near the interface change during a potential step and correlate with the current *vs.* time behaviour. Because the metal dissolved continuously during the potential step experiment, the sample was periodically moved up to maintain the metal interface in the centre of the beam; typical X-ray beam heights were between 70 um and 300 um, which made it possible to maintain the interface in the beam manually.

Figure 7.1 shows a typical time-resolved X-ray diffraction experiment at Station 6.2, SRS Daresbury, where XRD data was collected with the current response. In this experiment, data collected over 30 s gave a sufficiently high signal to noise ratio to allow a Voigt function to be fitted to peaks corresponding to $NiCl_2(H_2O)_6$. The peak positions correspond well to $NiCl_2(H_2O)_6$ reported[100, 101] and closest to those reported by Crook[100]. Approximately 60 s after potential steps from 0 V to between 1.2 V and 2.0 V, faint diffraction peaks can be observed; all potential step experiments were performed to potentials in this range. After 100 s, the current begins to decrease rapidly and undergoes a minimum at about 200 s. At the same time, the diffraction peaks became noticeably stronger, indicating the presence of more salt near the interface during this time. Results obtained from these initial salt film formation experiments showed that the diffraction patterns and current both change after a potential step, which inspired later experiments and further analysis.

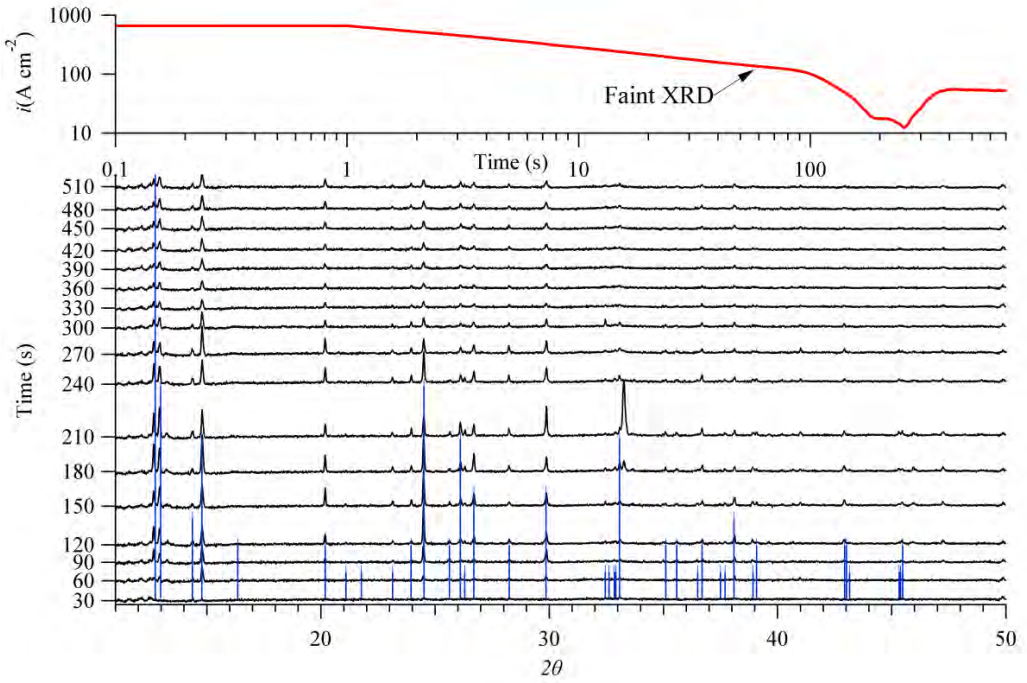

Figure 7.1 is a typical potential step experiment to 1.6V (*vs.* Ag/AgCl) performed on the entire salt film at MPW 6.2 Daresbury.

7.a.1 SAXS/WAXS

Using a similar protocol to that used for the experiment shown in Figure 7.1, potential step experiments were performed whilst collecting small angle X-ray scattering (SAXS), wide angle X-ray scattering (WAXS) and electrochemical data; SAXS/WAXS experiments were carried out on beamline I22 at the Diamond Light Source. Data collected from these experiments was processed as described in Section 3.b.2.iii.

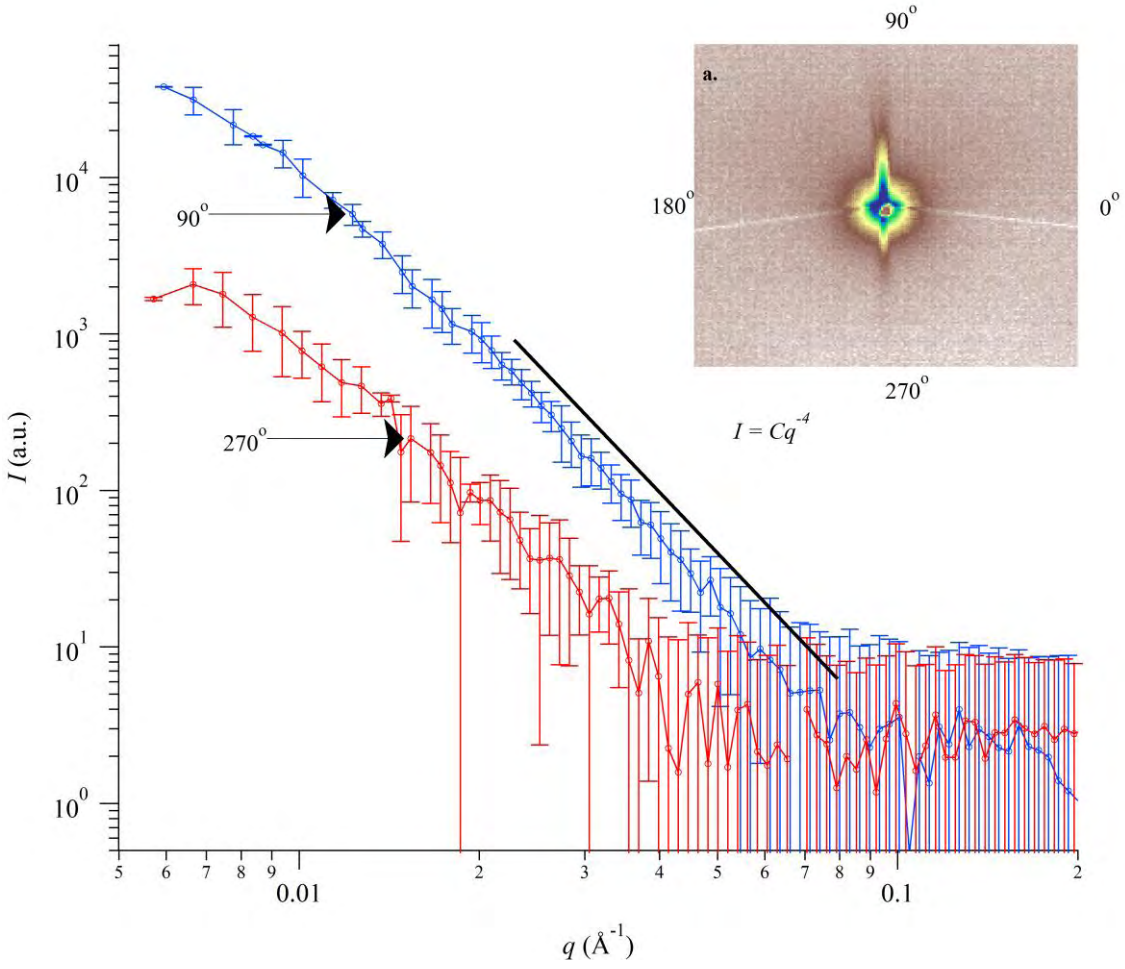

Figure 7.2a is a typical SAXS image obtained 60 s after the Potentiostatic step to 1.4V. Figure 7.2b is a log-log plot of typical anisotropic SAXS obtained from sector integration at 90° and 270° from the image shown in Figure 7.2.

Approximately 10 s after the potential step, anisotropic small angle scattering was observed, which increases to a maximum at approximately 60 s. Figure 7.2a shows a raw SAXS image at 60 s showing a strong signal at 90° and 270°. Figure 7.2b shows the resulting 1-D SAXS data averaged over 10° sectors at 90° and 270°. The shapes of the SAXS profiles are similar for both sectors, having power-law decays in intensity greater than q^{-4} and approaching q^{-5}. The shapes and temporal behaviour of both of these scattering curves are essentially the same (apart from their magnitude) up to 120 s. Since the scattering signal at 270° is smaller than that at 90°, scattering must arise from an oriented anisotropic population near the interface,

with a small dimension perpendicular to the metal foil; the SAXS data obtained from the 10° sector at 90^o is analyzed here because the signal-to-noise is lower at 270^o. Furthermore, no scattering is observed at the 0^o and 180^o sectors, which leads to the conclusion that the scattering population must have very large dimensions (>1 μm) parallel to the metal surface.

7.a.1.i SAXS Modelling

Small angle scattering requires a difference in electron density between the scattering and matrix phase.[3] Given that a positive current is always maintained in these experiments, the interfacial objects that fulfil this requirement are considered to be: concentrated $NiCl_2$ solution, a passive NiO layer and solid salt crystals. Anisotropic scattering is not likely to be from solid particles near the interface, as they would be suspended in a convective solution and likely to change orientation and move from the interface.

Anodic nickel oxide films are commonly grown in different alkaline conditions[102]. Based on steady state transport calculations, the H^+ concentration at the metal interface was found to be an order of magnitude less than bulk concentration[97, 98] (1 M). Due to the low interfacial pH (~1), the formation of such a film is unlikely. Taking the pH into account, formation of NiO_2 is thermodynamically possible for a potential step to 1.8 V[102], but would be kinetically limited by the low water activity, as the concentration of Ni(II)Cl is predicted to be very high near the interface[97, 98]. Thus, the formation of a passive layer is considered to be unlikely in these conditions. The anisotropic scattering is therefore considered to be from a population of layers, containing a high concentration of Ni(II) on the surface of the metal. Because the metal foil does not dissolve uniformly, the scattering can be assumed to be from a population of non-interfering slab-like layers or a single uniform slab-like layer that spans across the entire surface; in the *q*-range observed here, there would be little difference in the SAXS data

between a single uniform slab-like layer and a population of randomly distributed slab-like layers because only the smallest dimension is observed. Thus, the term "surface layer" is used for the remainder of this paper, whilst recognising that this could also be a population of non-interfering layers.

Scattering from a slab can be treated as a simple box by the equation:

$$(7.1)\ I_{id}(q) = k\int_{cos\,90}^{sin\,\omega}\int_{cos\,90}^{sin\,\varphi}\left\{\frac{sin\,(qZ\alpha)}{qZ\alpha}\frac{sin\left(qY\sqrt{1-\alpha^2}\,sin\left(\frac{\pi}{2}\beta\right)\right)}{qY\sqrt{1-\alpha^2}\,sin\left(\frac{\pi}{2}\beta\right)}\frac{sin\left(qX\sqrt{1-\alpha^2}\,cos\left(\frac{\pi}{2}\beta\right)\right)}{qX\sqrt{1-\alpha^2}\,cos\left(\frac{\pi}{2}\beta\right)}\right\}^2 d\beta\,d\alpha$$

where, k, is a constant, ω, φ, are the angles parallel and perpendicular to the incoming X-rays, respectively, Z,Y and X are the lengths, defined in Figure 7.3.

A power-law decay in q can be observed in anisotropic small angle scattering, at high q, as discussed in Chapter 2. However, the power-law decay in q can deviate from q^{-4}, observed for isotropic scattering, depending on the values of φ and ω. The value of φ, in Equation 7.1 was restricted to 5^o because most of the scattering signal was confined to the 10^o sector. An estimation of ω is, however, more difficult because this angle is parallel to the beam propagation.

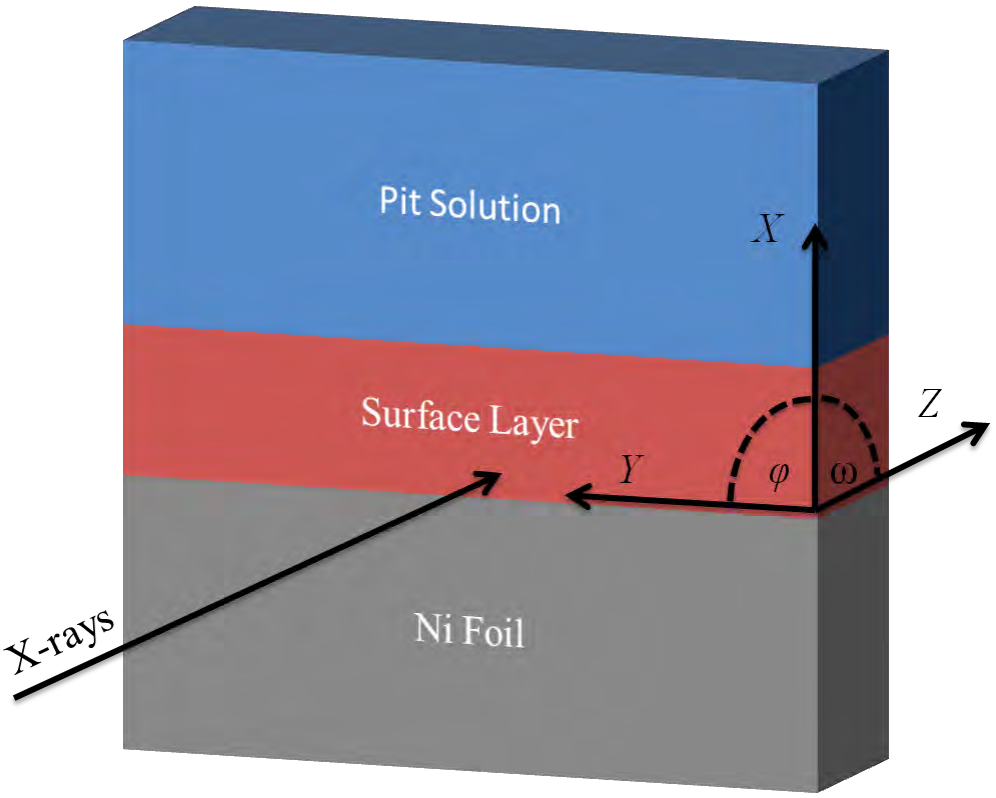

Figure 7.3 is drawing showing how the surface layer is modelled with Equation 7.1.

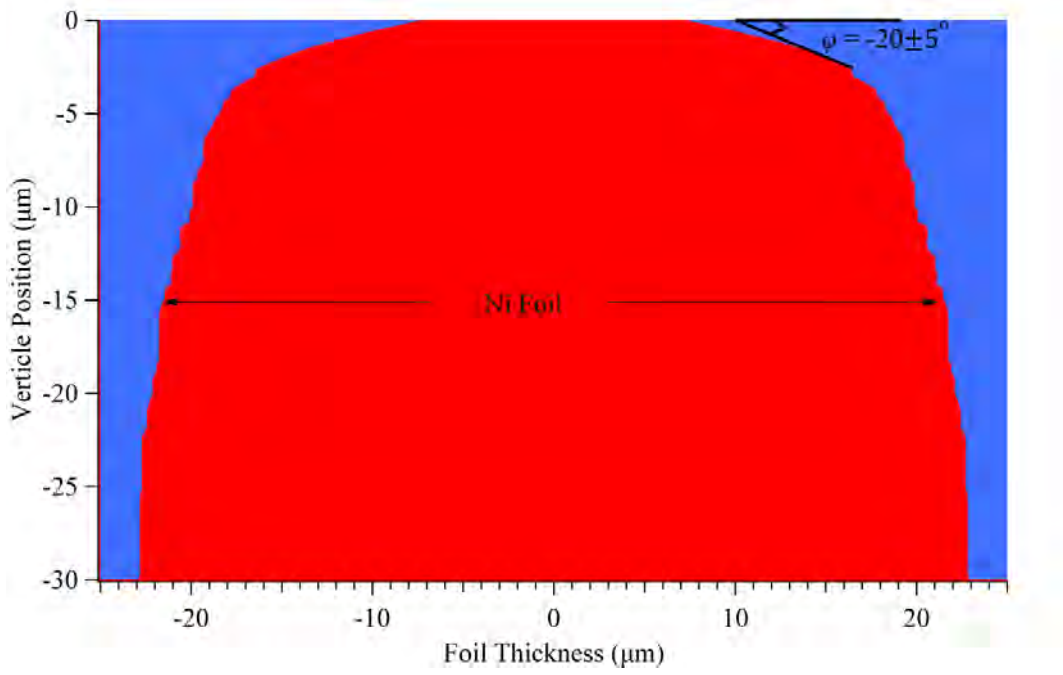

Figure 7.4 is the through thickness of the Nickel foil (*Z* direction in Figure 7.3) calculated from a radiography image, 60 s after a potential step to 1.6V.

Realizing that the mass absorption of nickel is an order of magnitude greater than that of nickel chloride salt, the through thickness of the metal foil (into the page in Figure 3.6a) is readily calculated from radiography data by the equation:

$$t = \frac{\ln\left(I_o(x)/I_t(x)\right)}{\left(\mu/\rho\right)_{Ni}\rho_{Ni}} \quad (7.2)$$

where $\left(\mu/\rho\right)_{Ni}$ is the mass absorption coefficient of nickel metal (69.65 $cm^2\ g^{-1}$) and $\rho_{m_{Ni}}$ is the mass density of nickel metal (8.91 g cm^{-3}). The thickness was calculated after taking an average vertical profile along the entire horizontal range (Figure 3.6a), in a manner similar to how the absorption profile, $A(x)$ was calculated. The nickel foil through thickness is shown in Figure 7.4, 60 s after a potential step to 1.6 V. The curvature of the metal foil, at the interface, is less than $20^o \pm 5^o$ for most of the metal thickness and increases rapidly to 90 ^{o} near the edge of the foil; error in this estimation arises from analysis of all images after the step and for two different steps to 1.6 V and 1.0 V. The value of ω is therefore taken to be 20 ^{o} in Equation 7.1, as estimated from analysis of the radiography data.

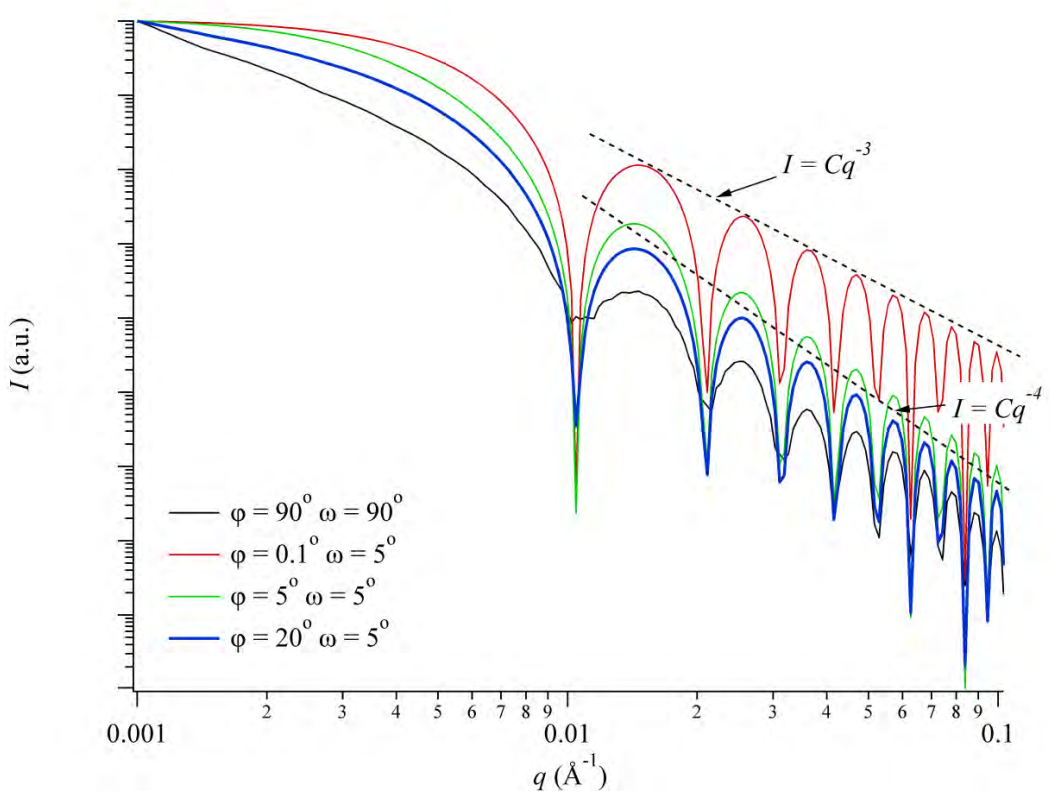

Figure 7.5 is a sensitivity plot showing how the theoretical intensity decays, at high q, with different values of phi. All curves are calculated from Equation 7.1, with the dimensions of *Y* and *Z* on the micron scale.

The estimate of ω, obtained from the radiography data, contains a relatively large error. The scattered intensity, at high q, is expected to decay according to q^{-2} for a perfectly oriented layer and q^{-4} for an isotropic layer taking on all possible orientations. From Figure 7.5, the intensity decays at high q according to q^{-4} for values of φ greater than 5. Therefore, taking into account the error in ω, the scattered intensity from the surface layer is expected to decay according to q^{-4} at high q.

Given the values of φ and ω, the scattered intensity calculated from Equation 7.1 should decay according to q^{-4}, similar to an isotropic surface layer. Negative deviations from high q scaling have been attributed to the presence of a smooth electron density gradient between the scattering and matrix phase[12]. These smooth transitions can be obtained numerically by convoluting an ideal (piece-wise function) electron density distribution by a smoothing

function, commonly assumed to be a Gaussian[11, 12]. Using the convolution theorem for Fourier transforms, the scattered intensity can then modeled by the equations:

(7.2) $I(q) = I_{id}(q, X)H^2 + [Fl]$

(7.3) $H = e^{-(\sigma^2 q^2)}$

(7.4) $[Fl] = \frac{k}{q}$

where H is the Fourier transform of the smoothing function, σ is the standard deviation of the Gaussian smoothing function, $[Fl]$ is the background due to density fluctuations and k is a constant.[11, 12] Equation 7.2 accounts for smooth transitions between phases and is applied to the high-q portion of the scattering data. The background term, $[Fl]$ is assumed to be dominated by two dimensional density fluctuations at the layer boundary[12]. Two dimensional fluctuations are assumed, because the layer boundary itself is not perfectly one-dimensional and because Equation 7.4 resulted in a better fit, compared to a constant or one-dimensional background.

Modeling the intensity data, using Equations 7.1 - 7.4, cannot be performed with any confidence because of the oscillatory nature of Equation 7.1. These oscillations are unrealistic because of surface roughness and consequent polydispersity in slab thickness, which cause deviations from a perfect parallelepiped SAXS model[3]. Instead, a simple equation that takes into account the ideal intensity decay in q of q^{-4} was fitted to the high q-region (0.03 Å < q < 0.075 Å). The resulting equation is:

(7.5) $I(q) - [Fl] = \frac{k}{q^4} e^{(-\sigma^2 q^2)}$

where $[Fl]$ is obtained by fitting a power-law function in the q-range, 0.08 Å^{-1}< q <0.2 Å^{-1} to Equation 6. Figure 7.6 is a plot of the background subtracted intensity *vs.* q, obtained 60 s and 90 s after the potential step with the respective fitted curves obtained from Equation 7.5. All other data showed similar fits, but the SAXS data collected before 20 s and after 120 s had very poor fits, owing to the low signal to noise. The dashed lines in Figure 7.6 show how the background subtracted intensity deviates from the ideal q^{-4} decay, which is attributed to the presence of an electron density gradient at the layer boundary. Error bars are not shown in Figure 7.6 for clarity. In general the fitted data are on the edge of the experimental error calculated from the standard deviation as discussed in Chapter 3.

Using the background-subtracted intensity from two steps to 1.4 V and two steps to 1.8 V, the values of k and σ were varied to fit Equation 7.5 by a least squares method. The FWHM of the Gaussian smoothing function is calculated from σ and used to represent trends in the transition layer thickness, Δ and is calculated from σ by the standard equation:

(7.6) $$\Delta = 2\sqrt{2\ln(2)}\sigma$$

Values of Δ reported here are on the order of 1 nm, with the entire transition region being much larger. Errors in Δ are obtained from the standard deviation of the fit calculated by the "*FitFunc*" function in Igor Pro.

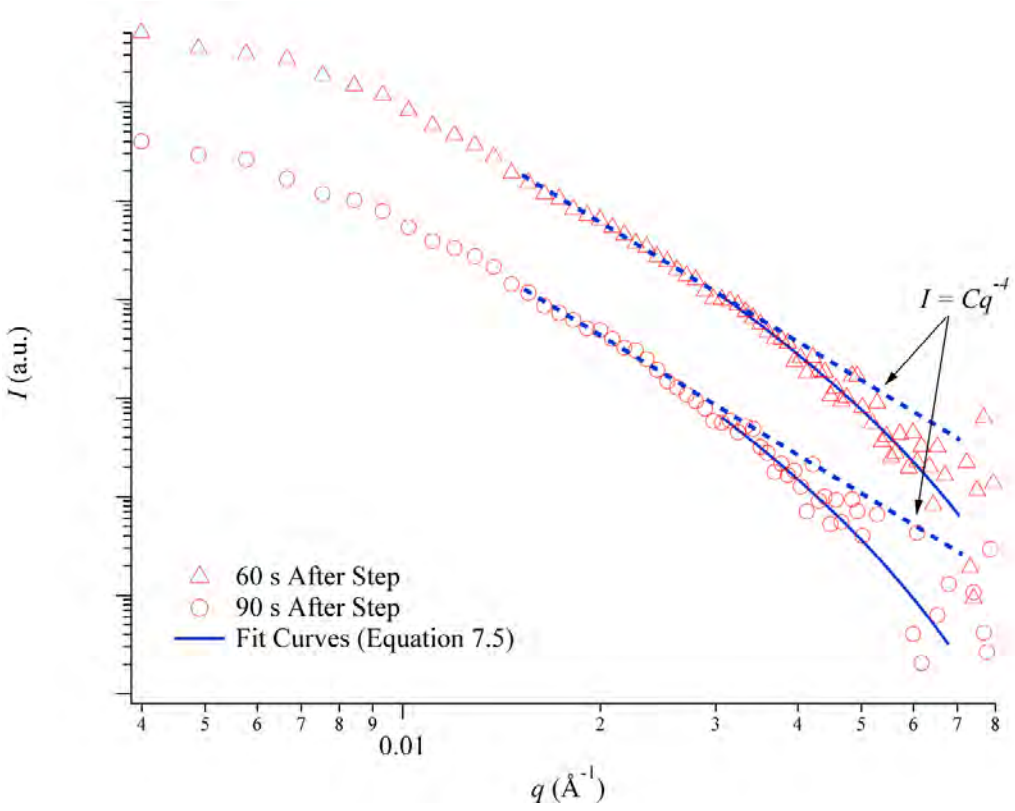

Figure 7.6 is a log-log plot of the scattered intensity *vs*. *q* 60 s and 90 s after a Potentiostatic step to 1.4 V. The solid blue lines are the curves resulting from fitting Equation 7.5 to the data, by a least squares method. The dashed lines are power law decays in *q* of *q*-4 and show how the raw data deviate from this ideal behaviour.

7.a.1.ii Time dependence of total scattering

A pseudo-invariant was devised to represent the total scattering, because the scattering is anisotropic and given by the equation:

$$(7.7) \quad Q_{\varphi} = \int_{0.005}^{0.05} \int_{85}^{95} I(q) q^2 d\varphi dq \cong \frac{\pi}{18} \int_{0.005}^{0.05} I(q) q^2 dq \propto \overline{\eta^2} V$$

where q is the magnitude of the scattering vector, I is the averaged intensity over the 10^o span, V is the volume of the surface layer and $\overline{\eta^2}$ is the contrast; integration limits are set to the available q-range. Equation 7.7 is used as the best available equation for the total scattering of the anisotropic scattering population. The total scattering is proportional to the total scattering volume and contrast, which are the physically meaningful parameters that

change Q_φ. Errors in Q_φ are calculated from the errors calculated from the standard deviation in the azmuthal image integration shown in Figure 7.2a.

7.a.1.iii Total Salt Volume

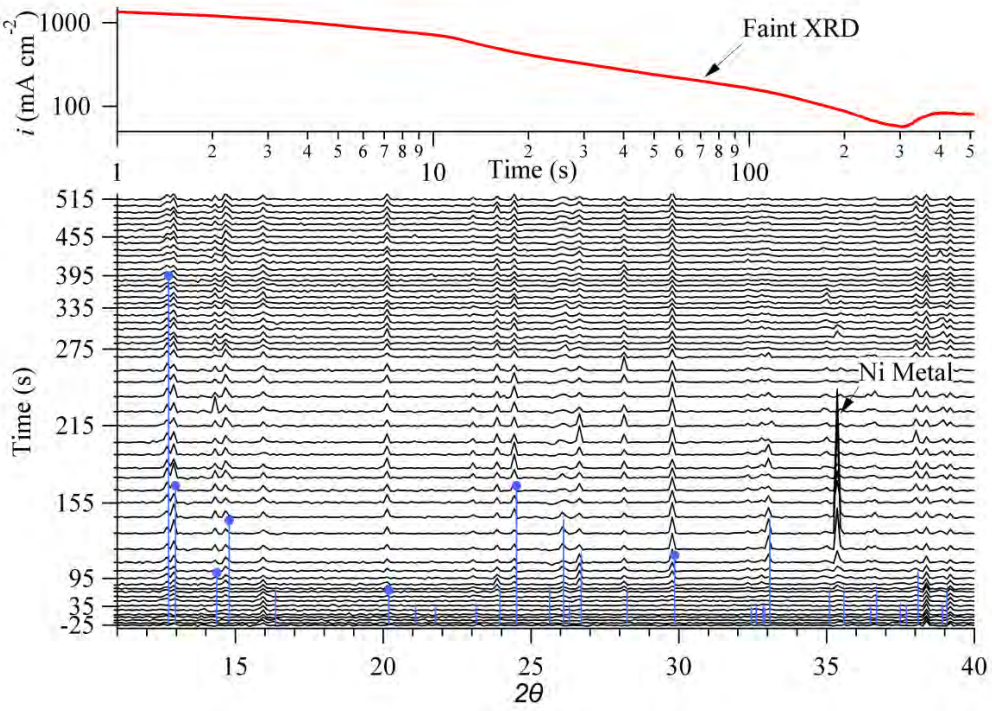

Figure 7.7 is a stack plot showing the diffraction patterns and electrochemical data collected simultaneous with the SAXS images. The peak at 35.5 corresponds to Ni metal. The blue sticks correspond to $NiCl_2(H_2O)_6$ reported by Crook[100].

Figure 7.7 shows the diffraction patterns collected simultaneously with the SAXS images. Faint diffraction peaks, corresponding to $NiCl_2(H_2O)_6$, are observed at *ca* 70 s, similar to that observed in Figure 7.1. Although a higher (10 s) time resolution was obtained at I22, the 2θ resolution was not as good as that obtained at Daresbury (Figure 7.1); most peaks are triangles in Figure 7.7, unlike Figure 7.1 where observed peaks have a proper Voigt shape. Because most peaks contain only three points, a Voigt function could not be fitted to any of the peaks.

A simple estimate of the total volume of crystalline salt present (V_c) is obtained by numerical integration of the area under seven diffraction peaks (from patterns of the type shown in Figure 7.7) minus backgrounds calculated by straight line interpolation from neighbouring regions free of diffraction peaks. Errors in the observed salt volume were taken as the standard deviation (counting statistics).

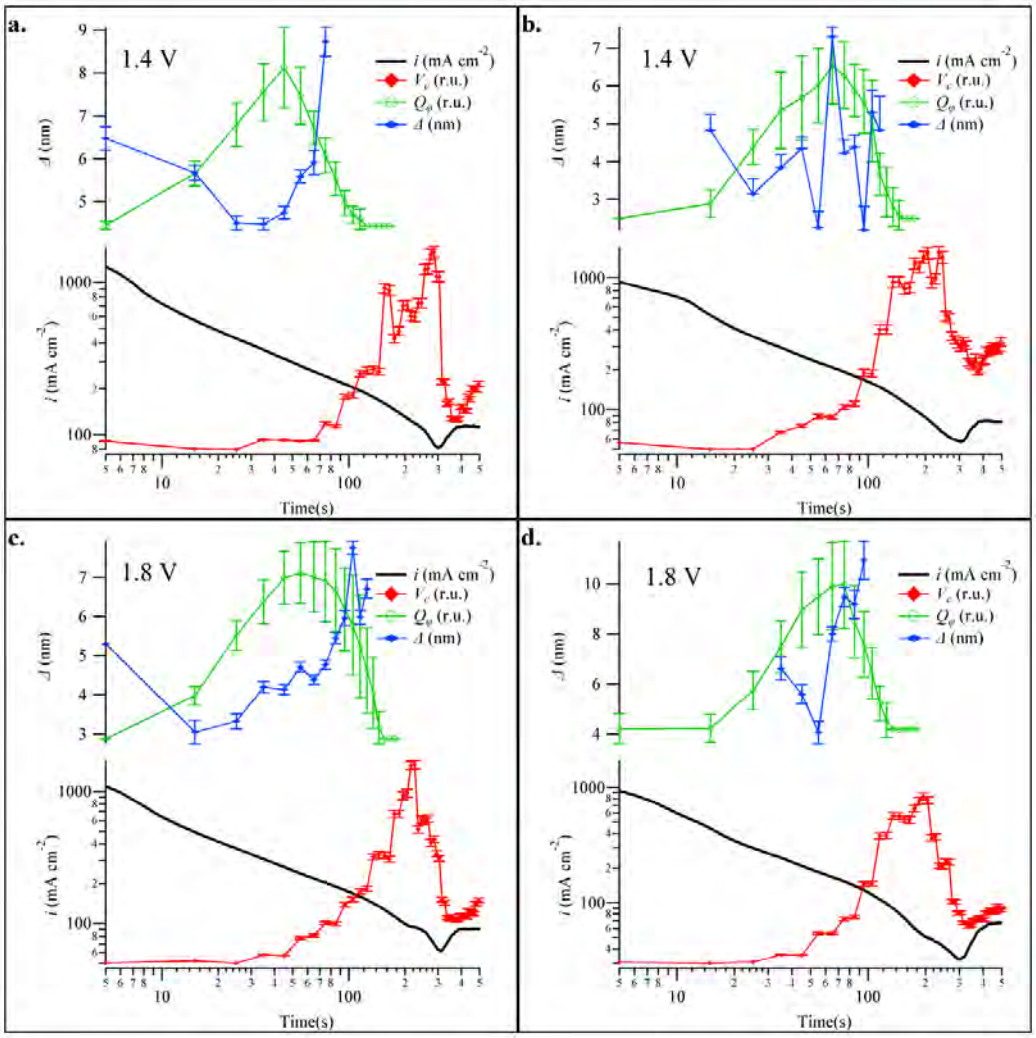

Figure 7.8a, 7.8b, 7.8c and 7.8d are plots the SAXS total scattering (Q_φ), crystalline salt volume (V_c), transition layer thickness (Δ) and the current density (i) after Potentiostatic steps to 1.4 V, 1.4 V, 1.8 V and 1.8 V, respectively.

Figure 7.8a shows a plot of the way that the SAXS total scattering (Q_φ), crystalline salt volume (V_c), transition layer thickness (Δ) and the current density (i) change with time, following the application of a potential step to 1.4 V. In all experiments shown in Figures

7.8a through 7.8d, Q_φ increases to a maximum at *ca.* 60 s at which time the surface layer has a small transition layer thickness, Δ, (sharp interface) except for the experiment shown in Figure 7.8b, where no trend in Δ can be observed. Before the maximum Q_φ value is reached, the value of Q_φ increases by a factor of three, with little change in the scattering shape within experimental error. Values of Δ and salt volume (V_c) always increase rapidly after Q_φ reaches a maximum, showing a strong correlation between the three parameters. After the SAXS signal from the surface layer goes to zero ($Q_\varphi = 0$), V_c reaches a maximum before the current minimum and decreases to a steady state value as the current density increases to the steady state limiting current density.

7.a.2 XRD only

X-ray diffraction data collected from the first experiments at Daresbury, shown in Figure 7.1, were also analyzed to obtain the change in peak shape with time. A Voigt function was fitted to two of the strongest peaks at 12.8^o and 14.9^o (Figure 7.1), which correspond to the {1,1,0} and {-1,1,1} plane, respectively. The FWHM and integrated area were calculated from the fit parameters to obtain V_c and the crystallite size, l, by Equations 2.39 through 2.41. The calculated values of V_c and l are shown with the measured current as a function of time in Figures 7.9a and 7.9b for Potentiostatic steps to 1.2 V and 1.6 V, respectively. Errors in V_c and l can be estimated from the standard deviation of the fit parameters, but are on the same order as l and V_c and are not shown for clarity.

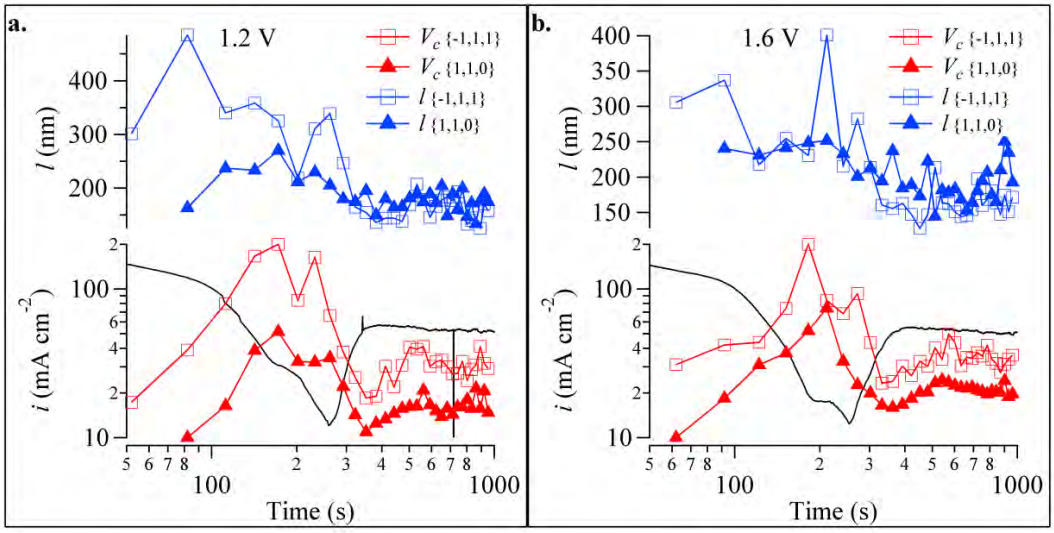

Figure 7.9a and 7.9b are plots of the measured current (black), salt volume (red) and crystallite size (blue) as a function of time after a potential step to 1.2V and 1.6V, respectively.

7.a.2.i Total Salt Volume and Crystal Size

The same trend in V_c can be observed in these experiments, as in Figures 7.8a through 7.8d, with V_c reaching a maximum before the current minimum and decreasing to steady state. Crystallite sizes on the order of 100 nm are observed throughout the potential step and are typically larger before the current minimum and decrease to steady state values with V_c. The crystallite sizes estimated from the peak shape should not be considered accurate to more than one significant digit (i.e. ± 100 nm), owing to the assumption of the detector function and calibration using NBS 640c silicon, which has a broad distribution of crystallite sizes. However, the crystallite sizes appear to be larger but also subject to larger fluctuations before the current minimum. When the current density, i, reaches a steady state, values of l decrease to approximately constant values.

Although large errors are present in the analysis of these experiments, the data are significant in terms of reproducibility. Experimental results shown in Figures 7.9a and 7.9b were obtained with a slightly larger beam and lower flux and show the same trend as in Figures

7.8a through 7.8d, with respect to V_c. Thus, it can be concluded that the trend in salt volume, after a potential step, is reproducible regardless of the beam size. Because the same trend in V_c can be observed, for both experiments, it can also be concluded that there is no significant beam damage, when a higher flux was used for the SAXS/WAXS experiments discussed previously.

7.a.3 Radiography results

In Chapter 3, the raw radiography data were used to extract values of A_{max} and x_B, which provide information about the mass absorption near the interface and the position of the salt film boundary, respectively. Both values are shown as a function of time, with the current, after a potential step to 1.6 V and 1.0 V in Figures 7.10a and 7.10b, respectively. Just after the step, A_{max} increases rapidly, while the current is decreasing as the concentration of dissolved nickel increases near the interface. The salt film boundary, x_B, and A_{max} increase during the first 60 s as supersaturation conditions are also present far from the interface. The salt film then forms but the amount of Ni(II) required to prevent the salt from dissolving cannot be supplied by the low current, resulting in salt film dissolution[27]. During dissolution, x_B decreases before the current minimum, following the similar trend in V_c shown in Figures 7.8a through 7.8d and Figures 7.9a and 7.9b. The inset in Figures 7.10a and 7.10b show the general trend of the profile, A, as the salt dissolves toward the interface. The value of A between ca 8 μm and x_B has a maximum value of 1.45±0.5 and remains constant during salt film dissolution. Once the current reaches a steady state value, the value of A_{max} is constant at ca 1.8. The value of x_B also remains constant with the current, but is higher at 1.6 V than at 1.0 V. These trends were also observed for another experiment to 1.6 V, not shown here.

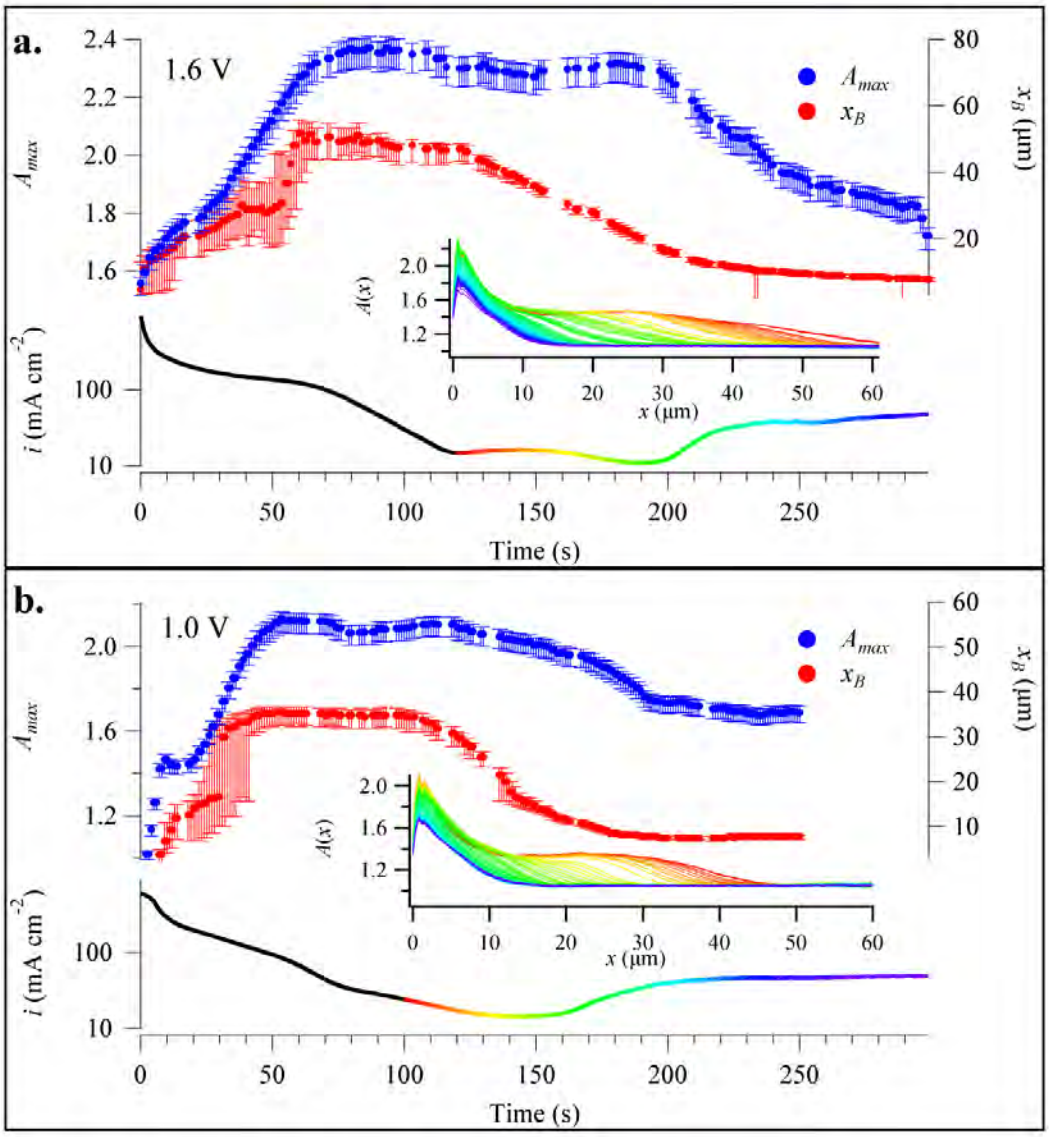

Figure 7.10a and 7.10b are plots A_{max} (blue), x_B (red) and current (black) as a function of time after Potentiostatic steps to 1.6V and 1.0V, respectively. The insets in both figures show how the $A(x)$ profile changes as x_B decreases and each trace colour corresponds to the colour in the measured current. Errors in Amax and x_B come from Errors in the background absorption profile and Statistical errors in the averaging discussed in the Section 3.b.2.vi. Errors in the profiles, $A(x)$, are not shown for clarity.

7.a.4 Transport Modelling

Results from X-ray experiments, obtained from a dissolving nickel artificial pit, have been presented earlier in this chapter and the simplest model for the small angle scattering results is a high density liquid surface layer that precedes nucleation. Because the metal undergoes aggressive dissolution after a potential step, a high concentration of Ni^{2+} is expected near the interface, which is likely to be the source of this layer. In addition, the presence of a concentrated Ni(II)Cl solution would provide the necessary contrast for small angle scattering. Analysis of radiography data shows that indeed the value of A_{max} increases rapidly after the potential step, as the concentration of Ni^{2+} increases. A simple, theoretical transport model could also provide some insight into the supersaturation conditions near the interface during the potential step and so was performed here for comparison. This approach assumes dilute limit transport and has been applied fruitfully in pitting corrosion before[79, 84, 97, 98]. Because precipitated salt is observed at ca 60 s (Figure 7.1 and Figure 7.7) results from this modelling are only useful to about 60 s, as the salt film is not accounted for.

It is common when modelling pitting corrosion (and other electrochemical systems) to assume a dilute system[79, 82, 84, 97, 98], where Equations 2.49 and 2.50 are used; in some cases, migration is also often neglected. Although, it is well known that transport is restricted in solutions more concentrated than 2 M[18, 24, 25, 103], the dilute limit assumption has had some success in explaining experimental results and is usually considered a good approximation[79, 84] for corroding pits. Although some modelling work has been published for artificial pits[97, 98], none have been performed for a potential step.

From a mathematical standpoint, a one dimensional ionic transport model is a system of nonlinear partial differential equations that require initial, as well as boundary conditions

during the potential step[18]. The system is one-dimensional in space, where *x* is the distance from the interface. A fixed boundary is used here because the pit depth (~1 mm) is much greater than depth added during dissolution (~30 µm) and it is found that interfacial concentrations did not change significantly when the pit depth was increased even by 0.5 mm. Standard grid spacing was used through the pit, with smaller increments closer to the metal where the concentration is expected to change the fastest. With the appropriate boundary conditions, the 2-D (*x* and *t*) partial differential equations can be treated as a set of differential algebraic equations[104], using the "*pdepe"* function in Matlab. This approach requires consistent initial conditions, which were obtained by solving the boundary value problem, containing a set of steady state 1-D equations. This particular boundary value problem was solved using the *bvp5c* function in Matlab.

7.a.4.i Initial Conditions

In all potential step experiments performed here, the potential of the working electrode was decreased to zero, prior to salt film potential (>=0.4 V *vs.* Ag/AgCl), and held at 0 V for 300 s. During the 0 V period, the current density approaches a quasi-steady state current density below the limiting current density (*ca* 30 mA cm^{-2}), as shown in Figure 7.11. Because of the highly concentrated solution in the pit, transport is slow and the concentrations near the interface, before the potential step is assumed to be saturation (4.45 M). Although the solubility of $NiCl_2(H_2O)_6$ does decrease in 1 M HCl to 4.2 M[105], the pH near the interface will increase slightly, as the Ni^{2+} is dissolved, to maintain electroneutrality; this was confirmed with this model. Therefore, 4.45 M is taken to be saturation near the interface. Bulk concentrations at the pit mouth are also assumed, as discussed in the previous chapter. The flux of all species is assumed to be zero, except for Ni^{2+}, as a result of the semi-constant anodic current (Figure 7.11) just before the

Potentiostatic step. A mutual diffusion coefficient for saturated $NiCl_2$ is used(5.9×10^{-6} cm^2s^{-1}), while (9.6×10^{-6} cm^2s^{-1}) is used for the diffusion coefficient for H^+.

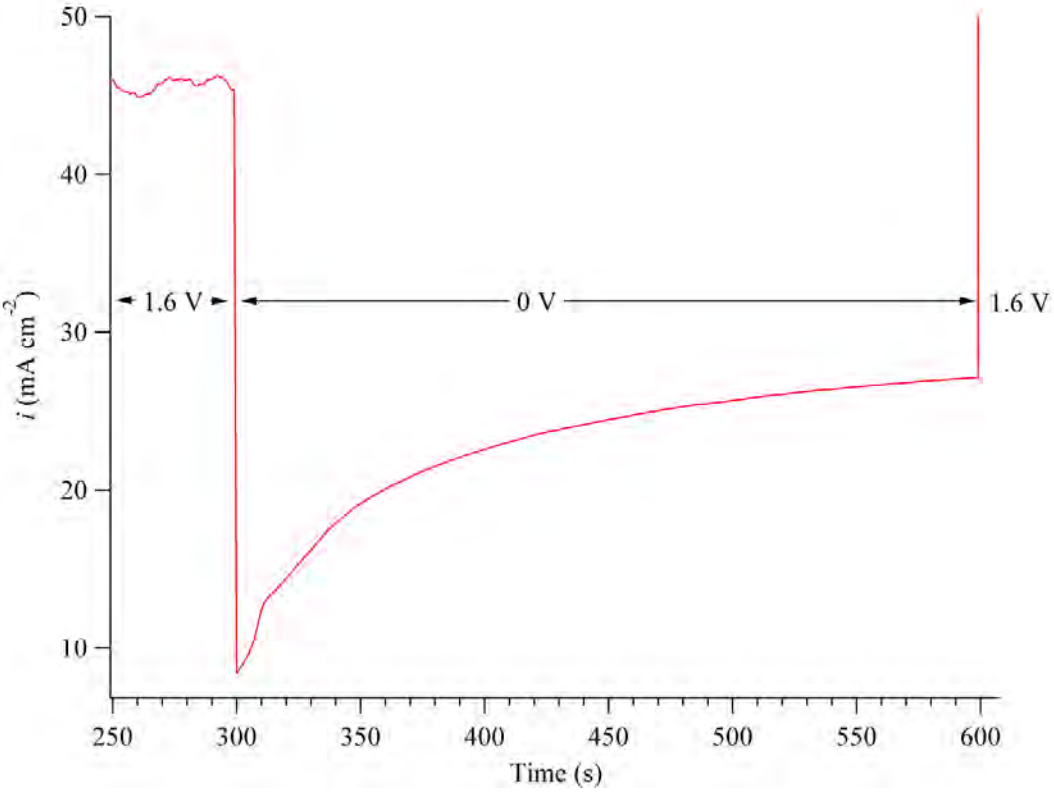

Figure 7.11 is a plot showing how the current responds when the potential is decreased to 0 V. The current always approaches a steady state value between 20 and 30 mA cm^{-2}.

Using these conditions, the boundary value problem is given by the equations:

(7.8) $\frac{dC_{Ni}}{dx} = \frac{-2F}{RT} C_{Ni} \frac{d\Phi}{dx} - \frac{i_I}{2FD_{Ni}}$

(7.9) $\frac{\partial^2 \Phi}{\partial x^2} = -\frac{F \sum z_i C_i}{\varepsilon}$

} Pit

(7.10) $C_H = C_H^{\infty} e^{\left(-\frac{F\Phi}{RT}\right)}$

(7.11) $C_{Cl} = C_{Cl}^{\infty} e^{\left(\frac{F\Phi}{RT}\right)}$

(7.12) $C_{Cl}^{\infty} = C_H^{\infty} = 1M$

(7.13) $C_{Ni}^{\infty} = 0M$

(7.14) $\Phi^{\infty} = 0$

} Pit Mouth

where all symbols are the same as in Chapter 2. Equations 7.10 and 7.11 are valid when there is no net Cl^- or H^+ flux[18], which will be the case when there is little change in the current (Figure 7.11) before the potential step. The assumptions that underlie Equations 7.12 through 7.14 are reasonable assumptions, given the pit depth, and have been used before in similar situations[97, 98].

The Nernst-Plank equation is used to calculate the concentration gradient for nickel and the Nernst-Einstein relationship used for the mobility[97, 98]. In theory, i_I, should be between 20 and 30 mA cm^{-2} (Figure 7.11). However, these values resulted in concentrations less than saturation near the interface. Therefore, the value of i_I was increased until saturation exists at the interface. A value of 127 mA cm^{-2} for a 1 mm pit and 63 mA cm^{-2} for a 2 mm pit was found to satisfy saturation conditions at the interface. This value of i_I is much higher than experimentally observed and most likely a result of the dilute limit assumption; values of i_I

can be further decreased by decreasing the mutual diffusion coefficient of $NiCl_2$. The results from Equations 7.8 through 7.14 are shown in Figure 7.12.

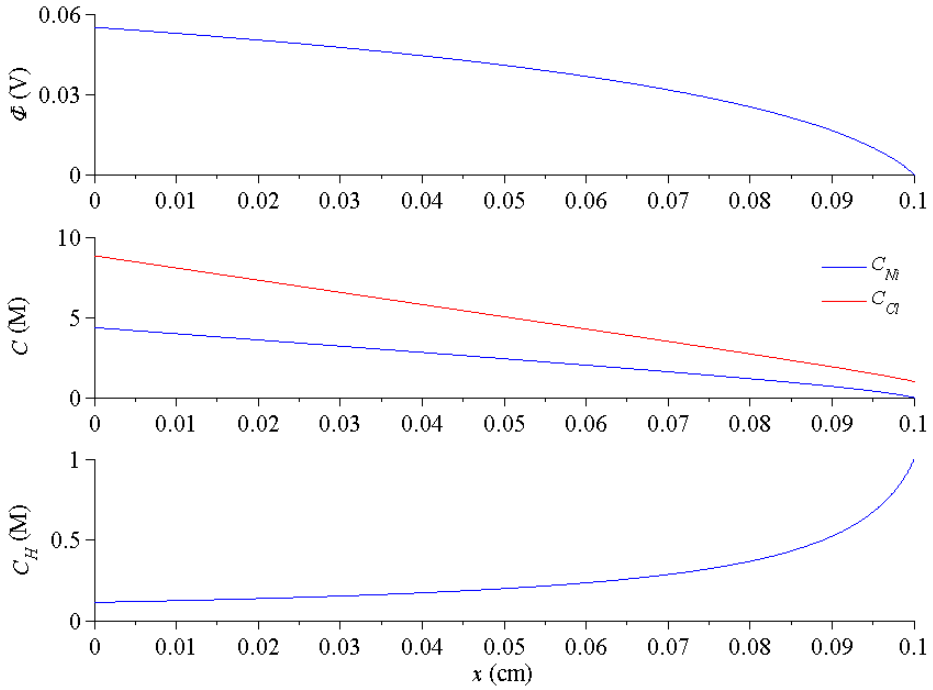

Figure 7.12 is a stack plot showing the potential and concentration profiles calculated using Equations 7.8 through 7.14. These initial conditions were used to model the potential step experiments.

Concentration and potential gradients obtained by this method agree well with those reported in previous work for nickel pits[97, 98]. In the artificial pit cell used, the working electrode potential would be less than 0.222 V (Ag/AgCl), owing to the potential drop across the double layer and through the pit and the liquid junction potential between the working and reference electrode. Thus, a value of 0.06 V can be considered a reasonable value, keeping in mind that absolute scaling of the solution potential is somewhat arbitrary[18, 97], but should be on the same order.

7.a.4.ii Potential step

Using the initial conditions in Figure 7.12, the potential and species concentrations can be calculated, in both space and time, by the equations:

(7.15) $\frac{\partial C_i}{\partial t} = \frac{\partial}{\partial x}\left(z_i \frac{FD_i}{RT} C_i \frac{\partial \Phi}{\partial x} + D_i \frac{\partial C_i}{\partial x}\right)$

(7.16) $\frac{\partial^2 \Phi}{\partial x^2} = -\frac{F \sum z_i C_i}{\varepsilon}$

Pit

(7.17) $J_{Ni} = \frac{i}{2F}$

(7.18) $J_{Cl} = J_H = 0$

(7.19) $\frac{\partial \Phi}{\partial x} = \frac{i}{\kappa} = \frac{i}{\frac{F^2}{RT}\sum D_i C_i}$

Pit Bottom

(7.20) $C_i = C_i^{\infty}$

(7.21) $\Phi = 0$

Pit Mouth

where J is the flux and is also equal to the term in parenthesis in Equation 7.15, κ is the conductivity and the Nernst-Einstein relationship is used for the mobility in Equations 7.15 and 7.19. Because electroneutrality is not forced upon Equation 7.16, the individual diffusion coefficients for Ni^{2+} and Cl^- were used and were considered a function of concentration, interpolated from experimental data in previous work[21]; the diffusion coefficient for H^+ is taken to be that at infinite dilution[20](9.6×10^{-6} cm^{2}s^{-1}). The current density, i, is obtained from the measured current shown in Figure 7.11a, which is a shallow pit (~1 mm), as evidenced from the higher steady state current density compared to the radiography experiments, which were closer to 2 mm. The system of equations are solved only to 100 s

after the step because precipitated salt is not accounted for and is clearly observed at 100 s after the step in all experiments (Figures 7.8a through 7.8d).

Equation 7.15 is applicable only at the dilute limit and Equation 7.19 is Ohm's law for electrolytes and assumes no concentration gradient near the interface. At this point, these assumptions may seem farfetched for such a concentrated system, but they are used fruitfully in electrochemistry because accounting for concentration effects is non-trivial and has only been modelled in recent years[23-25].

The concentration profile of Ni^{2+} as a function of distance, *x*, and time, *t*, is shown in Figure 7.13. It can be seen that the Ni^{2+} concentration and concentration gradient between 0 cm and 0.05 cm increases rapidly, while the concentration profile between the 0.05 cm and 0.1 cm does not change significantly throughout the potential step. Figure 7.13 serves to show that the system of equations were solved successfully and result in smooth concentration profiles that change, as expected with an increase in the current density. Similar plots can be generated for other species and the potential, but are not shown for brevity.

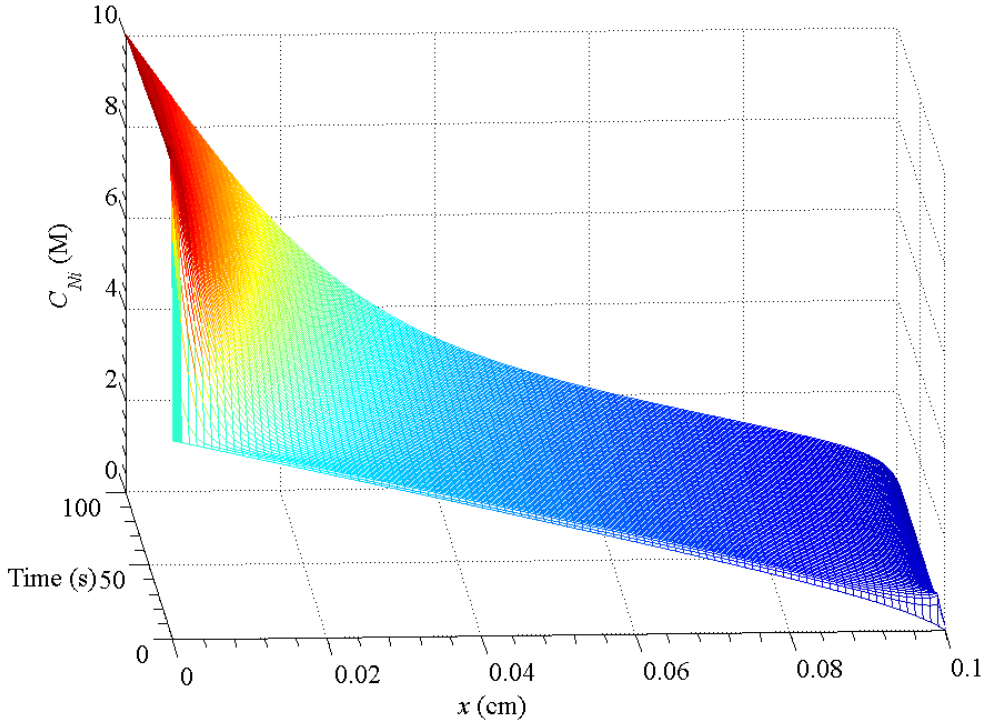

Figure 7.13 is a mesh plot of the dissolved nickel concentration as a function of distance, x, and time. The concentration profiles were obtained by solving the system of partial differential equations (Equations 7.15 to 7.21), using the current density in Figure 7.8a.

Finally, the supersaturation ratio, at the interface, can be plotted with the current and time and is shown in Figure 7.14. Initially, the current density decreases, while the supersaturation ratio increases and reaches a maximum supersaturation ratio of 2.4 at approximately 7 s after the Potentiostatic step. Although this galvanostatic model does not contain any relationship between the dissolution kinetics and the interfacial Ni^{2+} concentration, an increase in the interfacial Ni^{2+} concentration is predicted, which would decrease the experimental current. At these high concentrations, the conductivity through the pit is expected to decrease[23], which would decrease the potential at the metal surface (Equation 2.44) and thus the current (Equation 2.46). Thus, up to 7 s, the simple transport model predicts an increase in the interfacial Ni^{2+} concentration, as nickel transport away from the interface is much slower than dissolution; this increase is expected to decrease the measured current, which is also

observed. Once the maximum is reached however, the current density decreases drastically, while the supersaturation ratio decreases, which is unexpected.

Anisotropic small angle scattering is observed *ca* 20 s after the potential step and was attributed to a surface layer containing a highly concentrated $NiCl_2$ solution. Based on radiography experiments, the value of A_{max} increases, monotonically, to *ca* 50 s and must be due to the increasing concentration of dissolved nickel. However, a highly concentrated $NiCl_2$ solution, near the interface, is not predicted in the model results in Figure 7.14. Clearly, supersaturation ratios of 2 are well beyond the dilute limit and one likely explanation for the discrepancy is that ionic transport is largely overestimated with this model, even though the diffusion coefficients were considered to be a function of concentration. Of course, no diffusion coefficients have been reported for supersaturated $NiCl_2$ and only the values of saturated $NiCl_2$ could be used. Furthermore, the ionic mobility, estimated by the Nernst-Einstein equation, is also over estimated because the conduction mechanism changes at *ca* 3 M for many electrolytes as short range interactions can no longer be neglected; relaxation and electrophoretic effects are also neglected, which would also restrict transport. Thus, the discrepancy between the dilute model and experimental results is likely due to concentration effects, which would further restrict transport away from interface and cause the interfacial Ni^{2+} concentration to continue to increase beyond 7 s.

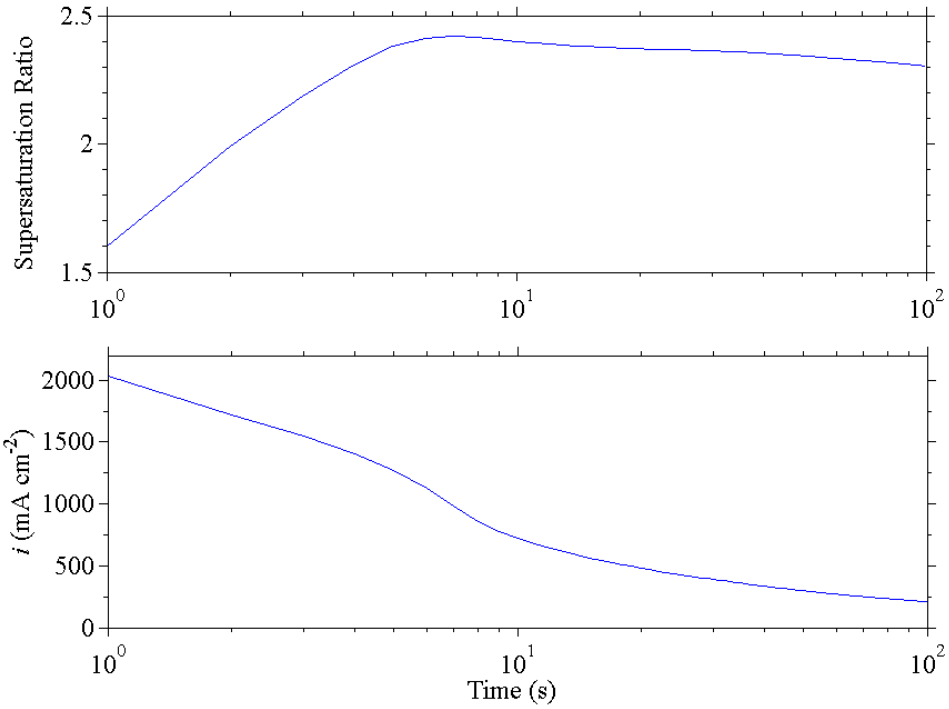

Figure 7.14 is a stack plot of the supersaturation ratio (top) and the current density (bottom) versus time (log scale), obtained from solving (Equations 7.15 to 7.21), using the current density in Figure 7.8a.

7.a.5 Discussion

Potential step experiments were performed on nickel artificial pits to explore interfacial phenomena that lead to salt film formation. The SAXS signal from the concentrated surface layer increased to a maximum at approximately 60 s and decreased with increasing salt volume, observed by X-ray diffraction. Analysis of radiography data showed that after the potential step, the near interfacial absorption, A_{max}, increased to a maximum at about 50 s and can also be attributed to an increasing $NiCl_2$ concentration. The measured current from the SAXS/WAXS experiments was used to model ion transport after the potential step and showed that the interfacial $NiCl_2$ concentration reaches a maximum sooner than that observed by radiography, which is a consequence of the dilute assumptions made in the model. Comparison between the model supersaturation and X-ray data suggest that ionic transport near the interface cannot be considered to be at the dilute limit. Differences in the interfacial

Ni^{2+} concentration predicted by the model and experimentally observed are most likely because concentration effects are not accounted for in the model. Thus, the surface layer formation is discussed in the context of restricted transport that is present near the interfaced after the potential step. A theory for the surface layer formation that is consistent with the experimental results is presented and is based on restrictive transport.

After the salt film precipitates, the total volume of salt increases to a maximum before the current density reaches a minimum. After the current density passes through a minimum and begins to increase to steady state, the total salt volume decreases to a steady state value. Analysis of the radiography data shows that during this salt film dissolution, the salt film thickness decreases, while its absorption remains constant. Thus, the salt film does not precipitate to a steady state thickness and, instead, precipitates to a thickness too large to be maintained by the nickel dissolution and must dissolve to a steady state thickness. This thickness "overshoot" is likely a result of super saturation conditions that exist prior to nucleation. Supersaturation conditions, far the interface (on the micron scale) could determine how the salt film arrives at a steady state thickness.

7.a.5.i Surface Layer Formation

The sequence of events proposed for the formation and dispersion of a highly concentrated liquid layer that results in the transient anisotropic SAXS signal are described schematically in Figure 7.15. In the first step, the layer is formed as the Faradaic flux of Ni^{2+} is greater than the ion flux away from the surface; chloride ions will migrate towards the metal to maintain charge balance.[96, 98] Continued dissolution results in local increases in the Ni^{2+} concentration, along with the formation of a transient boundary (Figures 7.8a through 7.8d). The presence of a transition layer implies that the transport of Ni^{2+} is very slow despite a

steep concentration gradient that must exist at the boundary. During the surface layer formation, the mechanism of transport must therefore be more consistent with a "hopping-conduction" mechanism[23] than with the classic DHO theory.

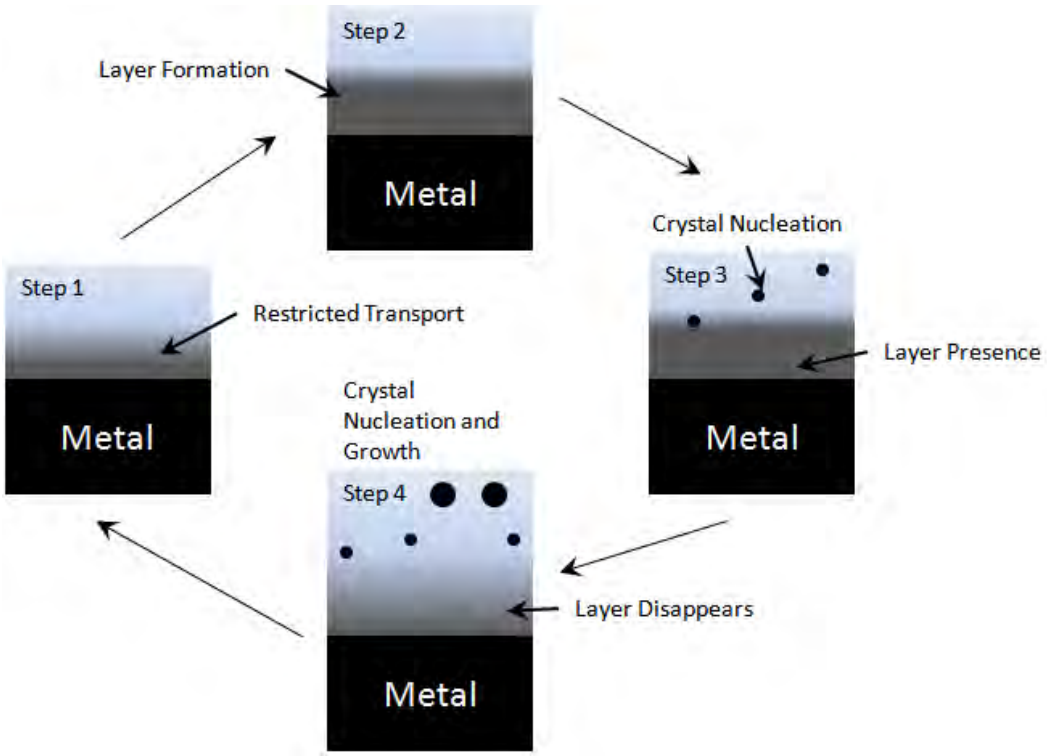

Figure 7.15 is a schematic illustration of the sequence of events proposed for the formation and dispersion of the surface layer followed by its subsequent disappearance as a result of crystal nucleation and growth.

Results from transport modelling can be used to understand the possible compositions of the surface layer. The Ni^{2+} concentration profile shows a very rapid, linear decrease near the interface (Figure 7.16). The linear decrease arises from the fact that the potential gradient is smallest near the interface and results in diffusion dominated transport in this region; previous authors have also obtained this result[79, 97, 98], assuming electroneutrality. A negligible potential gradient is obtained because of the F/ε factor in Equation 7.16 (10^{16} V cm mol^{-1}), slight deviations from electroneutrality would then cause an appreciable increase in the electric field, which causes Ni^{2+} cations to migrate away and Cl^- anions to move toward the interface. If, however, transport is more restricted than assumed in the

model, deviations from electroneutrality may occur and a much larger potential gradient could exist as the Cl^- would be unable to reach the interface.

Although departures from electroneutrality are likely near the interface, the large electric field produced near the interface would not necessarily cause the Ni^{2+} to migrate away. Classic Debye-Huckel-Onsager (DHO) transport theory does not account for short range interactions between ions, which would undoubtedly differ from long range forces. Conduction in concentrated environments has been studied recently and been modelled by a so called "hopping" mechanism, whereby ions are assumed to form a pseudo-lattice[23]. Considering this transport mechanism, it is possible that the surface layer contains an unbalanced electrolyte, with a large concentration of Ni^{2+} cations. Departures from electroneutrality cannot be theoretically modelled here because the formulation is highly non-trivial and requires knowledge of the ion-ion and ion-solvent interactions, which were not investigated. However, recent work has shown that ion transport can become extremely restricted in such a concentrated environment[23], which could result in an unbalanced layer composition.

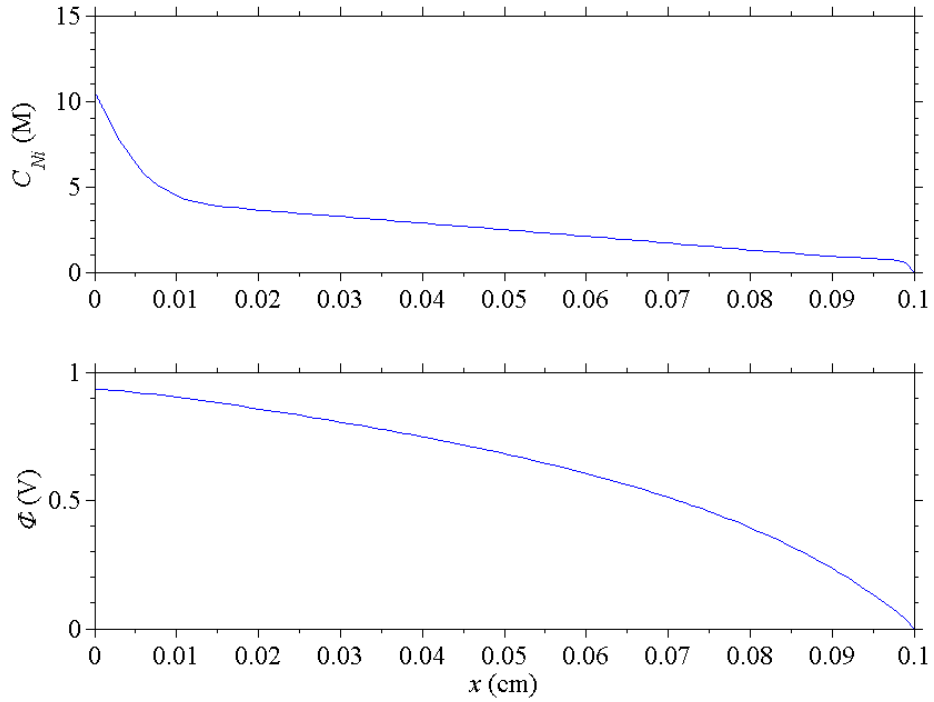

Figure 7.16 is a stack plot of the Ni^{2+} concentration profile (top) and potential profile (bottom) when the maximum interfacial concentration of Ni^{2+} is encountered in the transport model.

The observation of small angle scattering requires a significant difference in electron density between the layer and adjacent solution. Although, it is possible that the layer contains an unbalanced and supersaturated Ni(II)Cl solution, it is assumed here that the layer is electrically neutral to show that a sufficient small angle scattering signal can be obtained. Analysis of A_{max} at 60 s (Figures 7.10a and 7.10b) results in an estimated concentration of nickel chloride of between 8 and 9 M, ~1 µm above the interface. Thus, the density of the adjacent phase must be on the order of 2 g cm^{-3}, predicted for nickel chloride at those concentrations[106]. Based on predictive density modelling[106], a layer of molten $NiCl_2$ would have a density of 3.5 g cm^{-3}, corresponding to a $\Delta\rho^2$ value on the order of 200 x 10^{20} cm^{-4}, which would give a clear SAXS signal. Thus, a surface layer composed of only nickel chloride would give a sufficiently strong SAXS signal. It is likely that the proposed surface layer would contain some water, but it is not possible to estimate the mass fraction.

Continued dissolution and build up of dissolved Ni(II) near the interface results in a well-defined surface layer at ~60 s and shown in step two in Figure 7.15. As time progresses, the value of Q_φ increases, which could be due to the formation of additional layers, an increase in the layer thickness and a possible increase in contrast if the concentration of Ni(II) increases in each layer. Unfortunately, the contrast and total volume cannot be separated in Equation 7.7 and no clear Guinier knee can be observed in the SAXS data. However, all three effects would have the same contribution to Q_φ, as more nickel is dissolved.

7.a.5.ii Surface Layer Dissipation and Crystal Nucleation

Following the surface layer formation, precipitation of crystalline $NiCl_2(H_2O)_6$ occurs in the solution adjacent to the surface layer. As shown in Figures 7.8a through 7.8d, the total salt volume (V_c) rapidly increases only after the surface layer is fully developed. Crystal nucleation theory predicts a rapid increase in the nucleation rate when a critical supersaturation value is reached, regardless of the crystal structure[87]. Critical supersaturation ratios predicted by the method of Ruckenstein depend on the value of the monomer-monomer and monomer-solvent interaction, which also depends on the crystal structure.[89] It can be hypothesized that a critical concentration of Ni(II) is reached when the surface layer is fully developed and nucleation spontaneously occurs at or near the surface layer. Typical supersaturation ratios for crystal nucleation vary significantly between 2 to 300, with the predicted ratio of molten salt to saturated nickel chloride at 15. Although it is not clear where the crystal nucleation occurs, it is likely to take place at the boundary where more water is available, and/or when the stoichiometric amount of Cl^- reaches the boundary. Once nucleated, crystallites are transported away from the surface layer by diffusion or diffusion/electrophoresis, depending on whether or not the particles are charged. This process is show schematically as Step 3 in Figure 7.15.

During crystal nucleation and growth, scattering from the surface layer begins to disappear (Figures 7.8a through 7.8d). As the surface layer disappears, the transition layer thickness increases. An increase in the transition layer thickness suggests that the surface layer boundary transitions to a continuous gradient, too large to give a SAXS signal. Thus, continued nucleation and growth causes the concentration of nickel in the surface layer to decrease. A decrease in the nickel chloride concentration could restore traditional DHO transport, causing the well-defined surface layer to transform into a continuous concentration gradient. Without a well defined surface, the SAXS signal completely disappears by ~120 s and shown as Step 4 in Figure 7.15. Interestingly, the current density begins a rapid decrease shortly after the surface layer disappears. Correlation between the disappearance of the surface layer and the current provides additional evidence that the anisotropic scattering is from a surface layer near the reaction plane.

7.a.5.iii Dissolution to Steady State

Both the salt film boundary, x_B, (Figures 7.10a and 7.10b) and the salt volume (Figures 7.8a through 7.8d) reach a maximum value and begin to decrease at an inflection point before the current minimum. Agreement between the XRD and radiography data suggest that newly precipitated salt crystals extend far out into solution (>20 μm) before they begin to dissolve. Strong correlation between salt dissolution and a change in the current density is likely to be due to sudden changes in the resistance between the working and reference electrode; though the ion flux away from the reaction plane is expected to increase as more salt film dissolves and would also affect nickel dissolution.

During dissolution, A remains constant at 1.45±0.5 between ca 8 μm and x_B, suggesting that ion transport within this region is restricted enough to prevent homogenous dissolution inside

but fast enough at the boundary to cause the salt film to dissolve. Also, the observation that *A* remains constant between ca 8 μm and x_B, suggests that ion transport in this region is very slow either because of the high concentration or the presence of non-conducting salt.

The volume fraction of salt at $A = 1.45$ can be calculated, with few assumptions. Between 8 μm and x_B, salt is not dissolving or growing, as the concentration must be near saturation. Using the appropriate values of μ/ρ for Ni, Cl, H and O (at 15 keV), the density of saturated $NiCl_2(H_2O)_6$ (1.42 g cm^{-3} at 4.45 M) and the density of $NiCl_2(H_2O)_6$ (1.92 g cm^{-3}), the volume fraction of salt (v_{salt}) is calculated to be 20%. Though, no volume fraction of salt has been reported in nickel salt films, the porosity has; the porosity is defined as the area available for transport divided by the actual geometrical area and is a purely geometrical correction applied to conductivity measurements[26]. To a first approximation, salt volume fraction and porosity are related by: $\phi \approx 1 - v_{salt}$. The calculated porosity in the salt film during this time is much larger than steady state values of ca 0.1% reported by others,[27, 96] This large discrepancy is not surprising since the previous work considered the steady state film rather than the dissolving one observed here. In addition, previous calculations have assumed that all of the resistance is due to the presence of salt.

7.a.6 Conclusions

1) *In-situ,* artificial pit experiments have provided insight into interfacial and near-interfacial phenomena when instantaneous high dissolution conditions are imposed on a restricted transport system. Following a potential step, ionic transport can be restricted enough such that a non-crystalline layer of salt solution with extremely high supersaturation approaching that of molten salt can temporarily exist. The presence of a sharp concentration gradient at the surface layer/electrolyte interface inferred from a highly anisotropic SAXS

signal indicates that transport of dissolved species inside are not concentration dependent. When a critical supersaturation ratio is reached, nucleation of salt crystals occurs in or near the surface layer. Continued nucleation decreases the concentration inside this layer until a SAXS signal is no longer observed. A sharp decrease in the current density always follows the disappearance of this layer and correlates with a change in ionic concentrations at the reaction plane.

2) Analysis of XRD and radiography data lead us to conclude that a temporarily thick salt film forms and dissolves towards the metal surface to a steady state thickness. During dissolution, ion transport between ca. 8 μm and the salt film boundary is restricted enough to prevent homogenous dissolution of the salt film. A salt volume fraction of ca 20% is calculated from within the dissolving salt film, which is much lower than that that previously found for steady state salt films.

3) A simple transport model was used to show how the dilute limit assumption fails near the interface and is clearly not an appropriate assumption; although, the dilute limit assumption, and even simple diffusion, have been shown to accurately describe transport throughout the entire pit. A complete transport model that takes into account concentration effects, short range interactions and salt film precipitation was not performed here, but could provide invaluable insight into the interpretation of the experimental results, particularly the composition of the surface layer. Because the surface layer precedes nucleation, a calculation of the critical supersaturation ratio for $NiCl_2(H_2O)_6$ could also provide an estimate of the concentration inside the surface layer, or at its boundary, prior to its disappearance. However, this calculation is non-trivial and would require knowledge of system specific parameters required by any crystal nucleation theory[87].

CHAPTER 8
Conclusions and Future Work

In this chapter, the conclusions and future work from the AC electrograining and nickel artificial pit systems are discussed. Interfacial phenomena that occur in two different electrochemical systems have been discussed in previous chapters. In the electrograining study, phenomena occurring in the smut were studied. Because the overall goal of electrograining is controlling the final surface morphology, the practical focus of future work would be finding a relationship between how the smut permeation properties can be manipulated to obtain a specific aluminium surface morphology. From an electrochemical point of view, the effect of gas release on the dissolution kinetics is also interesting. Of course, the mechanism of gas release is determined by the smut gel, whose mechanical properties could be manipulated with the incorporation of additives, which have been shown to be present in the smut[36].

Interfacial phenomena that occur during a potential step were also studied in nickel artificial pits, with the focus on salt film formation. From a corrosion point of view, salt film formation can be considered to be undesirable, as the salt film maintains the aggressive solution chemistry necessary for dissolution[77, 78]. This practical approach could involve the addition of additives or other means to prevent salt film formation. Modelling the salt film formation also presents a very challenging opportunity to apply recent advances in modelling the ion transport[23-25] and crystal nucleation[87] to reproduce the change in measured current.

8.a Electrograining

8.a.1 *in-situ* SAXS

The initial experiments described in Chapter 5 were focussed on developing SAXS as a technique that can probe the structure of smut *in-situ*. It was shown that scattering from the pitted surface can be neglected in the analysis of SAXS data obtained after electrograining and is dominated by scattering from the smut. The scattering curve, $I(q)$, was modelled as agglomerated $Al(OH)_3$ particles using a two level unified equation. Analysis of parameters obtained was interpreted as scattering from isolated, compact agglomerates that contained little to no branching. Although good fits were obtained in all cases, future experiments should be performed at lower q, if possible, to obtain information about the agglomerate sizes and mass fractal dimension, which appear to change with the electrograining conditions. However, the *in-situ* SAXS experiments in this thesis were performed with a modest q-range at the DUBBLE beamline. The q-range available on other SAXS beamlines would be similar and would not likely be able to provide much more information about the larger agglomerates. Although the scattered intensity can be measured at lower q values via USAXS, the data collection time is much longer with the Bronse-Hart arrangement that is normally used at USAXS beamlines, which makes *in-situ* studies of electrograining difficult.

Finally, the time resolution is an important factor in the total scattering analysis, as gas release occurs in less than 10 s. The limiting factor for time resolution is the signal obtained from the smut. A sufficient signal was obtained for SAXS frames between 4 s and 6 s at the DUBBLE beamline. Advances in detector technology (i.e. solid state detectors) may allow for a sufficient signal to be obtained at shorter exposure times; these are currently being implemented at the DUBBLE beamline.

Of course, the signal can be also increased by increasing the flux incident on the sample, which can be accomplished by performing the experiments on beamlines with an undulator source such as I22 at the Diamond Light Source. If a higher flux is to be used, the potential response should also be measured simultaneously to ensure that the electrochemistry in the cell is consistent with what is expected. Beam damage is a common problem in liquid samples and one consequence would be sample heating, which should change the potential response.

8.a.2 Sample Cell

The scattering signal can also be increased by decreasing the beam attenuation in the flow cell. Most of the beam attenuation results from the Al foil and the electrolyte. In the experiments presented in Chapter 5, thin (40 μm) foils were used to minimize beam attenuation. However, one of the drawbacks of these foils is that very low current densities must be used and the electrograining time cannot exceed about 100 s. When too much charge is passed, much of the Al metal is removed and the background scattering from the remaining metal is markedly lower than that of the original ungrained Al foil, which must be used as the scattering background. Thicker Al sheets (200 μm) were used, with an increased energy, to try and avoid this problem, but the results obtained were very noisy and these experimental conditions were not considered optimal. However, thicker foils (~80 μm) could be used in future experiments, especially if the experiments were performed with a higher X-ray flux.

The distance between electrodes was kept to a minimum by using the minimum available PTFE sheet thickness (1 mm). A shorter distance between electrodes can be obtained by using only parafilm to separate the electrodes. This was attempted in a few samples, but it was difficult to ensure consistent cell thicknesses and that some of the parafilm does not

cover the samples. An alternative material is Surlyn, which is a clear plastic that is commonly used in packaging. This material flows when heated and provides a seal[107] (instead of parafilm) and it is available in 100 µm sheets. Thus, surlyn can be used to regulate the through thickness of the electrolyte and provide a seal for the cell, instead of a PTFE spacer and parafilm.

8.a.3 Other techniques

Small angle scattering is the primary technique employed in the studies described in this thesis. Using SAXS in the electrograining system, changes in the total scattering was correlated with changes in the gas fraction in the smut after electrograining. After the completion of the entire electrograining sequence, multi-sine impedance measurements were also performed such that four separate impedance spectrums were obtained every 6 s after the final electrograining burst. Results obtained from these experiments are currently being interpreted and show differences in the impedance spectrum as gas is released after electrograining. Using time resolved impedance, the gas release could be correlated with a capacitive component in the smut and SAXS measurements would not be required.

8.a.4 Gel Permeation

It is hypothesized that gas permeation depends on the mechanical properties of the smut. Future work that focuses on altering the mechanical properties of the smut gel could provide some insight into how to alter the gas permeation mechanism with certain additives. The ability of smut to permeate gas could be measured by first electrograining for a sufficient period of time to form the smut gel. Following smut formation, a slightly cathodic potential could be placed on the working electrode to allow hydrogen gas to evolve, whilst the current is measured; alternately, the experiment could be performed galvanostatically.

Ex-situ gel precipitation could also prove to be a useful technique that can be used to form many different precipitated gels. The mechanical properties of the gels could then be evaluated by any number of methods used in colloid science. Additionally, *ex-situ* USAXS experiments could be performed on the gels to see if there is any change in the $Al(OH)_3$ structure with different additives. Thus, using *ex-situ* gels would allow for many different gels to be evaluated, as opposed to *in-situ* smut, which requires significantly more time and preparation to evaluate.

Because of the limited time allotted during beamtime, not all planned experiments could be performed. *In-situ* electrograining experiments, performed with a DC offset, were thought to be very promising. In these experiments the amount of smut formed could vary and could also change the smut permeability. However, the biggest advantage to these experiments is that the amount of H_2 gas evolved changes and could provide additional information about how much gas the smut can evolve before it mechanically breaks down. Some of these experiments were performed in the last beamtime session, but the data was deemed unreliable because of abrupt and unexpected changes in I_o and I_t in the calibration file.

8.b Salt Films

Salt film formation experiments were performed by applying a potential step to a nickel foil in an artificial pit. Following a potential step, ionic transport can be restricted enough such that a non-crystalline layer of salt solution with extremely high supersaturation approaching that of molten salt can temporarily exist. When a critical supersaturation ratio is reached, nucleation of salt crystals occurs in or near the surface layer. Continued nucleation decreases the concentration inside this layer until an anisotropic SAXS signal is no longer observed.

The formation of the surface layer was compared with a transport model that treated the electrolyte as a dilute solution. It was shown that, in this case, the dilute limit assumption could not reproduce the surface layer or interfacial absorption, A_{max}, obtained from the radiography data. Despite the fact that the dilute limit assumption is widely used in corrosion and electrochemistry, it is clearly not valid near the interface in an artificial pit and should be considered unrealistic!

8.b.1 Transport Modelling

Realistic modelling the formation of the surface layer, on the other hand, would require knowledge of ion mobility up to very high concentrations, where the conduction occurs by a different mechanism[23] and relaxation[25] and the electrophoretic effect[24] must be also considered. Because the surface layer precedes nucleation, a calculation of the critical supersaturation ratio for $NiCl_2(H_2O)_6$ could also provide an estimate of the concentration inside the surface layer (or at the boundary) prior to its disappearance. Once the salt film has precipitated, transport through it could approximated by the porosity by considering the local volume fraction of electrolyte available for transport[26]. The salt crystallites are relatively small and also move in response to concentration gradients and the electric field, as they are likely charged. At this point, some assumptions must be made about the salt particles, with the most convenient assumption being that they are not charged and are only transported via Brownian motion and gravity.

Analysis of XRD and radiography data lead us to conclude that a temporarily thick salt film forms, which dissolves towards the metal surface to a steady state thickness. During dissolution, ion transport between ca. 8 μm and the salt film boundary is restricted enough to prevent homogenous dissolution of the salt film. A salt volume fraction of ca 20% is

calculated from within the dissolving salt film, which is much lower than that that previously found for steady state salt films. Although no transport modelling is reported here, one could model the system with any number of commonly used assumptions[18] to determine whether a salt fraction of 20% would prevent homogenous dissolution.

8.b.2 Potential step

Potential step experiments performed involved potential steps to relatively high potentials to ensure salt film formation. However, this is unlikely to be how a salt film forms in a real pit. Experiments where the potential is stepped to lower potentials (i.e. 0.4 V) could provide evidence of whether or not a surface layer forms and precedes nucleation. Even though Potentiostatic steps to lower potentials may yield similar or different results, the mechanism behind salt film formation in a real pit may still be different. In this case, a real pit is much shallower and the salt film precipitation occurs under less transport restricted conditions. This concept can be explored further by using shallower artificial pits and slowly increasing the potential, instead of instantaneously stepping the potential.

8.b.3 Other Effects

Experiments were performed with 1 M HCl in a simple nickel artificial pit. Other acid concentrations have been considered in previous literature at steady state, but could be used in the potential step experiments to provide an excess Cl^- concentration. Under these conditions, salt film formation could be different because of the decrease in $NiCl_2(H_2O)_6$ solubility in higher acid concentrations. Although some experiments were performed with H_2SO_4, the data obtained were not of high enough quality to perform the same analysis. With the addition of H_2SO_4, a different salt phase is expected, which may or may not have the

same formation mechanism. Thus, future experiments with different electrolytes could provide interesting results to better understand salt film formation under different conditions.

8.b.3.i Artificial pit cell

The artificial pit cell that was used can be improved significantly to provide higher quality data that can analysed with a higher degree of accuracy. The first and most obvious problem with the artificial pit cell used is that the through thickness of the pit is not known. This is due to expansion of the kapton tape, just above the metal foil, and the necessary epoxy between the foil and tape. Glass encapsulation offers a more rigid and well defined pit, where the through thickness is known. This is most important with the radiography and could allow for the direct calculation of the solution concentration near the interface.

In theory, small angle scattering data can be calibrated so that the electron density contrast can be obtained, from the invariant, when the through thickness of the pit is known. In practice, this would be difficult in the artificial pit system because a calibrant, such as glassy carbon, would need to be placed inside the pit to obtain the scattering cross-section. However, if a pit could be grown and rinsed with water, it could be used as background, as opposed to the background used here, which was simply the SAXS image before the Potentiostatic step.

Thinner foils could also be used to minimize the curvature of the foil during dissolution. Although this curvature was estimated with radiography data, it did raise some questions as to whether the phenomena observed actually occurred on portions of the foil or the entire surface.

Finally, changes in temperature would affect the salt solubility, as well as the ion transport. A cell was designed to control the temperature but it proved difficult to ensure that the interfacial temperature was the same as that of the water flowing through the cell.

8.b.3.ii Gravity

Artificial pits used in these experiments were performed in such a way that gravity forced the salt film toward the metal surface. Experiments could be designed in such a way that the effect of gravity is reversed (upside down pit) and could prove to be useful in the understanding of how the salt particles move during formation and steady state. If gravity is what maintains the salt film close to the interface, thus restricting the transport, then possibly higher dissolution rates could be obtained in an upside down pit, as the salt is forced away from the metal surface increasing its porosity. Conversely, higher dissolution rates in the upside down pit could cause more salt to precipitate because gravity will have a minimal effect on ion transport. Thus, the effect of gravity could allow for a better understanding of how the salt film remains near the interface and if it has an effect on the metal dissolution rate.

Chapter 8 Conclusions and Future Work

References

[1] A. Guinier, *X-ray diffraction in crystals, imperfect crystals, and amorphous bodies*, W.H. Freeman, San Francisco,, **1963**, p. x, 378 p.
[2] A. Guinier and G. Fournet, *Small-angle scattering of X-rays*, Wiley, New York,, **1955**, p. 268 p.
[3] O. Glatter and O. Kratky, *Small Angle X-Ray Scattering*, Academic Press, New York, New York, U.S.A, **1982**, p.
[4] J. Als-Nielsen and D. McMorrow, *Elements of modern X-ray physics*, Wiley, New York, **2001**, p. xi, 318 p.
[5] C. A. Dreiss, K. S. Jack and A. P. Parker, *Journal of Applied Crystallography* **2006**, *39*, 32-38.
[6] G. F. A. Guinier, C. Walken, Trans., *Small-Angle Scattering of X-Rays*, John Wiley&Sons Inc., **1955**, p.
[7] G. Beaucage, *Journal of Applied Crystallography* **1995**, *28*, 717-728.
[8] J. A. Potton, G. J. Daniell and B. D. Rainford, *Journal of Applied Crystallography* **1988**, *21*, 663-668.
[9] J. E. Martin and A. J. Hurd, *Journal of Applied Crystallography* **1987**, *20*, 61-78.
[10] H. D. Bale and P. W. Schmidt, *Physical Review Letters* **1984**, *53*, 596-599.
[11] M. H. Kim, *Journal of Applied Crystallography* **2004**, *37*, 643-651.
[12] W. Ruland, *Journal of Applied Crystallography* **1971**, *4*, 70-&.
[13] C. G. Vonk, *Journal of Applied Crystallography* **1973**, *6*, 81-86.
[14] J. Ilavsky and P. R. Jemian, *Journal of Applied Crystallography* **2009**, *42*, 347-353.
[15] J. Y. Bottero, D. Tchoubar, J. M. Cases and F. Flessinger, *Journal of Physical Chemistry* **1982**, *86*, 3667-3673.
[16] A. Guinier, *X-Ray Diffraction*, W.H. Freeman and Company, Paris, France, **1963**, p.
[17] F. Schreier, *Journal of Quantitative Spectroscopy & Radiative Transfer* **1992**, *48*, 743-762.
[18] J. S. Newman and K. E. Thomas-Alyea, *Electrochemical systems*, J. Wiley, Hoboken, N.J., **2004**, p. xx, 647 p.
[19] E. E. A. El Aal, W. Zakria, A. Diab and S. M. A. El Haleem, *Journal of Materials Engineering and Performance* **2003**, *12*, 172-178.
[20] in *CRC handbook of chemistry and physics*, *Vol.* Chapman and Hall/CRCnetBASE, Boca Raton, FL, **1999**.
[21] R. H. Stokes, S. Phang and R. Mills, *Journal of Solution Chemistry* **1979**, *8*, 489-500.
[22] J. F. Dufreche, O. Bernard, S. Durand-Vidal and P. Turq, *Journal of Physical Chemistry B* **2005**, *109*, 9873-9884.
[23] L. M. Varela, J. Carrete, M. Garcia, L. J. Gallego, M. Turmine, E. Rilo and O. Cabeza, *Fluid Phase Equilibria* **2010**, *298*, 280-286.
[24] J. F. Dufreche, O. Bernard and P. Turq, *Journal of Chemical Physics* **2002**, *116*, 2085-2097.
[25] S. Van Damme and J. Deconinck, *Journal of Physical Chemistry B* **2007**, *111*, 5308-5315.
[26] R. Hilfer, *Physica A* **1993**, *194*, 406-414.
[27] M. J. Danielson, *Journal of the Electrochemical Society* **1988**, *135*, 1326-1332.
[28] N. Epstein, *Chemical Engineering Science* **1989**, *44*, 777-779.
[29] P. Laevers, A. Hubin, H. Terryn and J. Vereecken, *Journal of Applied Electrochemistry* **1998**, *28*, 387-396.
[30] W. Bras, I. P. Dolbnya, D. Detollenaere, R. van Tol, M. Malfois, G. N. Greaves, A. J. Ryan and E. Heeley, *12th International Conference on Small-Angle Scattering* (Venice, Italy) **2002**, pp. 791-794.
[31] E. Homan, M. Konijnenburg, C. Ferrero, R. E. Ghosh, I. P. Dolbnya and W. Bras, *Journal of Applied Crystallography* **2001**, *34*, 519-522.
[32] J. Ilavsky, P. R. Jemian, A. J. Allen, F. Zhang, L. E. Levine and G. G. Long, *Journal of Applied Crystallography* **2009**, *42*, 469-479.

[33] J. A. Hammons, T. Rayment, I. Vandendael, O. Blajiev, A. Hubin, A. J. Davenport, M. Raes and H. Terryn, *Electrochemistry Communications* **2010**, *12*, 717-719.
[34] H. Terryn, J. Vereecken and G. E. Thompson, *Corrosion Science* **1991**, *32*, 1173-&.
[35] G. E. Thompson and G. C. Wood, *Corrosion Science* **1978**, *18*, 721-&.
[36] B. P. Wilson, A. Dotremont, M. Biesemans, R. Willem, P. Campestrini and H. Terryn, *Journal of the Electrochemical Society* **2008**, *155*, C22-C31.
[37] T. Dimogerontakis and H. Terryn, *Corrosion Science* **2007**, *49*, 3428-3441.
[38] T. Rayment, A. J. Davenport, A. J. Dent, J. P. Tinnes, R. J. K. Wiltshire, C. Martin, G. Clark, P. Quinn and J. F. W. Mosselmans, *Electrochemistry Communications* **2008**, *10*, 855-858.
[39] M. P. Amor and J. Ball, *Corrosion Science* **1998**, *40*, 2155-2172.
[40] P. Laevers, H. Terryn, J. Vereecken and G. E. Thompson, *International Conference to Mark the 20th Anniversary of the UMIST Corrosion-and-Protection-Centre: Advances in Corrosion and Protection* (Manchester, United Kingdom) **1992**, pp. 231-238.
[41] C. S. Lin and S. M. Fu, *Journal of the Electrochemical Society* **2001**, *148*, C240-C246.
[42] C. K. Dyer and R. S. Alwitt, *Journal of the Electrochemical Society* **1981**, *128*, 300-305.
[43] H. Terryn, J. Vereecken and G. E. Thompson, *Corrosion Science* **1991**, *32*, 1159-&.
[44] M. Pourbaix, *Atlas of electrochemical equilibria in aqueous solutions*, National Association of Corrosion Engineers, Houston, Tex., **1974**, p. 644 p.
[45] K. Ogle, M. Serdechnova, M. Mokaddem and P. Volovitch, *Electrochimica Acta 56*, 1711-1718.
[46] P. Laevers, H. Terryn, J. Vereecken, B. Kernig and B. Grzemba, *Corrosion Science* **1996**, *38*, 413-429.
[47] G. J. Marshall and J. A. Ward, *Materials Science and Technology* **1995**, *11*, 1015-1023.
[48] B. B. Rodriguez, J. M. C. Mol, B. Kernig, J. Hasenclever and H. Terryn, *Corrosion Science* **2011**, *53*, 930-938.
[49] A. J. Dowell, *Transactions of the Institute of Metal Finishing* **1986**, *64*, 85-90.
[50] Y. L. Lee, B. L. Ou and Y. H. Chiu, *Journal of Materials Science-Materials in Electronics* **2007**, *18*, 627-634.
[51] C. S. Lin, C. C. Chang and H. M. Fu, *Materials Chemistry and Physics* **2001**, *68*, 217-224.
[52] C. S. Lin, C. C. Chang and S. H. Hsieh, *Journal of the Electrochemical Society* **2000**, *147*, 3647-3653.
[53] J. W. Akitt, *Progress in Nuclear Magnetic Resonance Spectroscopy* **1989**, *21*, 1-149; S. P. Bi, C. Y. Wang, Q. Cao and C. H. Zhang, *Coordination Chemistry Reviews* **2004**, *248*, 441-455; D. W. Schaefer, R. A. Shelleman, K. D. Keefer and J. E. Martin, *Physica A* **1986**, *140*, 105-113.
[54] H. D. Bale and P. W. Schmidt, *Journal of Chemical Physics* **1959**, *31*, 1612-1618.
[55] J. Y. Bottero, J. M. Cases, F. Fiessinger and J. E. Poirier, *Journal of Physical Chemistry* **1980**, *84*, 2933-2939.
[56] W. H. Kuan, M. K. Wang, P. M. Huang, C. W. Wu, C. M. Chang and S. L. Wang, *Water Research* **2005**, *39*, 3457-3466; H. J. Liu, J. H. Qu, C. Z. Hu and S. J. Zhang, *Colloids and Surfaces a-Physicochemical and Engineering Aspects* **2003**, *216*, 139-147.
[57] S. S. Kumru and H. D. Bale, *Journal of Applied Crystallography* **1994**, *27*, 682-692.
[58] G. Johansson, *Acta Chemica Scandinavica* **1960**, *14*, 771-773.
[59] A. Singhal and K. D. Keefer, *Journal of Materials Research* **1994**, *9*, 1973-1983.
[60] S. M. Bradley, R. A. Kydd and R. F. Howe, *Journal of Colloid and Interface Science* **1993**, *159*, 405-412.
[61] A. N. Christensen, M. S. Lehmann and A. Wright, *Acta Chemica Scandinavica Series a-Physical and Inorganic Chemistry* **1982**, *36*, 779-781.
[62] K. Sinko, R. Mezei, J. Rohonczy and P. Fratzl, *Langmuir* **1999**, *15*, 6631-6636.
[63] C. S. Lin and C. C. Chiu, *Journal of the Electrochemical Society* **2005**, *152*, C482-C487.

[64] P. W. Schmidt, J. Kroughmoe and H. D. Bale, *Journal of Physical Chemistry* **1956**, *60*, 1580-1582; H. D. Bale and P. W. Schmidt, *Journal of Physical Chemistry* **1958**, *62*, 1179-1183.
[65] H. Terryn, B. Kernig, A. Hubin and P. Laevers, *Transactions of the Institute of Metal Finishing* **2000**, *78*, 29-34.
[66] H. Terryn, J. Vereecken and G. E. Thompson, *Transactions of the Institute of Metal Finishing* **1988**, *66*, 116-121.
[67] M. Dietzel and G. Bohme, *Geochimica et Cosmochimica Acta* **2005**, *69*, 1199-1211.
[68] F. Tomasoni, H. van Parys, H. Terryn, A. Hubin, J. Deconinck, J. M. Buchlin and J. van Beeck, *Electrochemistry Communications* **2010**, *12*, 156-159.
[69] G. Beaucage, *Physical Review E* **2004**, *70*.
[70] E. O. K. O. Glatter, Ed, *Small Angle X-Ray Scattering*, Academic Press, New York, New York, U.S.A, **1982**, p.
[71] H. Vogt, *Electrochimica Acta* **1980**, *25*, 527-531.
[72] S. W. Rutherford and D. D. Do, *Adsorption-Journal of the International Adsorption Society* **1997**, *3*, 283-312.
[73] A. K. Vijh, *Journal of Physical Chemistry* **1968**, *72*, 1148-&.
[74] D. Kashchiev and A. Firoozabadi, *Journal of Chemical Physics* **1993**, *98*, 4690-4699.
[75] L. Liu, A. Chakma and X. S. Feng, *Journal of Membrane Science* **2008**, *310*, 66-75.
[76] P. C. Pistorius and G. T. Burstein, *Philosophical Transactions of the Royal Society of London Series a-Mathematical Physical and Engineering Sciences* **1992**, *341*, 531-559.
[77] N. J. Laycock, M. H. Moayed and R. C. Newman, *Journal of the Electrochemical Society* **1998**, *145*, 2622-2628.
[78] N. J. Laycock and R. C. Newman, *Corrosion Science* **1997**, *39*, 1771-1790.
[79] N. J. Laycock, J. S. Noh, S. P. White and D. P. Krouse, *Corrosion Science* **2005**, *47*, 3140-3177.
[80] G. S. Frankel, *Journal of the Electrochemical Society* **1998**, *145*, 2970-2970.
[81] M. P. Ryan, D. E. Williams, R. J. Chater, B. M. Hutton and D. S. McPhail, *Nature* **2002**, *415*, 770-774.
[82] F. Hunkeler, A. Krolikowski and H. Bohni, *Electrochimica Acta* **1987**, *32*, 615-620.
[83] D. Landolt, P. F. Chauvy and O. Zinger, *Electrochimica Acta* **2003**, *48*, 3185-3201.
[84] G. T. Gaudet, W. T. Mo, T. A. Hatton, J. W. Tester, J. Tilly, H. S. Isaacs and R. C. Newman, *Aiche Journal* **1986**, *32*, 949-958.
[85] P. Russell and J. Newman, *Journal of the Electrochemical Society* **1986**, *133*, 59-69.
[86] T. R. Beck and R. C. Alkire, *Journal of the Electrochemical Society* **1979**, *126*, 1662-1666.
[87] E. Ruckenstein and Y. S. Djikaev, *Advances in Colloid and Interface Science* **2005**, *118*, 51-72.
[88] E. Ruckenstein and B. Nowakowski, *Journal of Colloid and Interface Science* **1990**, *137*, 583-592.
[89] G. Narsimhan and E. Ruckenstein, *Journal of Colloid and Interface Science* **1989**, *128*, 549-565.
[90] J. S. Newman and K. E. Thomas-Alyea, *Electrochemical Systems*, John Wiley & Sons, Inc., Hoboken, NJ, **2004**, p.
[91] T. R. Beck, *Journal of the Electrochemical Society* **1982**, *129*, 2412-2418.
[92] H. C. Kuo and D. Landolt, *Electrochimica Acta* **1975**, *20*, 393-399.
[93] R. D. Grimm, A. C. West and D. Landolt, *Journal of the Electrochemical Society* **1992**, *139*, 1622-1629.
[94] N. Sridhar and D. S. Dunn, *Journal of the Electrochemical Society* **1997**, *144*, 4243-4253.
[95] R. D. Grimm and D. Landolt, *Corrosion Science* **1994**, *36*, 1847-1868.
[96] A. C. West, R. D. Grimm, D. Landolt, C. Deslouis and B. Tribollet, *Journal of Electroanalytical Chemistry* **1992**, *330*, 693-706.
[97] A. C. West, *Journal of the Electrochemical Society* **1993**, *140*, 403-408.
[98] J. L. Luo, O. E. Hileman and M. B. Ives, *Corrosion Science* **1993**, *35*, 73-81.
[99] Y. H. Li, R. Gemmen and X. B. Liu, *Journal of Power Sources* **2010**, *195*, 3345-3358.

[100] W. W. Crook and J. L. Jambor, *Canadian Mineralogist* **1979**, *17*, 107-109.
[101] R. Kleinberg, *The Journal of Chemical Physics* **1969**, *50*, 4690-4696; J. Mizuno, *Journal of the Physical Society of Japan* **1961**, *16*, 1574-&.
[102] D. C. Silverman, *Corrosion* **1981**, *37*, 546-548.
[103] L. M. Varela, M. Garcia, F. Sarmiento, D. Attwood and V. Mosquera, *Journal of Chemical Physics* **1997**, *107*, 6415-6419.
[104] L. F. Shampine, M. W. Reichelt and J. A. Kierzenka, *Siam Review* **1999**, *41*, 538-552.
[105] H. X. Liu and V. G. Papangelakis, *Industrial & Engineering Chemistry Research* **2006**, *45*, 39-47.
[106] M. Laliberte and W. E. Cooper, *Journal of Chemical and Engineering Data* **2004**, *49*, 1141-1151.
[107] P. Cheng, R. H. Chen, J. F. Wang, J. N. Yu, T. A. Lan, W. J. Wang, H. J. Yang, H. X. Wu and C. S. Deng, *Nanoscale Research Letters 5*, 1313-1319.